INNOVATIVE DESIGNS OF RF TRANSMIT ARRAY COILS AND RF HEATING ANALYSIS OF PATIENTS WITH IMPLANTED DBS

A DISSERTATION SUBMITTED TO

THE GRADUATE SCHOOL OF ENGINEERING AND SCIENCE

OF BILKENT UNIVERSITY

IN PARTIAL FULFILLMENT OF THE REQUIREMENTS FOR

THE DEGREE OF

DOCTOR OF PHILOSOPHY

IN

ELECTRICAL AND ELECTRONICS ENGINEERING

By

Ehsan Kazemivalipour

September 2020

INNOVATIVE DESIGNS OF RF TRANSMIT ARRAY COILS AND RF HEATING ANALYSIS OF PATIENTS WITH IMPLANTED DBS

By Ehsan Kazemivalipour

September 2020

We certify that we have read this dissertation and that in our opinion it is fully adequate, in scope and in quality, as a dissertation for the degree of Doctor of Philosophy.

Ergin Atalar (Advisor)

Emine Ülkü Sarıtaş Çukur

Özgür Salih Ergül

Laleh Golestani Rad

Yiğitcan Eryaman

Approved for the Graduate School of Engineering and Science:

Ezhan Karaşan

Director of the Graduate School

ABSTRACT

INNOVATIVE DESIGNS OF RF TRANSMIT ARRAY COILS AND RF HEATING ANALYSIS OF PATIENTS WITH IMPLANTED DBS

Ehsan Kazemivalipour
Ph.D. in Electrical and Electronics Engineering
Advisor: Ergin Atalar
September 2020

A safe and efficient magnetic resonance imaging (MRI) test would rely on informed specification, design, implementation, assessment, and application of appropriately selected radiofrequency (RF) coils. Towards these goals, this dissertation comprises three contributions to novel RF transmit array (TxArray) coil design techniques and two contributions to RF heating reduction of deep brain stimulation (DBS) implants in RF transmit coils.

TxArray coils with multiple transmit elements provide the additional degrees of freedom that can be used to enhance field uniformity, accelerate acquisition time, enable RF shimming while intending to mitigate specific absorption rate (SAR) hotspots, and increase power efficiency. How a TxArray coil is designed can have a significant impact on its gain from parallel transmission technology. Thus, the first contribution of this dissertation is on the eigenmode analysis of the scattering matrix for the design of TxArray coils to obtain their efficient operation modes and achieve an efficient RF shimming in terms of power consumption. The algorithm is tested for the design of four 3T TxArray coils with 8 to 32 channels, and it is shown that it can enlarge the dimension of the excitation space by up to 50% compared with the commonly used design techniques. The next contribution is to establish a fast fine-tuning procedure to precisely design an imperfectly manufactured TxArray coil using its corresponding equivalent circuit model. By fitting the measured scattering parameters to a lumped circuit model, all inductances/resistances of an 8-channel 3T TxArray coil are estimated. The manufactured coil is then appropriately tuned only in a single iteration. As another contribution, a theoretical coil size optimization is

introduced to minimize the magnetic coupling between non-adjacent transmit channels of a TxArray coil. By calculating all self/mutual-inductances of a 12-channel 3T TxArray coil and minimizing mutual-inductances, its sizes are determined. The finite element simulations are performed to demonstrate the feasibility of this approach.

One of the safety considerations of RF transmit coils is the localized SAR amplification due to the interaction of metallic implants with the coil's electric fields. Therefore, the fourth contribution is on evaluating SAR mitigation performance at tips of patient-derived realistic DBS implants using a 3T patient-adjustable transmit coil, which uses a mechanically rotating linearly polarized birdcage resonator. The reconfigurable coil system decreases the SAR on average by 83% for unilateral leads and by 59% for bilateral leads in comparison to a conventional quadrature birdcage coil. In the final study, the local SAR amplification surrounding the tips of a large cohort of DBS implants with realistic lead trajectories in a commercially available vertical open-bore 1.2T coil and a standard horizontal closed-bore 1.5T birdcage coil is presented. On average, SAR is decreased by 31-fold in the 1.2T vertical coil compared to the 1.5T horizontal coil.

Overall, this dissertation proposes innovative approaches for designing TxArray coils and heating assessment and SAR reduction of DBS patients, which mainly contribute to improving the performance of RF transmit coils in terms of power efficiency and patient safety.

Keywords: Magnetic resonance imaging (MRI), Radiofrequency (RF) coil, Transmit array coil, Eigenmode analysis, Equivalent circuit model, Coupling, MRI safety, Deep brain stimulation (DBS), Specific absorption rate (SAR)

ÖZET

RF VERİCİ DİZİSİ SARGILARININ YENİLİKÇİ TASARIMLARI VE İMPLANTE EDİLMİŞ DBS'Lİ HASTALARIN RF ISINMA ANALİZİ

Ehsan Kazemivalipour
Elektrik ve Elektronik Mühendisliği, Doktora
Tez Danışmanı: Ergin Atalar
Eylül 2020

Güvenilir ve verimli bir manyetik rezonans görüntüleme (MRG) testi, uygun şekilde seçilmiş RF sargıların tanımlama, tasarım, değerlendirme ve uygulanmasına dayanmaktadır. Bu amaçlar doğrultusunda, bu tez savunması özgün RF verici dizisi (TxArray) sargı tasarım tekniklerine üç katkıdan ve RF verici sargılarındaki derin beyin stimülasyonu (DBS) implantlarının RF ısınma azaltımına iki katkıdan oluşmaktadır.

Çoklu verici elementlerinden oluşan TxArray sargıları, alan tekdüzeliğini arttırabilmek, toplama süresini hızlandırabilmek, özgül soğurma oranı (ÖSO) noktalarını azaltmak amacıyla RF şim ayarlamasını mümkün kılabilmek ve güç verimliliğini arttırabilmek için ek serbestlik dereceleri sağlar. Bir TxArray sargısının nasıl tasarlandığı, paralel iletim teknolojisinden edinilen kazanç üzerinde önemli bir etkiye sahiptir. Böylece, bu tezin ilk katkısı, TxArray sargılarının tasarımı için verimli çalışma modlarını elde etmek ve güç tüketimi açısından verimli bir RF şimlemesi elde etmek amacıyla saçılma matrisinin özmod analizi üzerinedir. Algoritma, 8-32 kanallı dört 3T TxArray sargılarının tasarımı için test edilmiş ve yaygın olarak kullanılan tasarım tekniklerine kıyasla yayılma alanının boyutunu %50'ye kadar genişletebildiği gösterilmektedir. Bir sonraki katkı, karşılık gelen eşdeğer devre modelini kullanarak kusurlu bir şekilde üretilmiş bir TxArray sargısını tam olarak tasarlamak için hızlı bir ince ayar prosedürü oluşturmaktır. Ölçülen saçılma parametreleri bir toplu devre modeline uydurularak, 8 kanallı bir 3T TxArray sargısının tüm endüktans/dirençleri tahmin edilir. Üretilen sargı daha sonra yalnız tek bir iterasyonda uygun bir şekilde ayarlanır. Diğer bir katkı olarak, bir TxArray sargısının bitişik olmayan verici kanalları

arasındaki manyetik kuplajı en aza indirmek için teorik bir sargı boyutu optimizasyonu öne sürülmüştür. 12 kanallı bir 3T TxArray sargısının tüm öz/karşılıklı endüktansları hesaplanarak ve karşılıklı endüktansları en aza indirgenerek boyutları belirlenir. Bu yaklaşımın uygulanabilirliğini göstermek amacıyla sonlu eleman simülasyonları gerçekleştirilir.

RF verici sargılarının güvenlik hususlarından biri, metalik implantların sargının elektrik alanları ile etkileşimi nedeniyle lokalize ÖSO amplifikasyonudur. Bu nedenle dördüncü katkı, mekanik olarak dönen doğrusal polarize bir kuş kafesi rezonatörü kullanan 3T ayarlanabilir verici bobini kullanılarak hastadan türetilen gerçekçi DBS implantlarının uçlarındaki ÖSO azaltma performansının değerlendirilmesi üzerinedir. Yeniden yapılandırılabilir sargı sistemi, ÖSO'ı geleneksel kuadratür kuş kafesi sargısına kıyasla, tek taraflı uçlar için ortalama %83 ve iki taraflı uçlar için %59 azaltmıştır. Son çalışmada, ticari olarak temin edilebilen dikey açık 1.2T sargısındaki ve standart yatay kapalı 1.5T kuş kafesi sargısındaki gerçekçi uç yörüngelerine sahip büyük bir DBS implant kohortunun uçları çevresindeki yerel ÖSO amplifikasyonu sunulur. Ortalama olarak ÖSO, 1.5T yatay sargıya kıyasla 1.2T dikey sargıda 31 kat azalmıştır.

Genel olarak, bu tez, esasen RF verici sargılarının güç verimliliği ve hasta güvenliği açısından performansını iyileştiren, TxArray sargılarının tasarımı, ısınma değerlendirmesi ve DBS hastalarının ÖSO azaltımı için yenilikçi yaklaşımlar öne sürmektedir.

Anahtar sözcükler: Manyetik rezonans görüntüleme (MRG), Radyo-frekansı (RF) sargı, Verici dizisi sargısı, Özmod analiz, Eşdeğer devre modeli, Kuplaj, MRG güvenliği, Derin beyin stimülasyonu (DBS), Özgül soğurma oranı (ÖSO)

Acknowledgment

Doing the Ph.D. is like going through a challenging journey, which without many people's support and contribution it was not possible to come to the endpoint of this journey. I would express my deep gratitude to all the people who helped and supported me during this journey to make this experience unforgettable and this dissertation possible.

First and foremost, I would like to extend my sincere gratefulness to Prof. Ergin Atalar for his continued guidance, infinite support, encouragement, and patience throughout my Ph.D. studies. His immense knowledge and unwavering enthusiasm for research kept me engaged with my studies and research. His generous support and help let me pursue my research freely and taught me how to be a researcher, not just a student. I would like to thank him for providing such a great, professional, and friendly research environment at UMRAM.

My appreciation also extends to Prof. Laleh Golestani Rad for her incredible contribution, support, help, and advice whenever I need. Her support and guidance resulted in shaping two chapters of my dissertation. She generously shared their collected data and some tools at Northwestern University with me, which they played an essential role in my research.

I also convey my grateful thanks to my thesis committee members, Prof. Emine Ülkü Sarıtaş, Prof. Özgür Salih Ergül, Prof. Laleh Golestani Rad, and Prof. Yiğitcan Eryaman for their insightful comments, valuable suggestions, and inquiries and their precious time and effort assessing this dissertation.

I would state my special thanks to my colleagues at UMRAM and Northwestern University, which without their contribution and help on this research it would be hard to be at this point: Dr. Alireza Sadeghi-Tarakameh, Uğur Yılmaz, Umut Gundogdu, Dr. Bhumi Bhusal, Jasmine Vu, and Dr. Bach Thanh Nguyen.

I would express my thanks to all the UMRAM family and my lab mates for providing such a friendly and professional environment. My special thanks go to Prof. Kader Karlı Oğuz, Dr. Erkan Dorken, Aydan Ercingoz, Elif Ünal, Dr. Volkan Acıkel,

Dr. Cemre Arıyurek, Maryam Salim, Reza Babaloo, Suheyl Taraghinia, Mina Elhami, Dr. Manouchehr Takrimi, Taner Demir, Berk Silemek, Dr. Koray Ertan, Reyhan Ergün, Bilal Tasdelen, Said Aldemir, Mustafa Can Delikanlı, Ahmet Fatih Yaprak, Ziba Arghiani, Mert Bozkurt and my dear friends, Bahram, Mehdi, Elnaz, Sina, Maryam, Mohammadali, Gamze, Amir, Zeynab, Wiria, Fatemeh, Parviz, Aysan, Yashar, Leila, Khalil, Dariush, Meysam, and many others I did not write here, but they all touched my heart.

My deepest gratitude, love, and appreciation goes to my dear parents, grandmothers, mother and father in law, my sisters Zahra and Rezvan, and my old dear friend and sister in law, Ladan, for their everlasting support, continuous encouragement, and love. Without their blessings, I would not have this accomplishment.

Finally and above all, I wish to acknowledge the support and great love of my dear wife and my best friend, Laleh, who always support me, uplift me, comfort me, and bring joy to my soul as she shares a piece of her own in the precise magical moment it needed to happen. I feel very lucky to be able to experience life alongside her.

Content

List of Figures

List of Tables

Chapter 1

Introduction

Magnetic resonance imaging (MRI) is a non-invasive and powerful medical imaging tool. MRI is one of the most popular imaging modalities for diagnosis purposes. Indeed, MRI could penetrate deep into tissue with minimal risk for the patient and provide an outstanding soft-tissue contrast. MRI has been at the forefront of many researchers' interest throughout its existence, owing to its significance in clinical applications. Technological advancements developed and tested in the world's research laboratories continue to improve the flexibility and efficiency of MRI scanners. However, the evidently untapped capacities which remain could be the most interesting relative to the development of MRI.

The MRI principality is constructed from the main magnet with an intense static field (~ T), radiofrequency (RF) coil (~ μT), and three gradient coils with orthogonal fields (~ mT/m). RF coils serve to both stimulate and receive the MRI signal and can be categorized as transmit only, receive only, and transmit/receive (transceiver) coils. An informed specification, design, implementation, assessment, and application of appropriately selected RF coils will provide a safe and efficient MRI test. Since the earliest days of the MRI scanners, researchers have been finding ways to develop RF coils. In fact, RF coils have developed from the simplistic single-channel coils to the complicated multi-channel coils designed for modern applications. Developed multi-channel technology for RF coils with array elements have found new and more essential applications in parallel transmit schemes and parallel imaging to further enhance imaging quality, speed, and safety.

The RF frequency for proton MRI has also risen as MRI has shifted to greater field strengths. Partly because of the human body's electrical characteristics and partially because of the physical scale, the RF excitation homogeneity reachable with one channel transmit coil sometimes is not sufficient for reliable clinical diagnosis in some applications and with some patients [1, 2]. Full-body electromagnetic (EM) field simulations demonstrate considerable RF inhomogeneity (dielectric shading) and local SAR variations for the typical clinical RF coils used today, which eventually restrict scan speed [3, 4].

Radiofrequency (RF) transmit array (TxArray) coils, using multiple RF transmit coil elements in parallel, are being extensively utilized in ultra-high field MRI to overcome different issues, such as RF excitation inhomogeneities [5-15]. TxArray coils can be very useful for conventional high-field scanners since they provide additional degrees of freedom to the designers of pulse sequences and enable RF shimming while attempting to suppress SAR [16-18] hotspots. Besides, these degrees of freedom are useful for increasing power efficiency [19-21] and accelerating RF-intense applications [15]. TxArray coils can also be beneficial for the implementation of the implant-friendly mode [22-25]. It follows that TxArray coils are critical for obtaining the maximum benefit from high-field MRI.

TxArray coil's performance can gain considerably from the parallel transmission technology when the coil designs meet particular specifications, such as low coupling among individual array elements and appropriate interaction with subjects under test to provide a sufficient $\mathbf{B}_1^+$ field [26] efficiency. The high coupling level causes extra reflected power from the TxArray coil and decreases the power delivered to the subject, which is consequently considered a significant design challenge [21]. Numerous approaches are employed to reduce the effective coil coupling, including the use of L/C decoupling networks [27-30], overlapping of neighboring array elements [31, 32], transformer decoupling [33], inserting the induced current elimination (ICE) decoupling elements [34, 35], and adding reactive decoupling circuits among adjacent array elements [36]. Increasing the number of array elements will increase degrees of freedom for shimming and enhance excitation encoding capabilities of TxArray coils. The high coupling among individual array elements conversely decreases these degrees of freedom as $\mathbf{B}_1^+$ patterns of the array elements become more similar. However, as the number of array elements increases, the

coupling issue becomes more challenging because it requires further decoupling components and longer RF cables to decouple non-neighboring array elements [21, 37, 38]. Owing to the factors mentioned above, it is far more challenging to design TxArray coils than conventional coils. Therefore, part of this dissertation introduces novel design techniques for TxArray coils.

Correspondingly, chapter 2 introduces the concept of the scattering (**S**) matrix eigenmode analysis. Using this concept, a general design technique for obtaining efficient operation modes of TxArray coils is developed. It is demonstrated that eigenmode analysis of the **S**-matrix is an efficient method that provides a quantitative and compact representation of the TxArray coil's power transmission capabilities. This method offers a simple tool for quantifying, comparing, and optimizing the performance of the TxArray coils. It is shown that the ratio of the total reflected power to the total incident power of TxArray coils for a given excitation signal is the weighted sum of the eigenvalues $\mathbf{S}^{\mathbf{H}}\mathbf{S}$-matrix where the superscript **H** denotes the Hermitian transpose. Minimizing the eigenvalues of $\mathbf{S}^{\mathbf{H}}\mathbf{S}$-matrix can increase the excitation space of TxArray coils with a low total reflection. This chapter also presents a new and efficient methodology for designing TxArray coils based on minimizing the total reflected power for certain operating modes. It shows that the low total reflected power for some critical excitation modes can be achieved for all TxArray coils, even with a high coupling level. The method can enable the coil designers to find the maximum possible number of efficient modes for a TxArray coil with an arbitrary number of channels by optimizing the free design parameters. The performance of various 3T TxArray coils is investigated using the proposed method together with simulations and experiments.

Chapter 3 presents a fast fine-tuning method for designing an imperfectly manufactured TxArray coil using its equivalent circuit model. In a typical transmit coil building process, the general structure of the coil is designed, and its capacitor values are found using various optimization processes [39, 40], which may include an electromagnetic field simulation. The imperfections in the manufacturing process result in poor performance. The coil has to be fine-tuned to improve its performance. Although the fine-tuning process is rather straightforward when the number of coil elements is low, it becomes challenging for a coil with a high number of channels. This chapter proposes to fit the measured **S** parameters to an equivalent circuit model

to estimate all self/mutual-inductances and self/mutual-resistances of the manufactured coil, and then to find the capacitors that fine-tune the coil. The fine-tuning process of a 3T TxArray coil is accelerated using the proposed method, and it is demonstrated that the fabrication could be done only in a single iteration.

Chapter 4 lays out a TxArray coil design strategy based on minimizing the magnetic coupling between non-adjacent transmit array elements. According to the proposed method, the TxArray coil's design has changed from a traditional single-stage procedure to a two-stage procedure. A vast majority of design strategies are based on optimizing the capacitor values for a TxArray coil with predefined geometry. The method presented in this chapter focuses on optimizing the coil's sizes, before optimizing capacitors, to decrease the mutual-inductances between non-adjacent array elements. As a sample design, a 3T TxArray coil's optimum dimensions, such as coil radius, coil length, copper widths, are determined. Finite element based simulations are performed to confirm the validity of the method.

Although the magnetic component of the RF field stimulates the MRI signals, the corresponding electric field is the cause of bioeffects. Nerve stimulation and tissue heating, principally, are the instant bioeffects of RF fields [41]. Thus, safety consideration has been one of the most critical research topics in MRI. The localized specific absorption rate (SAR) concentration due to the interaction of metallic medical implants with electric fields is one of the essential safety considerations of RF coils. There has recently been considerable attention paid to the measurement of implant heating and the development of computational methods for implant safety assessments. Therefore, part of this dissertation is dedicated to RF safety assessment of patients with metallic implants.

MRI of patients with deep brain stimulation (DBS) implants is highly beneficial, both for target verification and to assess the "connectomics" functional effects of the neuromodulation [42]. Unfortunately, the interaction of RF fields with elongated DBS leads causes safety concerns that restrict MRI accessibility to these patients. Recent studies are mostly based on steering electric-field free regions in RF transmit coils through the design of implant-friendly modes using parallel transmit technology [22, 43-45]. Rendering the parallel transmit strategy is, however, complicated for ordinary applications in the clinic. Recently, a reconfigurable MRI technology with a rotating transmit coil was introduced, which offers an easy operational setup yet significant

reduction in SAR near tips of unilateral DBS leads during MRI at 1.5T [46, 47]. Chapter 5 presents the feasibility of using such reconfigurable coil technology for DBS imaging at 3T. This is the first study to assess the performance of field-steering based methods to simultaneously reduce the SAR at tips of bilateral DBS leads, use patient-derived realistic models, and consider both isolated leads and fully-implanted DBS systems with different configurations.

The majority of studies on RF heating of conductive implants, as well as the MR-labeling of DBS devices, have been limited to horizontal close-bore MRI scanners. Vertical MRI scanners introduced initially as open low-field MRI systems, are now available at 1.2T field strength, capable of high-resolution structural and functional imaging. No literature exists on DBS SAR in this class of scanners, which have a 90° rotated transmit coil and thus, generate fundamentally different electric and magnetic field distributions. Chapter 6 presents a simulation study of RF heating in a cohort of 90 patient-derived DBS lead models during MRI in a commercially available vertical open-bore MRI system (1.2T OASIS, Hitachi) and a standard horizontal 1.5T birdcage coil. It is shown that the open-bore vertical MRI system generates a significantly less SAR around implanted DBS leads. This SAR reduction is consistent over a large and diverse patient population with both types of isolated and fully implanted systems operated at two DBS centers.

Overall, this dissertation introduces innovative TxArray coil design techniques and evaluates RF heating in patients with implanted DBS leads to mitigate SAR during MRI scan, which primarily translates to improving the performance of RF transmit coils in terms of power efficiency and patient safety.

Chapter 2

Eigenmode Analysis of the Scattering Matrix for the Design of MRI Transmit Array Coils

2.1 Preface

The content of this chapter was partially presented at the International Society of Magnetic Resonance in Medicine (ISMRM)'s 27th and 28th Annual Scientific Meetings [48, 49], and published in Magnetic Resonance in Medicine [50]. The text, figures, and tables presented in this chapter are all based upon the journal publication [50]. Ergin Atalar has been involved in the conceptualization and methodology of the content of this chapter. The phantom experiments were conducted by the help of Alireza Sadeghi-Tarakameh.

2.2 Introduction

The performance of Radiofrequency (RF) transmit array (TxArray) coils significantly profits from parallel transmit technology if the coil designs satisfy particular requirements, such as low mutual coupling between individual array elements and sufficient interaction with samples to ensure sufficiently high power efficiency. High coupling among array elements makes power delivery to the subject challenging and, therefore, is considered a major design issue [21]. Increasing the number of transmit

elements can enhance the capability of TxArray coils in terms of RF shimming and homogeneity. The problem of mutual coupling reduction becomes more complex as the number of array elements increases due to the need for more decoupling components and longer cables to decouple non-adjacent elements, which are distantly located [21, 37, 38]. Considering the cost of high-power RF amplifiers, improvements in the incremental performance by further transmit elements with realistic assumptions of power budget for particular TxArray coil geometries and configurations should be determined. Theoretically, the power efficiency of a TxArray coil under single-channel excitation depends on the amount of power coupled to other transmit elements and is reflected back to the amplifier. The reflected power does not produce the $\mathbf{B}_1^+$ field [26] within the sample and may cause damage to the amplifiers [21, 51]. In this situation, proper matching, tuning, and decoupling of a TxArray coil produce higher transmitted power from the amplifier to the transmit elements and lower reflected power from all transmit elements [21, 52]. For a TxArray coil with coupled transmit elements under multichannel excitation, the total reflected power depends on the phases and amplitudes of the RF excitation signals, as well as the levels of matching, tuning, and decoupling. Although multiple studies focused on optimizing the excitation signals with various strict constraints, including the power consumption of TxArray coils [21, 53-57], categorization of the inputs based on the transmitted and reflected power in TxArray coils warrants attention.

Here, the concept of excitation eigenmodes is presented to achieve a quantitative and compact representation of the TxArray coil's transmission capabilities. For a given set of excitation signals, the total power transmitted to a TxArray coil can be analyzed using its scattering matrix (**S**-matrix), which can be determined as a relationship between the incident waves and reflected waves. The eigenmode analysis of **S**-matrix provides insight into the excitation signals with a low level of reflected power. It offers a simple tool for quantifying, comparing, and optimizing the performance of the TxArray coils.

An ideal TxArray coil in terms of the power efficiency will have a zero total reflected power for all incident waves, which requires a zero **S**-matrix. Due to the practical limitations and imperfections in matching and decoupling, **S**-matrix cannot be zero. However, the **S**-matrix elements can be minimized by adjusting the geometrical parameters or capacitor values of the coil using an optimization process.

In this process, the optimization criterion is fundamental and affects the performance of the coil [58]. The vast majority of studies concentrated on minimizing the magnitude of **S**-matrix elements without considering the excitation signals [38, 59-61]. However, the excitation signals have a significant role in determining the total transmitted and reflected power levels [58]. For a given TxArray coil, the reflection can be high for some excitation signals but low for some others. Here, it is proposed that the eigenmode analysis, looking at the **S**-matrix as a whole, captures more than just looking at the **S**-matrix elements individually. In this new matrix analysis, in addition to the magnitude of the **S**-matrix elements, their phases are also included, which was previously ignored. The insight provided by this approach can be used to minimize the total reflected power for larger sets of excitation signals by adjusting the TxArray coil design parameters. The novel design strategy utilized in this chapter demonstrates the possibility of obtaining very low total reflected power for specific sets of excitations, even for TxArray coils with a nonzero **S**-matrix.

In this chapter, the theory and concept of the **S**-matrix eigenmode analysis are provided, the details of the TxArray coil design are discussed, and the optimization strategy used to adjust the capacitor values to minimize the total reflected power is explained. A variety of simulation and experiment results on four dual-row TxArray coils with a different number of channels for imaging at 3T scanners are also provided. These coils [62, 63] have a significant potential to replace the conventional body coils since they can perform similar to the traditional birdcage coils if they are driven in the circularly polarized (CP) form but also provide additional degrees of freedom for many valuable applications of the TxArray coils.

2.3 Theory

The **S**-matrix describing a TxArray coil characterizes all the power interactions between its input ports. For a generic TxArray coil consisting of *N* transmit elements, the **S**-matrix is represented as **b** = **Sa**, where **a** and **b** are the vectors of the incident and reflected waves, respectively, defined as

$$\mathbf{a} = \frac{1}{2\sqrt{|\Re\{Z_0\}|}}(\mathbf{V} + Z_0\mathbf{I}) \quad \text{and} \quad \mathbf{b} = \frac{1}{2\sqrt{|\Re\{Z_0\}|}}(\mathbf{V} - Z_0^{*}\mathbf{I}) \tag{2.1}$$

where **V** and **I** are the vectors of root-mean-square port voltages and currents. Z_0 is the reference impedance and is chosen as 50 ohms in this chapter. With this formulation, the total average power transmitted to a TxArray coil with lossless transmission lines can be written as [64]

$$P_t^T = \mathbf{a^H a} - \mathbf{b^H b} = \mathbf{a^H}(\mathbf{U} - \mathbf{S^H S})\mathbf{a} \tag{2.2}$$

where the superscript **H** denotes the Hermitian (conjugate) transpose, and **U** denotes the identity matrix. Equation (2.2) expresses the net transmitted power as the difference between the incident power and the reflected power, which can be quantified as $P_i^T = \mathbf{a^H a}$ and $P_r^T = \mathbf{b^H b}$, respectively. A perfect design has 100% transmitted power and no reflected power, which does not occur when the transmit coil elements are coupled. The ratio of the total reflected power to the total incident power can be defined as the *normalized reflected power*. The normalized reflected power can be characterized as a function of the excitations and **S**-matrix

$$\lambda(\mathbf{a}) = \frac{P_r^T}{P_i^T} = \frac{\mathbf{b^H b}}{\mathbf{a^H a}} = \frac{\mathbf{a^H S^H S a}}{\mathbf{a^H a}} \tag{2.3}$$

$\lambda(\mathbf{a})$ can be minimized to ensure high transmit efficiency.

Examining $\mathbf{S^H S}$ can provide information on the total incident and reflected power of a TxArray coil [65, 66]. $\mathbf{S^H S}$ is a Hermitian matrix, which is therefore diagonalizable by a unitary similarity transformation [67]. Hence

$$\mathbf{S^H S} = \mathbf{Q}\Lambda\mathbf{Q^H} \tag{2.4}$$

where **Q** is a unitary matrix (i.e., $\mathbf{QQ^H = Q^HQ = U}$) formed by the eigenvectors ($\mathbf{q}_n$) of $\mathbf{S^H S}$. $\mathbf{\Lambda}$ is a diagonal matrix formed by the eigenvalues (λ_n) of $\mathbf{S^H S}$.

If the TxArray coil is excited in such a way that the vector of the incident waves is equal to the *n*th eigenvector of $\mathbf{S^H S}$, i.e., $\mathbf{a} = \mathbf{q}_n$, then the normalized reflected power yields

$$\lambda(\mathbf{a} = \mathbf{q}_n) = \frac{\mathbf{b^H b}}{\mathbf{a^H a}} = \frac{\mathbf{q}_n^\mathbf{H}\mathbf{S^H S}\mathbf{q}_n}{\mathbf{q}_n^\mathbf{H}\mathbf{q}_n} = \frac{\mathbf{q}_n^\mathbf{H}\lambda_n\mathbf{q}_n}{\mathbf{q}_n^\mathbf{H}\mathbf{q}_n} = \lambda_n \tag{2.5}$$

because $[\mathbf{S^H S}]\mathbf{q}_n = \lambda_n \mathbf{q}_n$. It should be noted that all eigenvalues are positive real with values less than or equal to one [68]. The eigenvectors of $\mathbf{S^H S}$ are orthogonal [68] and represent the excitation vectors of the TxArray coil. Therefore, they shall be called the *excitation eigenmodes* of the TxArray coil, and the eigenvalues of $\mathbf{S^H S}$ shall be called the *modal reflected power* values of the TxArray coil. The normalized reflected power in the case of an arbitrary vector of incident waves, which can be uniquely expanded as a sum of the distinct eigenmodes, that is, $\mathbf{a} = \sum_{n=1}^{N} w_n \mathbf{q}_n = \mathbf{Q}\mathbf{w}$, where $\mathbf{w} = \begin{bmatrix} w_1 & w_2 & \dots & w_N \end{bmatrix}^{\mathbf{T}}$ is the vector of the expansion coefficients, can be expressed as follows

$$\begin{aligned} \lambda(\mathbf{a}) &= \frac{\mathbf{a^H S^H S a}}{\mathbf{a^H a}} = \frac{\mathbf{w^H Q^H S^H S Q w}}{\mathbf{w^H Q^H Q w}} \\ &= \frac{\mathbf{w^H Q^H Q \Lambda Q^H Q w}}{\mathbf{w^H Q^H Q w}} = \frac{\mathbf{w^H \Lambda w}}{\mathbf{w^H w}} = \sum_{n=1}^{N} \left(\lambda_n \left(\frac{w_n}{\|\mathbf{w}\|} \right)^2 \right) \end{aligned} \tag{2.6}$$

Equation (2.6) shows that the normalized reflected power can be represented as the normalized weighted sum of the modal reflected power values. Because the form of $\lambda(\mathbf{a})$ is a Rayleigh quotient [69], its values are always between the smallest and largest λ_n values [65]. To obtain an ideal TxArray coil with zero total reflected power for any arbitrary inputs, all eigenvalues of $\mathbf{S^H S}$ must be zero, which does not appear to be feasible. However, the parameters in determining $\mathbf{S^H S}$ can be adjusted to minimize all eigenvalues and achieve a low total reflected power for a broader set of incident waves.

2.4 Methods

2.4.1 λ-opt design strategy

In this chapter, a design strategy based on the minimization of the normalized reflected power was employed to obtain the capacitor values of TxArray coils, known as λ-optimization (λ-opt). This strategy minimizes the normalized reflected power for excitation eigenmodes as well as for the CP excitation vector, that is, λ_{CP}. Minimizing λ_{CP} provides the opportunity to compose the CP excitation mode from the most

efficient excitation eigenmodes. However, the optimization problem was formulated as

$$\lambda\text{-opt:} \quad \min_{\bar{\mathbf{c}}} \quad \sum_{n=1}^{N}\left(\alpha_n \lambda_n{}^2\right) + \alpha_{CP}\lambda_{CP}^2 \tag{2.7}$$

where $\bar{\mathbf{c}}$ is the vector of the capacitor values and N is the total number of channels. α_n and α_{CP} represent the weights for each term. A constraint can be added to Equation (2.7) to obtain desired modes of operations. This general formulation was used under three specific cases:

$$\begin{aligned} &\text{case\#1} \quad \min_{\bar{\mathbf{c}}} \quad \frac{1}{N}\sum_{n=1}^{N}\lambda_n{}^2 + \lambda_{CP}^2 \\ \lambda\text{-opt:} \quad &\text{case\#2} \quad \min_{\bar{\mathbf{c}}} \quad \frac{1}{N}\sum_{n=1}^{N}\lambda_n{}^2 + \lambda_{CP}^2 \\ &\qquad\qquad \text{s.t.} \quad \lambda_{CP} \le 0.01 \\ &\text{case\#3} \qquad \min_{\bar{\mathbf{c}}} \quad \frac{1}{N}\sum_{n=1}^{N}\lambda_n{}^2 \end{aligned} \tag{2.8}$$

These three different minimization cases were employed to investigate the impact of the added constraint and weighting coefficients on the optimization results. To compare the performance of the λ-opt strategy, the conventional minimization strategy [20, 39, 52, 70], which is based on minimizing the magnitude of the **S**-matrix elements individually (**S**-opt), was also implemented. For this, the difference between the actual and desired **S**-matrices was minimized, as described in Ref. [39]. Therefore, this optimization criterion was formulated as

$$\begin{aligned} \mathbf{S}\text{-opt:} \quad &\min_{\bar{\mathbf{c}}} \quad \frac{1}{N}\sum_{n=1}^{N}\sum_{m=1}^{N}|s_{mn}|^2 \\ &\text{s.t.} \quad |s_{nn}| \le -15\,\text{dB} \end{aligned} \tag{2.9}$$

The added constraint puts an upper limit on the reflection coefficients. Note that $\sum_{n=1}^{N}\sum_{m=1}^{N}|s_{mn}|^2$, which is equal to the trace of $\mathbf{S^H S}$, can also be calculated as the summation of the λ_n values [67]; therefore, the **S**-opt approach minimizes the average of the λ_n values denoted as λ_{av}, while limiting the reflection coefficients to be equal to or less than -15 dB.

2.4.2 Proposed model for RF TxArray coil

The proposed model and schematic of dual-row ($2\times\frac{N}{2}$-channel) head TxArray coils are shown in Figure 2.1. These coils have a cylindrical geometry, is composed of N transmit loops with the same dimensional sizes distributed in both the circumferential direction and the z-direction, and can be decoupled (approximately) by adjusting the decoupling capacitors placed between the nearest neighbors. In each loop, five distinct capacitor values, that is, $\overline{\mathbf{c}} = [c_{dr} \quad c_{dc} \quad c_t \quad c_m \quad c_s]$, mainly control the performance of the TxArray coils as free design parameters. The chosen structure for the dual-row TxArray coil enables the coil to act like a single-row degenerate birdcage TxArray coil [29, 30, 62, 63, 71-74] when the mesh currents of the adjacent elements in the axial direction cancel each other in the mid-ring segments of the coil. In the CP excitation mode, both rows are individually excited with identical power and linearly increasing phases, and the lower-row channels are excited with a 180° phase shift relative to the

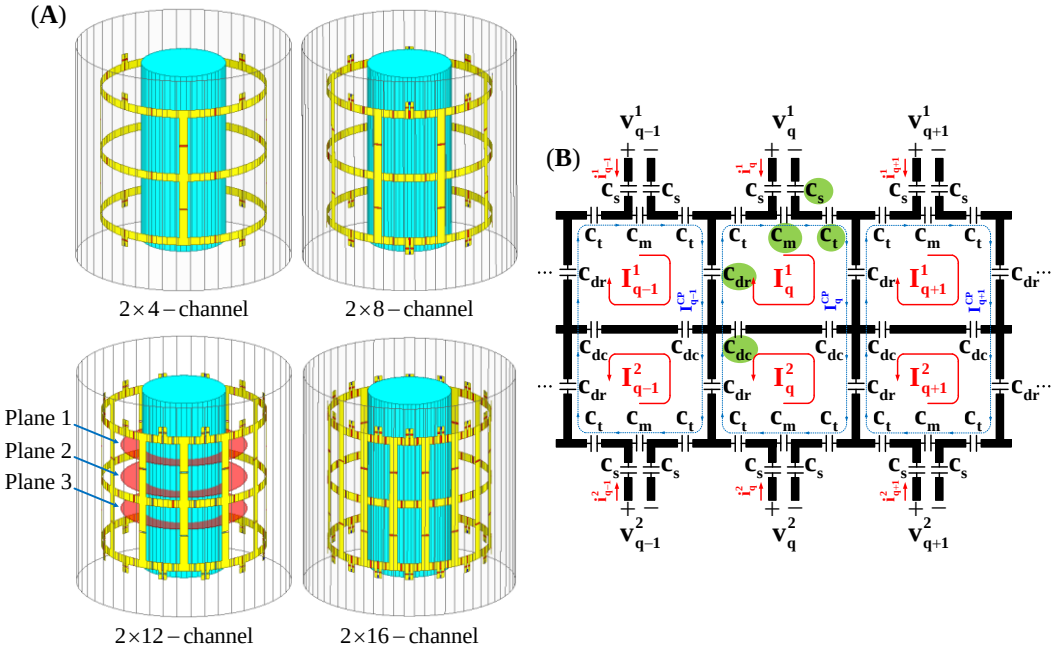

FIGURE 2.1 – (A) EM simulation models and (B) general schematic of dual-row degenerate birdcage TxArray coils. Three axial planes are shown in (A) to compare the TxArray coil fields. The port voltages and the mesh currents (the red trace) are shown in each of the loops. I_q^{CP} (the blue trace) denotes the mesh current of the CP excitation mode. All coils have the same dimensions, are enclosed with the same cylindrical RF shields, and are loaded by the same uniform cylindrical phantom.

upper-row channels. When the CP excitation is applied to this coil, it produces a field similar to a conventional birdcage coil with a rather uniform $\mathbf{B}_1^+$ field distribution in a large field-of-view.

2.4.3 Numerical simulations

Four shielded dual-row TxArray coils at 3T with 4, 8, 12, and 16 transmit channels in each row were designed and simulated (Figure 2.1). Additionally, four high-pass birdcage coils at 3T composed of 4, 8, 12, and 16 rungs connected at each end to two end-rings, as shown in Figure 2.2A, were simulated to compare the $\mathbf{B}_1^+$ patterns of the TxArray coils in the CP excitation mode with the traditional birdcage coils. The birdcage coils were tuned by capacitors distributed at the end-rings gaps (c_t) and matched to 50 Ω using two different capacitors: one at the top end-ring gap (c_m) connected in parallel to another capacitor (c_s) which is in series with an ideal voltage source (Figure 2.2B). The capacitors in the simulation of the high-pass birdcage coils were adjusted to produce a uniform magnetic field. However, the birdcage coils have

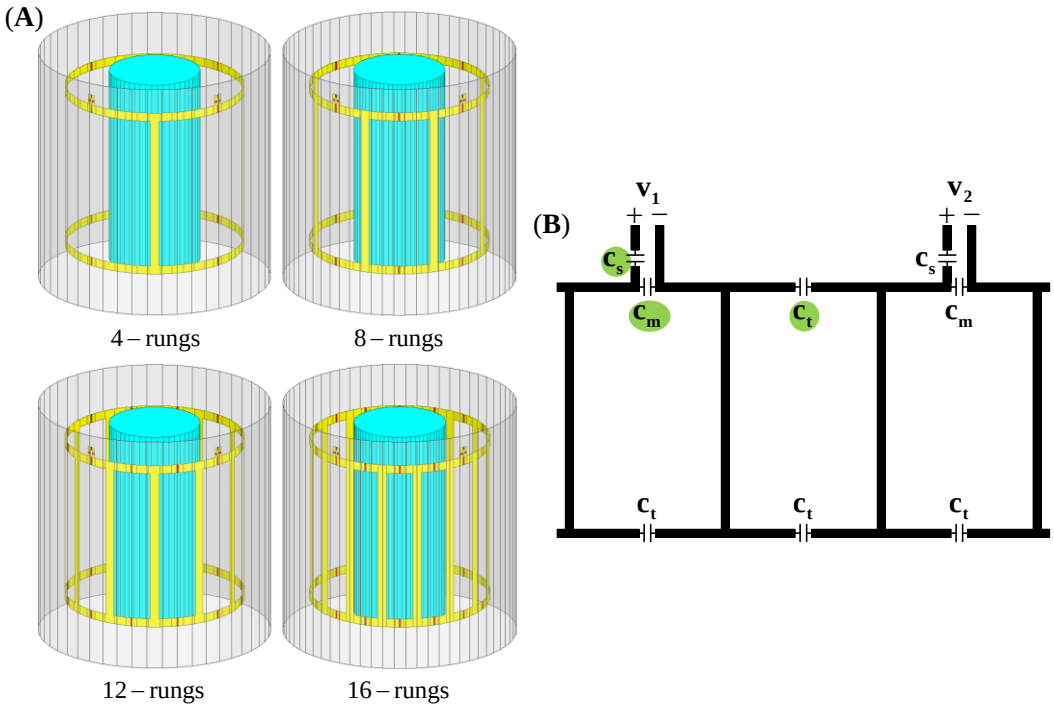

FIGURE 2.2 – (A) EM simulation models and (B) general schematic of four high-pass birdcage coils. All coils have the same dimensions, are enclosed with the same cylindrical RF shields, and are loaded by the same uniform cylindrical phantoms.

two decoupled ports on the top end-ring that were driven in the quadrature mode, where their ports were fed with the same amplitudes but with a 90° phase differential.

All TxArray coil and birdcage coils had a cylindrical geometry with the same dimensions (diameter of 315 mm, length of 270 mm, shield diameter of 408.9 mm, and shield length of 420 mm). All rings and legs were copper strips with a width of 15 mm. All coils shown in Figures 2.1-2.2 were loaded with a uniform cylindrical phantom with a diameter of 160 mm, a length of 350 mm, a conductivity of 0.6 S/m, and a relative permittivity of 80.

ANSYS Electronics Desktop 18.2 (ANSYS Inc., Canonsburg, PA, USA) was used to implement the numerical simulations at the operation frequency of 123.2 MHz. The conductors were modeled as good conductors [75], and the finite conductivity boundary was defined for them. A sphere with a radius greater than a quarter of the wavelength with the radiation boundary condition was defined as the outer surface of all simulations. Capacitors were adjusted based on the optimization method explained in the previous section using a combined finite element method and circuit analysis approach [76]. By substitution of all capacitors with equivalent lumped ports, the multiport **S**-matrices of the loaded TxArray coils were calculated in ANSYS HFSS. The multiport **S**-matrices were applied to perform the minimization problem, which was implemented in custom-written MATLAB 2018b scripts and obtain the optimal values of the capacitors. These MATLAB scripts are openly available in GitHub at https://github.com/UMRAM-Bilkent/Eigenmode-Analysis. In the next step, the multiport **S**-matrices were exported to ANSYS Designer. The updated port current and voltage values were pushed back to ANSYS HFSS to calculate the distributions of the electric and magnetic fields.

To obtain the capacitor values of the *2×4*-channel TxArray coil, all three different minimization cases of the λ-opt method were studied. The λ-opt (case#1) approach was also used to determine the coil performance as a function of the number of channels. To evaluate the performance of the proposed optimization strategy, both the λ-opt (case#1) and **S**-opt approaches were employed to optimize a *2×8*-channel TxArray coil. The capacitor values in the simulation of the TxArray coils and the high-pass birdcage coils are listed in Table 2.1.

TABLE 2.1 – Optimized capacitor values for the simulated TxArray coils and high-pass birdcage coils

Dual-row TxArray coils							
Capacitors	2×4-channel			2×8-channel		2×12-channel	2×16-channel
	λ-opt			λ-opt	**S**-opt	λ-opt	λ-opt
	case#1	case#2	case#3	case#1		case#1	case#1
c_{dr}	25.8 pF	25.8 pF	25.9 pF	41.2 pF	41 pF	43.5 pF	50.6 pF
c_{dc}	13.9 pF	14 pF	13.9 pF	27 pF	27.8 pF	39.9 pF	45.6 pF
c_t	13 pF	16 pF	12.8 pF	97.9 pF	29.3 pF	112.2 pF	161.8 pF
c_m	61.9 pF	25.2 pF	70.9 pF	18.1 pF	33.8 pF	31.1 pF	42 pF
c_s	65.7 pF	22.5 pF	70.2 pF	7.7 pF	23 pF	12 pF	13.2 pF

High-pass birdcage coils				
Capacitors	4-rung	8-rung	12-rung	16-rung
c_t	4.66 pF	13.36 pF	22.7 pF	32.27 pF
c_m	0.97 pF	3.68 pF	8 pF	13.46 pF
c_s	3.77 pF	10.36 pF	20.03 pF	28.34 pF

To obtain more information about the total transmitted power to each TxArray coil, the power loss in phantom and conductors, including the power-loss in the shield, were calculated. The capacitors are assumed to be lossless. The radiation loss was calculated as the difference between the total transmitted power and all other losses.

The $\mathbf{B}_1^+$ efficiency was evaluated as the average $\mathbf{B}_1^+$ within a region of interest for a unit total incident power. For comparison of the performance of the coils, the electromagnetic fields were recorded from three different axial planes that pass through the phantom, as shown in Figure 2.1A.

2.4.4 Measurements

To validate the simulations, the structure of a *2×4*-channel TxArray coil, which was supported by cylindrical plexiglass with a thickness of 3 mm and an outer diameter of 315 mm (Figure 2.3A), was constructed. The length of the coil was 270 mm, and all rings and legs were copper strips with a width of 15 mm. The coil's copper is broken into 56 different sections to distribute the capacitors. Due to practical limitations, the shield was built on another plexiglass in the shape of a right regular dodecagonal prism (Figure 2.3B). The shield is also constructed of copper strips on the outer side of the frame and slit in 12 equally spaced rectangular sections with dimensions of 105.5×480 mm^2 along the axial direction to reduce gradient-induced eddy currents [77]. The neighboring slits were connected with three 2 nF capacitors at positions that face rings

of the coil. The strip thickness in both the coil and the shield was 35 μm. The coil was loaded with a cylindrical SNR phantom (3.7 g/L $NiCl_2.6H_2O$ and 2.4 g/L NaCl) with a diameter of 153 mm. Magnetic resonance electrical properties tomography (MREPT) [78] was used to measure the conductivity of the phantom as 0.62 S/m. Its relative permittivity was assumed to be equivalent to that of water [79, 80].

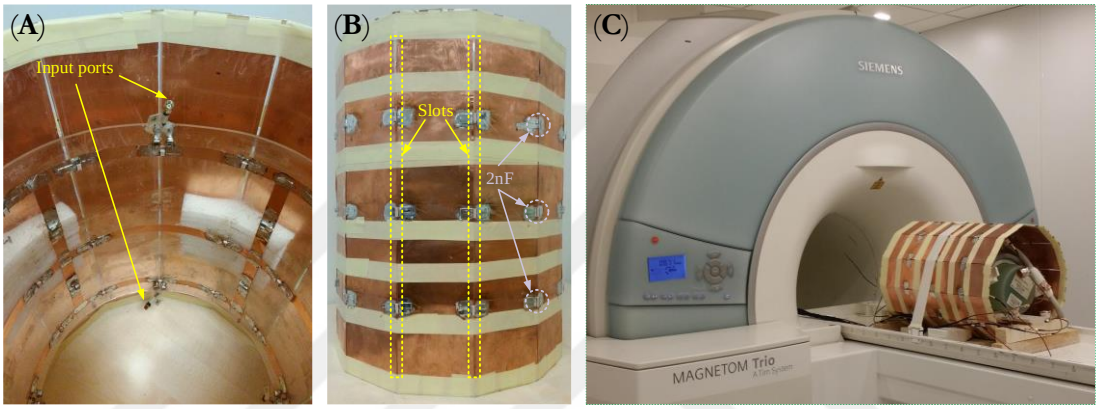

FIGURE 2.3 – Experimental setups. (A) A *2×4*-channel degenerate birdcage head TxArray coil that was designed and constructed using the proposed method. (B) An RF shield with several parallel slots placed on plexiglass in the shape of a right regular dodecagonal prism. (C) An overview of the TxArray coil inside the scanner. The coil is loaded with the sodium-nickel solution phantom, and the body-matrix coil of the Siemens scanner is used to pick up the MR signals.

To estimate the capacitor values needed for the fabricated coil, an identical loaded *2×4*-channel TxArray coil with the same 2 nF capacitors on its shield was simulated. The capacitor values (Table 2.2) were obtained using the λ-opt (case#1) method. Note that the optimal capacitors determined by the simulation were finely tuned in the fabricated coil to minimize the error between the simulated and measured reflection coefficients, λ_{av}, and λ_{CP} at 123.2 MHz.

TABLE 2.2 – Optimized capacitor values for the fabricated and simulated *2×4*-channel TxArray coils

Capacitors	c_{dr}	c_{dc}	c_t	c_m	c_s
Fabricated TxArray coil	25.7 pF ± 0.2 pF	14.6 pF ± 0.2 pF	14.6 pF ± 0.2 pF	51.6 pF ± 0.2 pF	51.9 pF ± 0.2 pF
Simulated TxArray coil	26.4 pF	14.1 pF	13.3 pF	56.6 pF	57 pF

A calibrated Agilent E5061B vector network analyzer was used to measure the scattering parameters of the coil. All MR experiments were conducted using a 3T scanner (Magnetom Trio, A Tim System, Siemens Healthcare, Erlangen, Germany) that was equipped with 8 transmit array channels. Each channel utilized a separate amplifier (Analogic Corp., Boston, MA, USA) with adjustable power output with maximum peak power of 8 kW. Accordingly, eight coaxial cables with adjusted bazooka baluns were used to carry the RF power from the amplifiers to the TxArray coil. The TxArray coil was utilized only in transmit mode without any detuning circuits. A Siemens body-matrix coil, which is a 6-channel standard flexible surface coil with six integrated preamplifiers, was used as the receive coil. The possible receive performance degradation due to the lack of detuning circuits did not affect the proof of principle experiments of this chapter.

A method based on the Bloch-Siegert shift [81, 82] was used to acquire the $\mathbf{B}_1^+$-map at the central axial plane of the coil. The Bloch-Siegert shift was applied by a modified gradient-echo (GRE) pulse sequence to spins by an off-resonance Fermi pulse. The duration and the off-resonance frequency were respectively 8 ms and 2 kHz. The other relevant imaging parameters were TR/TE = 100 ms/12 ms, slice thickness = 5 mm, matrix = 128 × 128, FOV = 300 mm, and # of averages = 1. A mask with a threshold of one-tenth of the maximum $\mathbf{B}_1^+$ value was applied to the $\mathbf{B}_1^+$-map to minimize the effect of unreliable data (low-SNR).

2.5 Results

2.5.1 Simulation results

The performance of all four TxArray coils at 123.2 MHz tuned by the different minimization approaches is summarized in Table 2.3. In this table, all the λ_n values, λ_{CP}, reflection coefficients, and maximum coupling levels, and $\mathbf{B}_1^+$ efficiencies in the CP excitation mode are provided for different solutions. The simulation results based on the λ-opt (case#1) approach revealed that the ability to match and decouple the TxArray coils decreases as the number of transmit channels increases, indicated by an increase in the average of modal reflected power values, λ_{av}. Note that this value is also equal to $\frac{1}{N}\sum_{n=1}^{N}\sum_{m=1}^{N}|s_{mn}|^2$. On the other hand, the CP mode $\mathbf{B}_1^+$ efficiency remains

unchanged since λ_{CP} was kept reasonably low for all four TxArray coils. For TxArray coils with 8, 16, 24, and 32 transmit channels, 1, 7, 11, and 20 of the excitation eigenmodes have a very high modal reflected power (> 0.93), respectively; therefore, these modes hardly contribute to the transmission process. 7, 9, 8, and 8 of the excitation eigenmodes have a total reflection of less than 50% for coils with 8, 16, 24, and 32 channels, respectively. These modes can be regarded as efficient eigenmodes of the TxArray coils, which can span the excitation space with low total reflection, and

TABLE 2.3 – Summary of the performance of the simulated TxArray coils designed based on the different minimization approaches

Minimization approach	2×4-channel			2×8-channel				2×12-channel			2×16-channel			
	λ-opt			λ-opt		S-opt		λ-opt			λ-opt			
	case#1	case#2	case#3	case#1				case#1			case#1			
$\lambda_1, \lambda_2, ..., \lambda_N$	**0.02**	**0.01**	**0.04**	**0.10**	**0.42**	**0.06**	0.65	**0.05**	0.61	0.99	**0.07**	**0.50**	0.98	1.00
	0.02	**0.01**	**0.04**	**0.10**	0.98	**0.06**	0.97	**0.05**	0.61	1.00	**0.07**	0.60	0.98	1.00
	0.09	**0.05**	**0.08**	**0.10**	0.98	**0.15**	0.98	**0.34**	0.63	1.00	**0.40**	0.60	0.98	1.00
	0.09	**0.05**	**0.16**	**0.10**	0.99	**0.15**	0.98	**0.34**	0.74	1.00	**0.40**	0.84	0.99	1.00
	0.14	**0.28**	**0.17**	**0.24**	0.99	**0.50**	0.98	**0.49**	0.75	1.00	**0.43**	0.93	0.99	1.00
	0.22	**0.37**	**0.17**	**0.24**	1.00	**0.50**	1.00	**0.50**	0.97	1.00	**0.44**	0.93	1.00	1.00
	0.30	**0.45**	**0.18**	**0.40**	1.00	0.63	1.00	**0.50**	0.98	1.00	**0.48**	0.98	1.00	1.00
	0.99	0.98	0.99	**0.40**	1.00	0.63	1.00	**0.50**	0.99	1.00	**0.48**	0.98	1.00	1.00
$\lambda_{av} = \frac{1}{N}\sum_{n=1}^{N}\lambda_n$	0.23	0.27	0.23	0.56		0.64		0.71			0.78			
λ_{CP}	0.09	0.01	0.17	0.10		0.15		0.05			0.07			
s_{mm} (dB)	-23.4	-14.7	-19.7	-9.9		-15.1		-7.7			-5.5			
$\max\{\lvert s_{mn} \rvert\}\big\rvert_{m\neq n}$ (dB)	-12.3	-10.8	-12.2	-5.9		-4.7		-6.8			-8.4			
$\mathbf{B}_1^+$ efficiency in the CP mode at Plane 2 ($\mu T/\sqrt{W}$)	0.63	0.65	0.58	0.63		0.58		0.64			0.64			

their corresponding eigenvalues are shown in bold in Table 2.3. While the number of efficient eigenmodes remains relatively constant as the number of channels increases, the ratio of efficient eigenmodes to all excitation eigenmodes decreases significantly. For coils with 8, 16, 24, and 32 channels, respectively, 88%, 56%, 33%, and 28% of the eigenmodes can be accessed efficiently ($\leq$ 50%), which indicates that adding channels does not necessarily lead to a proportional increase in the degrees of freedom.

The results (Table 2.3) also demonstrate that the solution obtained for the *2×8*-channel TxArray coil by the **S**-opt approach increases λ_{CP} substantially (by 50%) compared to the solution obtained by the λ-opt method. The increase in λ_{av} and decrease in $\mathbf{B}_1^+$ efficiency are not very significant (13% and 9%, respectively). Also, nine excitation eigenmodes with a total reflection of less than 50% are available with the solution acquired by the λ-opt (case#1) approach. In contrast, in the solution obtained by the **S**-opt approach, only six eigenmodes have this property indicating that the λ-opt method significantly enlarges the excitation space. For some applications that require more transmitted power or under some hardware limitations, a lower threshold value of modal reflected power can be considered for determining the excitation space. Considering an excitation space with a total reflection of less than 40% shows that eight eigenmodes were available with the solution acquired by the λ-opt approach. In contrast, the **S**-opt approach offered only four excitation eigenmodes.

On the other hand, three different solutions of the λ-opt approach obtained for the *2×4*-channel TxArray coil have shown that limiting λ_{CP} to less than 0.01 (case#2) can increase λ_{av} significantly (by 18%). Dropping out λ_{CP} in the minimization problem (case#3) did not cause a significant change in λ_{av}. The *2×4*-channel TxArray coil has only one excitation eigenmode with a reflection of more than 98% when any of the λ-opt approaches are used. Therefore, the usage of the different cases did not alter the dimension of the excitation space. Furthermore, λ_{CP} was changed significantly with the use of different cases. The results have also shown that the *2×4*-channel TxArray coil is capable of acceptable levels of matching and decoupling.

Figure 2.4 demonstrates the normalized reflected power, the total delivered power to the phantom, and the $\mathbf{B}_1^+$ efficiency of four dual-row TxArray coils and four high-pass birdcage coils, all of which are derived in the CP excitation mode. The TxArray coils were designed based on the λ-opt (case#1) approach. As the number of channels increases in the TxArray coils, λ_{av} increases, while λ_{CP} remains less than 10%, which

is slightly worse than the high-pass birdcage coils. As can be seen in Figure 2.4B, more than 87% and 95% of the total incident power is delivered to the phantom for the TxArray coils and the high-pass birdcage coils, respectively, when they are used in the CP mode. The $\mathbf{B}_1^+$ efficiencies of the TxArray coils and high-pass birdcage coils derived in the CP mode were also very similar (more than 0.62 $\mu T/\sqrt{W}$ and 0.65 $\mu T/\sqrt{W}$, respectively). Note that the slight difference between the CP performance of the TxArray coils and birdcage coils can be eradicated when the λ-opt (case#2) method is used, as can be seen in Figure 2.6 for the *2×4*-channel TxArray coil.

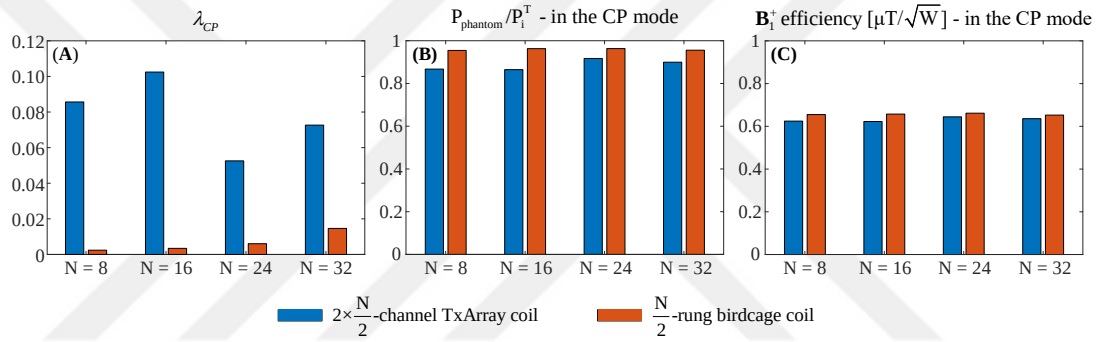

FIGURE 2.4 – (A) Normalized reflected power, (B) total delivered power to the phantom, and (C) $\mathbf{B}_1^+$ efficiency of *N*-channel TxArray coil and *N*/2-rung high-pass birdcage coil, which were both derived in the CP excitation mode with *N* = 8, 16, 24, and 32. The *N*-channel TxArray coils were designed based on the λ-opt (case#1) approach.

The results shown in Figures 2.5-2.9 are obtained by simulating the *2×4*-channel TxArray coil with the capacitors determined based on the λ-opt (case#2) approach. Figure 2.5 shows the surface current density on the TxArray coil and the $\mathbf{B}_1^+$-patterns within the phantom at three different axial planes, i.e., Planes 1, 2, and 3 shown in Figure 2.1A, when the coil was driven in the CP excitation mode. The results are normalized by the square root of the total incident power. In the CP mode, the current on the middle-ring of the TxArray coil is almost zero. The results show that a stronger $\mathbf{B}_1^+$-pattern is generated in Plane 2 compared with Planes 1 and 3 in the CP excitation mode, similar to the $\mathbf{B}_1^+$-pattern generated by a conventional birdcage coil.

Figure 2.6 also shows the $\mathbf{B}_1^+$ and electric field patterns of the TxArray coil together with a 4-rung high-pass birdcage coil in the CP excitation mode normalized by the square root of the total incident power. Both coils generate almost identical field patterns.

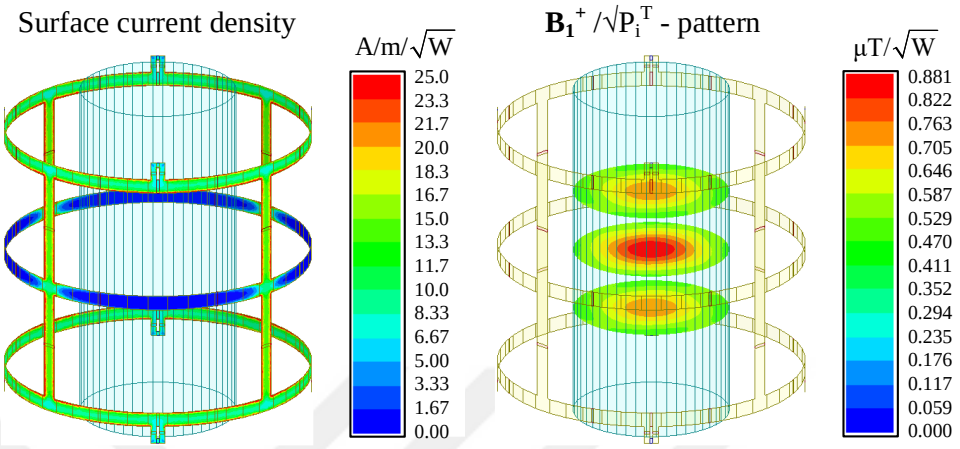

FIGURE 2.5 – Surface current density of the *2×4*-channel TxArray coil designed based on the λ-opt (case#2) approach and the $\mathbf{B}_1^+$-patterns within the phantom for the CP excitation mode at three different axial planes. Surface current densities and $\mathbf{B}_1^+$-patterns are normalized by the square root of the total incident power.

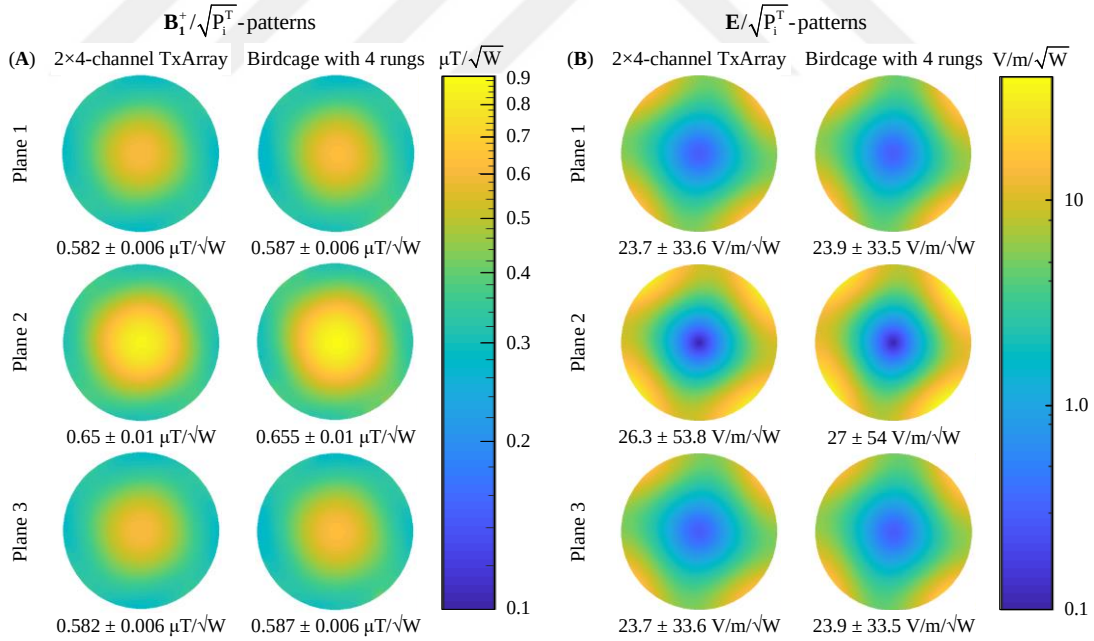

FIGURE 2.6 – (A) $\mathbf{B}_1^+$ and (B) electric field patterns of the *2×4*-channel TxArray coil designed based on the λ-opt (case#2) approach and the *4*-rung high-pass birdcage coil within the phantom at three different axial planes when both coils were driven in the CP excitation mode. The field patterns are normalized by the square root of the total incident power.

In Figure 2.7, the phantom's dielectric constant was changed between 20 and 80 to investigate the field focusing effect in the *2×4*-channel TxArray coil. The coil was simulated for each dielectric constant without changing the capacitor values. Figure

2.7A shows the $\mathbf{B}_1^+$-patterns within the phantom at the central axial plane (Plane 2) when the coil is derived in the CP excitation mode. Also, the field patterns reported in this figure are normalized by the square root of the total incident power. For easier comparison, Figure 2.7B displays the normalized $\mathbf{B}_1^+$ field along the x-axis (red dashed line shown in Figure 2.7A). The $\mathbf{B}_1^+$-patterns for different dielectric constants demonstrate that a decrease in dielectric constant leads to a smaller field-focusing effect, and thus the $\mathbf{B}_1^+$ distribution becomes more uniform. As the dielectric constant increases, significant variation in the field patterns can be observed between the center and the surrounding area. This is another indication of the birdcage coil-like behavior of the TxArray coil.

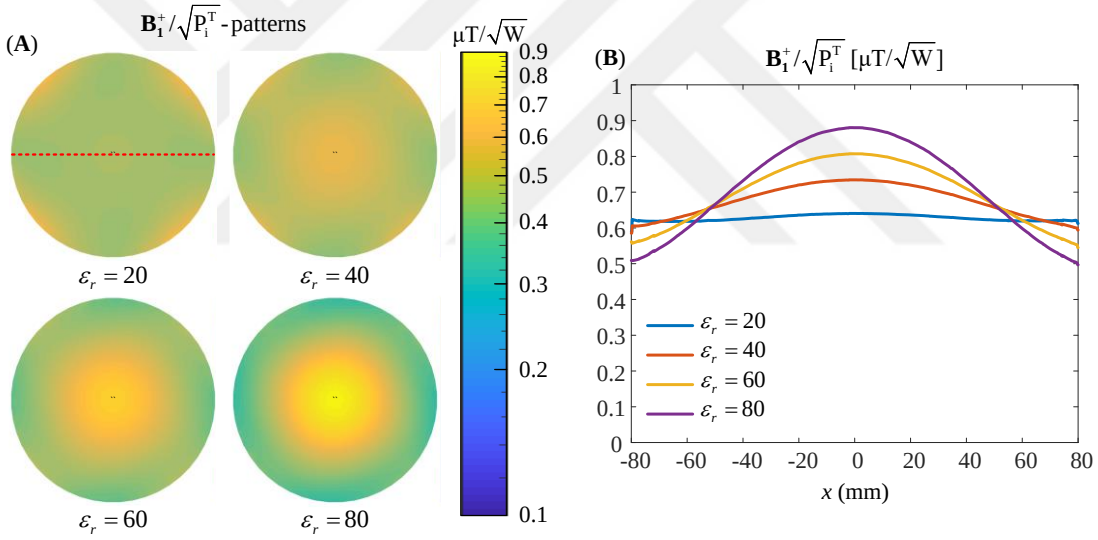

FIGURE 2.7 – (A) $\mathbf{B}_1^+$-patterns of the 2×4-channel TxArray coil designed based on the λ-opt (case#2) approach within the phantom at the central axial plane (Plane 2) when the coil was derived in the CP excitation mode. (B) $\mathbf{B}_1^+$ field distributions at y = 0. The field patterns are normalized by the square root of the total incident power.

Figure 2.8 shows the $\mathbf{B}_1^+$ and electric field patterns of all eight excitation eigenmodes of the *2×4*-channel TxArray coil within the phantom at three different axial planes (Figure 2.1A). For comparison, the $\mathbf{B}_1^+$ and **E** field patterns of the CP excitation mode are also shown in this figure. The field patterns are normalized by the square root of the total transmitted power. The results indicate that the first and second excitation eigenmodes produce linear fields that are perpendicular to each other. The fields generated by the CP excitation mode are mainly the quadrature combination of these two field patterns.

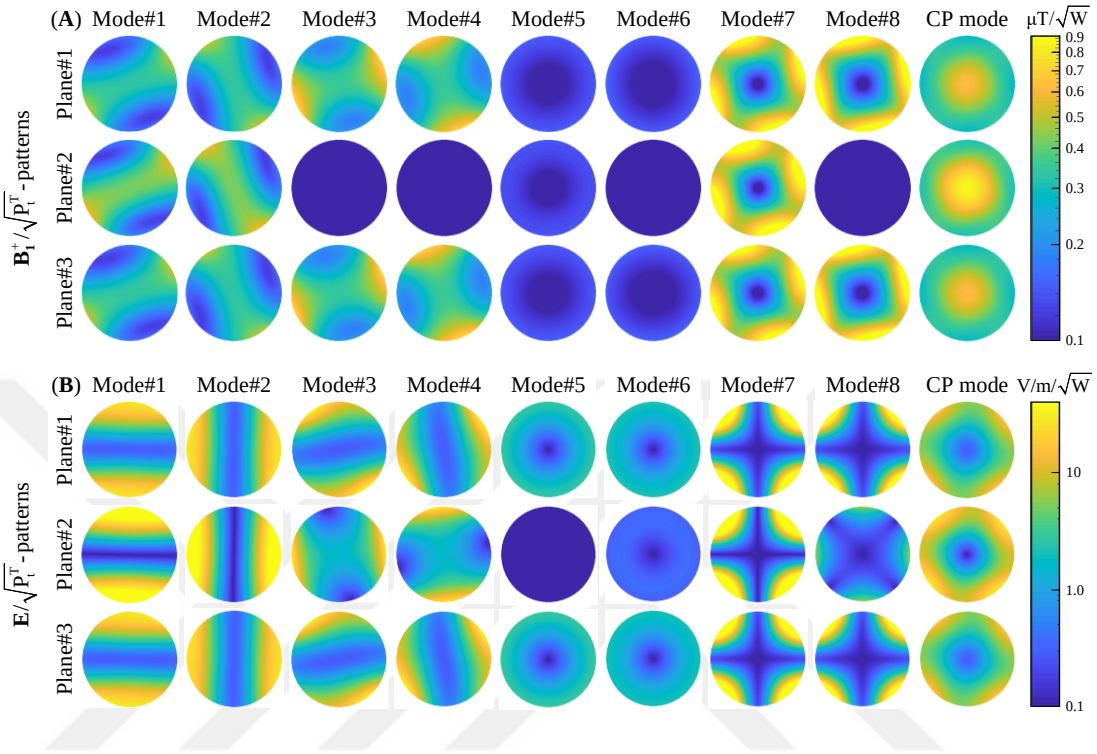

FIGURE 2.8 – (A) $\mathbf{B}_1^+$ and (B) electric field patterns of the *2×4*-channel TxArray coil designed based on the λ-opt (case#2) approach within the phantom for all excitation eigenmodes, and the CP excitation mode at Planes 1, 2, and 3. The field patterns are normalized by the square root of the total transmitted power.

Figure 2.9 indicates where the total incident power is consumed for each eigenmode. For comparison, this figure also shows the power analysis of the CP mode of excitation. The total reflected power increases in higher modes for a constant total

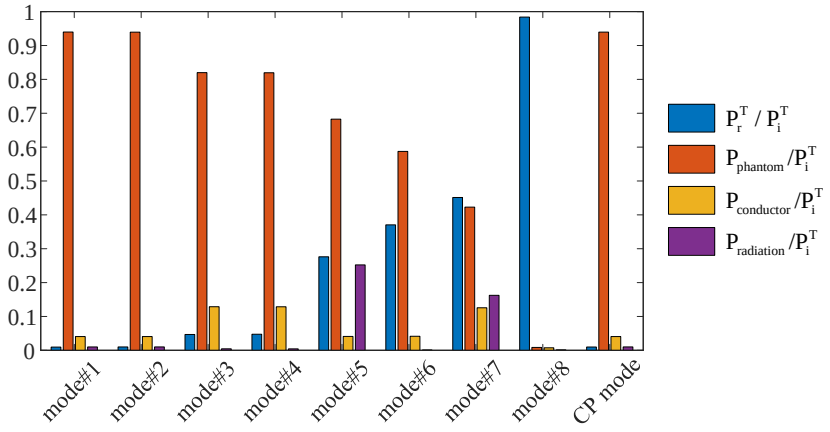

FIGURE 2.9 – Power analysis of the *2×4*-channel TxArray coil designed based on the λ-opt (case#2) approach for the excitation eigenmodes and the CP excitation mode.

incident power, which causes less power transmission to the TxArray coil. The delivered power to the phantom is also decreased because of lower accepted power in higher modes. For the CP excitation mode, less than 1% of the incident power is reflected; 94% of the incident power is delivered to the phantom. In this mode, only 4% of the incident power is dissipated in the coil conductors, and 1% of the incident power is radiated.

The sensitivity of the *2×4*-channel TxArray coil to the conductivity and diameter of the phantom is shown in Tables 2.4-2.5. The conductivity of the phantom was changed between 0.48 S/m and 0.72 S/m to investigate its effect on the eigenvalues. Without changing the values of the capacitors, the λ_n values of the *2×4*-channel TxArray coil designed based on the λ-opt (case#1) approach were found for each conductivity value. Table 4 summarizes the sensitivity analysis of the eigenvalues to the conductivity of the phantom. 10% and 20% variations in the conductivity resulted in 6.5% and 12.1% maximum changes in λ_{av}, respectively, 39.5% and 57% changes in λ_{CP}, respectively.

TABLE 2.4 – Sensitivity of the eigenvalues to the conductivity of the phantom

Conductivity (σ) (S/m)	0.48	0.54	0.60	0.66	0.72
$\lambda_1, \lambda_2, ..., \lambda_N$	0.02	0.01	0.02	0.01	0.01
	0.02	0.01	0.02	0.01	0.01
	0.13	0.08	0.09	0.05	0.04
	0.13	0.09	0.09	0.05	0.04
	0.17	0.16	0.14	0.14	0.14
	0.25	0.25	0.22	0.24	0.24
	0.39	0.39	0.30	0.32	0.31
	0.99	0.99	0.99	0.99	0.99
λ_{av}	0.26	0.25	0.23	0.23	0.22
λ_{CP}	0.13	0.09	0.09	0.05	0.04
s_{nn} (dB)	-23.6	-18.1	-23.4	-17.2	-16.2
$\max\{\lvert s_{mn} \rvert\}\big\rvert_{m \neq n}$ (dB)	-11.6	-12.1	-12.3	-12.7	-13.1

The *2×4*-channel TxArray coil loaded with a phantom with various diameters were tested to assess the eigenvalue sensitivity to the load diameters. The capacitor values of the coil were optimized by the λ-opt (case#1) approach. Table 5 summarizes the sensitivity of the eigenvalues to the diameter of the phantom. The results indicate that λ_{av} and λ_{CP} may vary between 0.46 and 0.18 and between 0.22 and 0.08, respectively, when the phantom diameter changes between 128 mm and 192 mm. λ_{av} tends to decrease with an increase in the load diameter.

TABLE 2.5 – Sensitivity of the eigenvalues to the phantom diameter					
Phantom diameter (mm)	128	144	160	176	192
$\lambda_1, \lambda_2, ..., \lambda_N$	0.22	0.08	0.02	0.01	0.01
	0.22	0.08	0.02	0.01	0.02
	0.22	0.14	0.09	0.04	0.05
	0.22	0.14	0.09	0.08	0.05
	0.51	0.31	0.14	0.08	0.06
	0.59	0.39	0.22	0.11	0.13
	0.72	0.53	0.30	0.12	0.13
	0.99	0.99	0.99	0.98	0.97
λ_{av}	0.46	0.33	0.23	0.18	0.18
λ_{CP}	0.22	0.14	0.09	0.08	0.13
s_{nn} (dB)	-12.4	-18.5	-23.4	-15.3	-10.9
$\max\{\lvert s_{mn} \rvert\}\big\rvert_{m \neq n}$ (dB)	-9.5	-10.5	-12.3	-14.1	-16.3

2.5.2 Measurement results

Figure 2.10A-B provides the simulated and measured **S**-matrix of the loaded *2×4*-channel TxArray coil that was designed based on the λ-opt (case#1) approach, which demonstrates a matching level of at least 13.5 dB and decoupling greater than 10.5 dB. Furthermore, Figure 2.10C illustrates the error matrix that is defined as the difference between the simulated and measured **S**-matrix and computed as $|\mathbf{S}_{simulated} - \mathbf{S}_{measured}|$. Figure 2.10D-E shows the simulated and measured reflection coefficients and λ_{av} as a function of the frequency. The difference in the matching and decoupling levels observed between the simulated coil and fabricated coil can be attributed to the imperfections in the construction of the coil. Figure 2.10F illustrates the simulated and measured modal reflected power values. For comparison, this figure also shows λ_{CP}. Figure 2.10E-F reveals that the measured λ_{CP} is in good agreement with the simulated λ_{CP}.

Figure 2.11 compares the $\mathbf{B}_1^+$ field patterns of the fabricated and simulated *2×4*-channel TxArray coil at the central axial plane (Plane 2) when both coils are derived in the CP excitation mode. Phase/magnitude shimming was not performed in the measured $\mathbf{B}_1^+$-pattern. As indicated in Figure 2.10 for the manufactured coil, the performances of all eight transmit channels are not precisely the same; therefore, the mode generating the best CP excitation profile for the fabricated coil will not be the same as that defined for the simulated coil. Note that the correct CP excitation mode

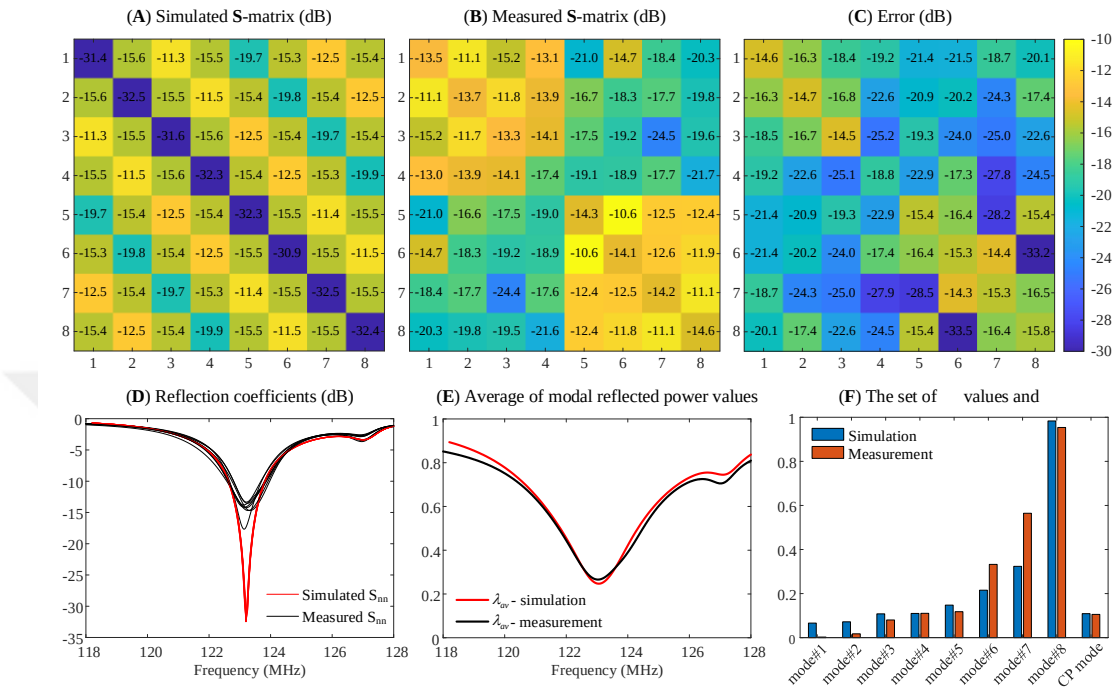

FIGURE 2.10 – (A) Simulated and (B) measured scattering parameter matrices of the loaded *2×4*-channel TxArray coil designed based on the λ-opt (case#1) approach at 123.2 MHz. (C) The difference between the simulated and measured **S**-matrix. (D) Reflection coefficients and (E) λ_{av} as a function of frequency. (F) The modal reflected power values of the TxArray coil at 123.2 MHz. For a comparison, part (F) also shows λ_{CP}.

of the fabricated coil cannot be found by merely evaluating the measured scattering parameters.

2.6 Discussion and conclusion

In this chapter, the normalized reflected power was defined and used as the ratio of the total reflected power to the total incident power to analyze the transmitting capabilities of TxArray coils. The excitation eigenmodes (the eigenvectors of $\mathbf{S^HS}$) was presented as an orthogonal basis for the TxArray coil excitation. The eigenvalues of $\mathbf{S^HS}$, λ_n, were named as the modal reflected power values. It was shown that the normalized reflected power for an arbitrary excitation set, $\lambda(\mathbf{a})$, can be quantified as the weighted sum of the λ_n values, which implies that the λ_n values fully characterize the transmission capabilities of the TxArray coil.

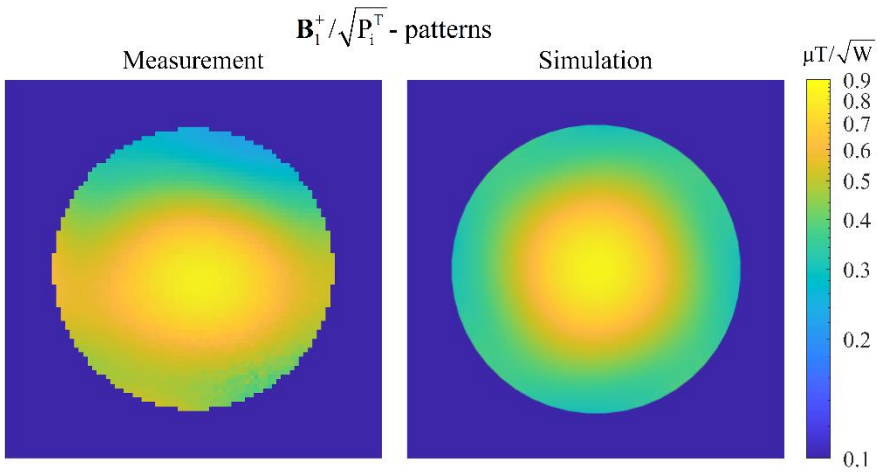

FIGURE 2.11 – Measured (left) and simulated (right) $\mathbf{B}_1^+$-patterns of the CP excitation mode at the central axial plane (Plane 2) for the fabricated and simulated *2×4*-channel TxArray coil designed based on the λ-opt (case#1) approach. The field patterns are normalized by the square root of the total incident power. In the measured $\mathbf{B}_1^+$-pattern, phase/magnitude shimming was not performed.

In the literature for general antenna arrays, the concept of the *total active reflection coefficient (TARC)* [83-85] is used. The magnitude square of TARC is equal to the modal reflected power; therefore, these concepts can be used interchangeably.

Ideally, zero total reflected power for all possible excitation sets is needed to design an ideal TxArray coil that corresponds to a zero set of λ_n values, which is possible only if the coil has a zero **S**-matrix. This is also the ideal design target to achieve perfect matching and decoupling levels. Due to the practical imperfections, **S**-matrix cannot be zero; therefore, optimization algorithms can be configured and run to minimize the **S**-matrix elements. In current practice, the magnitude of **S**-matrix elements is minimized to match and decouple a TxArray coil. However, minimizing **S**-matrix elements does not necessarily minimize the λ_n values because, apart from the amplitude, the **S**-matrix phase is also effective in determining the λ_n values. The proposed eigenmode analysis looks at the **S**-matrix as a whole, captures more than just looking at the **S**-matrix elements individually. Hence, the minimization of the λ_n values is a convenient approach for the design of TxArray coils.

The eigenmodes with high modal reflected power values hardly contribute to the transmission process and can, to a certain degree, be considered inefficient and

impractical. The eigenmode analysis thus provided insight to determine the optimum number of transmit elements. Hence, the number of efficient eigenmodes might be considered as a critical metric to compare the performance of various TxArray coils. Therefore, this chapter focused mainly on designing TxArray coils by increasing the number of efficient eigenmodes. The set of eigenmodes that has low reflection is considered as the excitation space of the TxArray coil. In the design process, an attempt is made to expand the excitation space. Although there seems to be a limit in this, the coverage of this space can be modified. In the example designs of this chapter, it is ensured that CP excitation lies within this space. It should be noted without limiting λ_{CP}, there are many design possibilities for the TxArray coils proposed in this chapter in which the CP mode does not lie within the low reflection excitation space. The future users of the proposed algorithm may add additional modes to the optimization process that are significant for the specific design.

For a predesigned TxArray coil, categorizing the efficient and inefficient eigenmodes limits the excitation space to the subset of eigenmodes. In this chapter, 50% was considered as a reasonable number for this limit. In practice, this limit should be defined by the hardware limitations of the overall system, including the available power and the amount of tolerable reflected power. If users, for example, want to conduct RF shimming, the knowledge of the excitation space enables users to achieve a proper shim more rapidly within the power limits of the amplifiers.

Assessment of the total power absorbed by the phantom is critically essential. The total absorbed power by the object of interest and the conductor and radiation losses cannot be distinguished by merely assessing the scattering parameters. In the electromagnetic simulation, careful integration within the phantom is necessary. Furthermore, maximizing the power delivered to the object is not directly linked to generating the desired $\mathbf{B}_1^+$ field. Linking the excitation space to these parameters is the subject of future research.

Although in this chapter, an eigenmode analysis was conducted for the **S**-matrix of TxArray coils, it was used earlier for other parameters. For example, the eigenmode analysis was applied to evaluate the signal-to-noise ratio (SNR) behavior of receive array coils [86, 87], to improve parallel imaging performance [88], and to attain a homogeneous transmit excitation with low levels of SAR at ultra-high field MRI [89].

In this chapter, however, the eigenmode analysis is used to obtain power-efficient operation modes of TxArray coils.

In this chapter, the performance of a dual-row TxArray coil was examined as an example to evaluate the effectiveness of the eigenmode analysis. The results demonstrated that the structure chosen for the dual-row TxArray coil could act like a single-row degenerate birdcage TxArray coil by providing the CP excitation field patterns under certain circumstances (Figure 2.5). Consequently, this coil enables us to benefit from the advantages of the parallel transmit technology without losing the advantages of the conventional birdcage coil to obtain rather homogeneous excitation patterns in a large volume.

For the analysis and design of the TxArray coils, the use of the modal reflected power concept is introduced. The capacitor values were found by using the newly developed λ-opt approach. In this approach, the λ_n values were minimized to increase the dimension of the excitation space (a subspace composed of the excitation eigenmodes with low total reflected power values). Additionally, the total reflected power for some critical modes of operations, such as the CP excitation mode, can be incorporated as a constraint in the optimization process. To examine the impact of the added constraint and weighting coefficients on the coil performance, three different minimization cases of the λ-opt approach were employed. To validate the effectiveness of the λ-opt approach, the optimal design performance of a dual-row TxArray coil achieved by the λ-opt method was compared with the optimal design obtained by the conventional minimization approach (**S**-opt). The results showed that the proposed algorithm could increase excitation space, and some critical modes of operations can be achieved without significant reflection.

Chapter 3

A Fast Fine-tuning Method for Designing an Imperfectly Manufactured Transmit Array Coil using its Equivalent Circuit Model

3.1 Preface

The content of this chapter has been partially presented at the International Society of Magnetic Resonance in Medicine (ISMRM)'s 26th and 28th Annual Scientific Meetings [71, 74]. Ergin Atalar was involved in conceptualizing the content of this chapter and in its methodology.

3.2 Introduction

Various methods have been employed in simulation environments to design radiofrequency (RF) transmit array (TxArray) coils and study their interactions with subjects under test, falling primarily within two major categories, including quasi-static [90, 91] and full-wave [92-99] electromagnetic models. Full-wave modeling approaches are more accurate than quasi-static modeling approaches, although they are more time consuming [100]. In the performance optimization of a TxArray coil, the use of full-wave simulations alone becomes an enormously limiting factor, as a full-wave simulation needs to be performed for each tuning condition. Co-simulation

strategy [76] can vastly speed up the analysis of a TxArray coil. This process replaced all lumped components with equivalent lumped-ports and calculated TxArray coils multi-port scattering matrices to determine the optimal lumped-elements in a short time through an RF optimizing tool.

Typically, the full-wave simulation results are not matched with the measurement results very well, in particular for imperfectly manufactured TxArray coils. It is thus challenging to predict the optimum lumped-elements of the manufactured coils. The vast majority of coil designers initially utilize the lumped-element values obtained from the simulation, along with some added variable components. They perform the fine-tuning and matching process and attempt to reduce the difference between the simulation and experimental results [62, 101]. In this process, the array elements iteratively can be tuned and matched one by one in successive steps. This approach is a time-consuming process, becoming more unfeasible when the number of array elements increases.

In this chapter, manufactured TxArray coils are to be modeled using lumped-elements and distributed models. It is proposed to measure the fabricated coil's scattering parameters by assembling the simulated coil's optimal lumped-elements to predict all unknown elements of the coil's equivalent circuit model. Adjusting the free design parameters that are integrated with circuit models could result in the proper design of manufactured TxArray coils. This process can be considered as a novel practical coil design approach to reduce the difference between the experimental and simulation results caused by the imperfection in coil's manufacturing. Although equivalent circuit models were previously used to find the optimal lumped-elements of the simulated array coils [51, 71, 73, 102-104], they were never used before in the development of manufactured array coils.

Here, the performance of simulated and manufactured 8-channel TxArray coil with capacitively decoupled channels for a 3T MRI system is evaluated. Fine-tuning and matching of this coil are laborious as adjusting one coil's channel will affect the performance of other channels; therefore, special attention needs to be paid to include the exact structure of the fabricated TxArray coil in the design process. The equivalent circuit model of the fabricated TxArray coil by considering all magnetic and electrical couplings [51, 104, 105] was utilized to determine all inductance and resistance values, which are required for organizing the circuit model. The design approach presented in

Chapter 2, which is based on the eigenmode analysis of the scattering matrix (**S**-matrix) [49, 50] is used to obtain the optimum capacitor values. The capacitor values are optimized to expand the excitation space of the TxArray coil with a low level of total reflected power.

3.3 Theory and methods

3.3.1 Simulated TxArray coil

Figure 3.1 displays the model and schematic of the simulated 8-channel degenerate birdcage TxArray coil. The coil has a cylindrical shape with a diameter of 315 mm and a length of 300 mm and comprises of eight transmit channels of the same dimensions. The width of all end-rings and rungs is 15 mm. The coil is shielded with a cylinder with a diameter of 412 mm and a length of 500 mm. The shield is slit into eight segments evenly distributed along the axial direction to decrease eddy current induced by gradient fields [77], where the adjacent slits are connected via two 3 nF capacitors at positions facing the coil's end-rings. A cylindrical phantom placed in the center of the coil with a conductivity of 0.62 S/m, a relative permittivity of 80, a diameter of 153 mm, and a length of 350 mm is then used to load the coil.

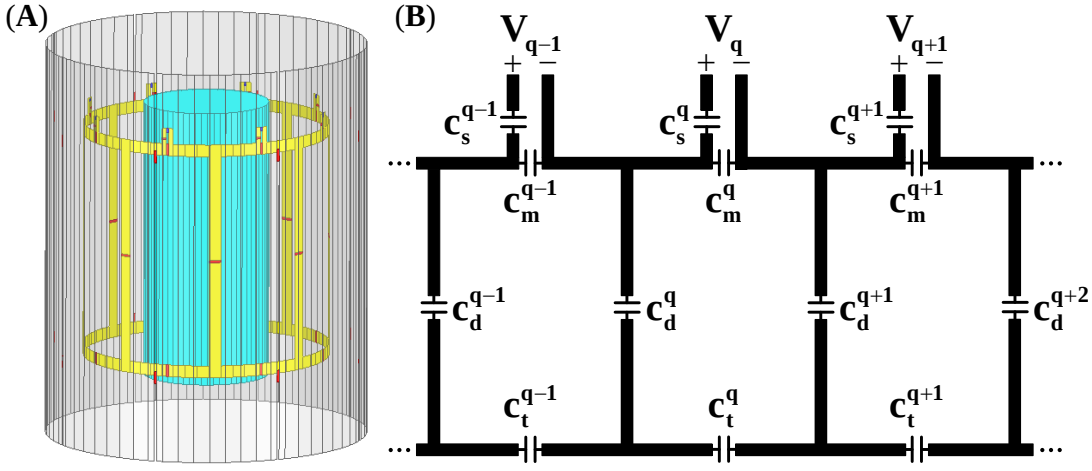

FIGURE 3.1 - (A) Electromagnetics (EM) simulation model and (B) schematic of a loaded 8-channel degenerate birdcage TxArray coil. $\mathbf{V}_q$ for $q = 1, 2, \ldots, 8$ represents the voltage across the port of the qth loop.

The decoupling strategy is based on the capacitive decoupling by adjusting the capacitors placed between the nearest neighbors. Particularly, c_d^q denotes decoupling capacitor, which is used to decouple the neighboring loops. Additionally, c_t^q denotes tuning capacitor, c_m^q denotes matching capacitor, and c_s^q denotes the series matching capacitor, which is used to improve the matching level with an additional degree of freedom.

To implement the numerical simulations, ANSYS Electronics Desktop 2019 R2 (ANSYS Inc., Canonsburg, PA, USA) is being used. A finite conductivity boundary [106] with the properties of copper was assigned for all coil and shield conductors. The co-simulation strategy [76] with combining the finite element method and circuit simulation analysis was used to adjust the capacitor values. The geometry of the simulated TxArray coil is circularly symmetric; therefore, to reduce the number of unknown parameters, it can be assumed that the values of the capacitors used in the same sections of different channels are equal. Consequently, four distinct capacitors, that is, $\bar{\mathbf{c}} = [c_d \quad c_t \quad c_m \quad c_s]$, with considering their equivalent series resistances, are considered as free design parameters to control the performance of the simulated TxArray coil.

In chapter 2, an approach based on the eigenmode analysis of **S**-matrix [50] was developed to effectively design TxArray coils in terms of power efficiency. Similarly, this method is used in this chapter to design the TxArray coil. In fact, the normalized reflected power for all excitation eigenmodes (eigenvalues of $\mathbf{S^H S}$, i.e., λ_n values) and the circularly polarized (CP) excitation mode (λ_{CP}) are minimized using the eigenmode analysis. The optimization problem has, therefore, been formulated as follows to find the optimum capacitor values (λ-opt):

$$\min_{\bar{\mathbf{c}}} \quad \frac{1}{8}\sum_{n=1}^{8} {\lambda_n}^2 + \lambda_{CP}^2 \tag{3.1}$$

Including λ_{CP} in the minimization problem enables the CP excitation mode to be composed of the most efficient excitation eigenmodes of the TxArray coil. The CP excitation mode is a critical mode of operation, which produces the most uniform $\mathbf{B}_1^+$ field [26] in the central plane of the TxArray coil. In this mode, all ports are individually excited with the same power and a phase shift of 45° between the successive ports.

3.3.2 Manufactured TxArray coil

Figure 3.2 demonstrates the 8-channel degenerate birdcage TxArray coil constructed with the same dimensions of the simulated coil (Figure 3.1A). Two cylindrical plexiglasses support the structure of the TxArray coil. The shield is broken down into eight uniformly spaced segments distributed along the axial direction. All segments of the coil and shield were copper strips with a thickness of 35 µm. Eight floating current traps [107] were constructed and added to the coil to prevent common-mode currents [108] at 123.2 MHz. The optimum capacitor values achieved from the simulation were used in the coil's prototype. The adjacent segments of the shield are connected with two 3 nF capacitors at locations facing the coil's end-rings. All used capacitors were non-magnetic surface mount high-Q capacitors. An SNR phantom (USA Instruments Inc., containing 3.7 g/L $NiCl_2.6H_2O$ and 2.4 g/L NaCl) with a cylindrical shape and a diameter of 153 mm was used to load the TxArray coil. Using magnetic resonance electrical properties tomography (MREPT) [78] technique, the conductivity of the phantom was measured as 0.62 S/m. The relative permittivity of the phantom was assumed to be the same as the relative permittivity of water [79, 80].

FIGURE 3.2 – The manufactured structure of a shielded 8-channel degenerate birdcage TxArray coil loaded with a cylindrical sodium-nickel solution phantom. The shield is broken down into eight uniformly spaced segments, where the adjacent segments are connected via two 2.5 nF capacitors at positions facing the coil's end-rings. Eight floating current traps were constructed and added to the coil.

As the TxArray coil was not machine-manufactured and, therefore, not quite the same as the simulated TxArray coil, it is expected that the simulated and measured **S-**

matrices would not be the same. The equivalent circuit model of the manufactured TxArray coil and the capacitors achieved from the simulation can be integrated to reduce the difference between the simulation and measurement results. This approach practically enables us to design the manufactured TxArray coil precisely. Figure 3.3 illustrates the equivalent circuit model of the manufactured TxArray coil, which is used to provide an efficient strategy to determine the suitable capacitors for the fabricated TxArray coil.

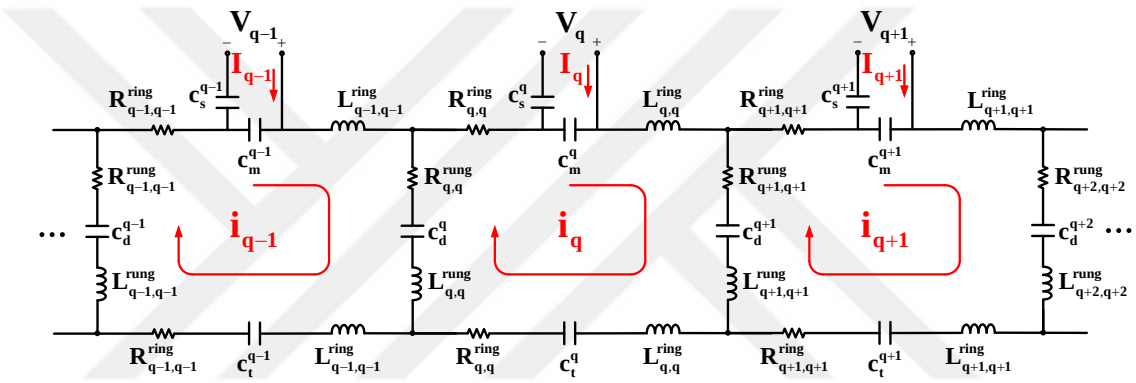

FIGURE 3.3 - Equivalent lumped element circuit model of the manufactured 8-channel degenerate birdcage TxArray coil. Although self/mutual-inductances (-resistances) are considered, only self-inductances (-resistances) are shown in the model.

The effects of all self/mutual-inductances and self/mutual-resistances emanating from the coil, the shield, and the load are taken into consideration. The current on an element of the coil can induce the eddy currents on the subject. These eddy currents can induce an electromotive force on other elements of the coil. This effect can be modeled as a mutual-resistance [109]. In Figure 3.3, $L_{q,q}^{ring}$ ($R_{q,q}^{ring}$) denotes the self-inductance (-resistance) of the qth arc at top/bottom end-ring, $L_{q,q}^{rung}$ ($R_{q,q}^{rung}$) denotes the self-inductance (-resistance) of the qth rung. Although it is not shown in Figure 3.3, the mutual-inductance (-resistance) between the qth and pth arcs in the same end-ring denotes as $L_{q,p}^{ring}$ ($R_{q,p}^{ring}$), the mutual-inductance (-resistance) between the qth and pth arcs in the different end-rings denotes as $\tilde{L}_{q,p}^{ring}$ ($\tilde{R}_{q,p}^{ring}$), and the mutual-inductance (-resistance) between the qth and pth rungs denotes as $L_{q,p}^{rung}$ ($R_{q,p}^{rung}$).

According to the image theory, the electromagnetic field produced by the currents induced on the surface of the RF shield is equal to the electromagnetic field produced by the image of the original currents running on the TxArray coil. Therefore, the RF

shield effect can be modeled with an imaginary TxArray coil with the same physical shape and radius of $r_i = r_s^2 / r_c$, where r_c and r_s are the coil and shield radii, respectively [110, 111]. The imaginary currents are in the opposite direction of the original currents to satisfy the boundary condition on the surface of the RF shield. Consequently, the shield's effects take into consideration by adding the mutual-inductance (-resistance) between the *q*th arc and the image of *p*th arc in the same end-ring that denotes as $L_{q,p}^{ring\prime}$ ($R_{q,p}^{ring\prime}$), the mutual-inductance (-resistance) between the *q*th arc and the image of *p*th arc in the different end-rings that denotes as $\tilde{L}_{q,p}^{ring\prime}$ ($\tilde{R}_{q,p}^{ring\prime}$), and the mutual-inductance (-resistance) between the *q*th rung and the image of *p*th rung that denotes as $L_{q,p}^{rung\prime}$ ($R_{q,p}^{rung\prime}$).

By analyzing the circuit model with Kirchhoff mesh current method, the following matrix equation can be derived as

$$\left(j\omega \mathbf{L}(\omega) + \frac{1}{j\omega}\mathbf{C} + \mathbf{R}(\omega) \right) \mathbf{i}(\omega) = \frac{1}{j\omega}\mathbf{C_m}\mathbf{I}(\omega) \tag{3.2}$$

where ω is the angular frequency and $j = \sqrt{-1}$. $\mathbf{i}(\omega) = \left[i_q(\omega) \right]_{8\times 1}$ denotes the vector of loop currents and $\mathbf{I}(\omega) = \left[I_q(\omega) \right]_{8\times 1}$ denotes the vector of current sources. $\mathbf{C} = \left[C_{q,p} \right]_{8\times 8}$ and $\mathbf{C_m} = \left[C_{q,p}^m \right]_{8\times 8}$ represent the capacitance matrices where $C_{q,p}$ and $C_{q,p}^m$ are defined as

$$C_{q,p} = \begin{cases} \dfrac{1}{c_d^{q-1}} + \dfrac{1}{c_d^q} + \dfrac{1}{c_t^q} + \dfrac{1}{c_m^q} & \text{if } q = p \\ -\dfrac{1}{c_d^{\min\{q,p\}}} & \text{if } q - p \equiv \pm 1 \text{ (mode 8)} \\ 0 & \text{otherwise} \end{cases} \tag{3.3}$$

$$C_{q,p}^m = \begin{cases} \dfrac{1}{c_m^q} & \text{if } q = p \\ 0 & \text{otherwise} \end{cases} \tag{3.4}$$

$\mathbf{L} = \left[L_{q,p} \right]_{8\times 8}$ and $\mathbf{R} = \left[R_{q,p} \right]_{8\times 8}$ also represent the inductance and resistance matrices, respectively, in which $L_{q,p}$ and $R_{q,p}$ are given by

$$\begin{aligned} L_{q,p} = {} & L_{q,p}^{rung} - L_{q,p}^{rung\prime} - L_{q+1,p}^{rung} + L_{q+1,p}^{rung\ \prime} - L_{q,p+1}^{rung} + L_{q,p+1}^{rung\ \prime} \\ & + L_{q+1,p+1}^{rung} - L_{q+1,p+1}^{rung\ \prime} + 2(L_{q,p}^{ring} - L_{q,p}^{ring\prime} - \tilde{L}_{q,p}^{ring} + \tilde{L}_{q,p}^{ring\prime}) \end{aligned} \tag{3.5}$$

$$\begin{aligned} R_{q,p} = {} & R_{q,p}^{rung} - R_{q,p}^{rung\prime} - R_{q+1,p}^{rung} + R_{q+1,p}^{rung\ \prime} - R_{q,p+1}^{rung} + R_{q,p+1}^{rung\ \prime} \\ & + R_{q+1,p+1}^{rung} - R_{q+1,p+1}^{rung\ \prime} + 2(R_{q,p}^{ring} - R_{q,p}^{ring\prime} - \tilde{R}_{q,p}^{ring} + \tilde{R}_{q,p}^{ring\prime}) \end{aligned} \tag{3.6}$$

In accordance with Kirchhoff mesh current method, the *q*th voltage source can be found as

$$V_q(\omega) = \frac{1}{j\omega}\left(\frac{1}{c_m^q} + \frac{2}{c_s^q}\right) I_q(\omega) - \frac{1}{j\omega c_m^q} i_q(\omega) \tag{3.7}$$

This equation can be written in the matrix form as

$$\mathbf{V}(\omega) = \frac{1}{j\omega}(\mathbf{C_m} + 2\mathbf{C_s})\mathbf{I}(\omega) - \frac{1}{j\omega}\mathbf{C_m}\mathbf{i}(\omega) \tag{3.8}$$

where $\mathbf{V}(\omega) = \left[V_q(\omega) \right]_{8\times 1}$ denotes the vector of voltage sources and $\mathbf{C_S} = \left[C_{q,p}^s \right]_{8\times 8}$, where its elements are given by

$$C_{q,p}^s = \begin{cases} \dfrac{1}{c_s^q} & \text{if } q = p \\ 0 & \text{otherwise} \end{cases} \tag{3.9}$$

Substituting the vector of loop input currents, obtained from Equation (3.2), into Equation (3.8) gives

$$\mathbf{V}(\omega) = \left(\frac{1}{j\omega}(\mathbf{C_m} + 2\mathbf{C_s}) + \frac{1}{\omega^2}\mathbf{C_m}\left(j\omega\mathbf{L}(\omega) + \frac{1}{j\omega}\mathbf{C} + \mathbf{R}(\omega) \right)^{-1} \mathbf{C_m} \right) \mathbf{I}(\omega) \tag{3.10}$$

Therefore, the impedance matrix (**Z**-matrix) of the manufactured TxArray coil's model can be expressed as follows:

$$\mathbf{Z}(\omega)=\frac{1}{j\omega}(\mathbf{C_m}+2\mathbf{C_s})+\frac{1}{\omega^2}\mathbf{C_m}\left(j\omega\mathbf{L}(\omega)+\frac{1}{j\omega}\mathbf{C}+\mathbf{R}(\omega)\right)^{-1}\mathbf{C_m} \tag{3.11}$$

The **S**-matrix in terms of the impedance matrix can be written as

$$\mathbf{S}(\omega)=(\mathbf{Z}(\omega)+Z_0\mathbf{U})^{-1}(\mathbf{Z}(\omega)-Z_0\mathbf{U}) \tag{3.12}$$

where Z_0 is characteristic impedance and **U** returns an 8×8 identity matrix. In the construction of the manufactured TxArray coil, the optimized capacitor values achieved from the simulation environment initially can be used. By measuring the **Z**-matrix of the manufactured TxArray over a wide range of frequencies for these initial capacitor values, the inductance and resistance matrices can be calculated as

$$\mathbf{R}(\omega)=\frac{1}{\omega^2}\mathrm{Re}\left\{\mathbf{C_m}\left(\mathbf{Z}(\omega)-\frac{1}{j\omega}(\mathbf{C_m}+2\mathbf{C_s})\right)^{-1}\mathbf{C_m}\right\} \tag{3.13}$$

$$\mathbf{L}(\omega)=\frac{1}{\omega^3}\mathrm{Im}\left\{\mathbf{C_m}\left(\mathbf{Z}(\omega)-\frac{1}{j\omega}(\mathbf{C_m}+2\mathbf{C_s})\right)^{-1}\mathbf{C_m}\right\}+\frac{1}{\omega^2}\mathbf{C} \tag{3.14}$$

Once the inductance and resistance matrices are determined, a new set of capacitor values can be accomplished to minimize the cost function implemented in Equation (3.1) for the manufactured TxArray coil. The new **Z**-matrix (or **S**-matrix), which fulfills the design criteria, can be measured by updating capacitor values used in the manufactured TxArray coil.

3.4 Results

Initially, the structure of the manufactured TxArray coil was assumed to be the same as that of the simulated TxArray coil, which resulted in the use of nearly identical capacitors in both structures. The optimized capacitor values obtained based on the λ-opt approach for the simulated coil were 12.8 pF, 9.5 pF, 34.7 pF, and 10.5 pF for c_d, c_t, c_m, and c_s, respectively. Therefore, in the first attempt, the same capacitor values were used in the manufactured TxArray coil, but with a tolerance of less than 2%. Figure 3.4 illustrates the reflection coefficients and the average of modal reflected power values, λ_{av}, for both simulated and manufactured 8-channel TxArray coils as a

function of frequency. The results showed that all transmit channels of the simulated TxArray coil resonate at 123.2 MHz with a reflection coefficient of less than -26 dB, which shows that they are very well matched and tuned. Unlike the simulation, the transmit channels of the manufactured TxArray coil resonate at different frequencies (ranging from 130.4 MHz to 131.8 MHz) with different matching levels (ranging from -9 dB to -31 dB). On average, the resonances of the manufactured TxArray coil are 7.7 MHz higher than the desired resonance frequency. Figure 3.4B shows that the lowest value of λ_{av} for the simulated TxArray coil is 0.23, which is attained at 123.2 MHz. On the other hand, for the manufactured TxArray coil, the lowest value of λ_{av} is 0.47, at 130.9 MHz. Since λ_{av} is also equal to $\frac{1}{8}\sum_{n=1}^{8}\sum_{m=1}^{8}|s_{mn}|^2$, it can be inferred that in addition to the difference in the resonance frequencies and reflection coefficients of the simulated and manufactured TxArray coils, other scattering parameters are also different.

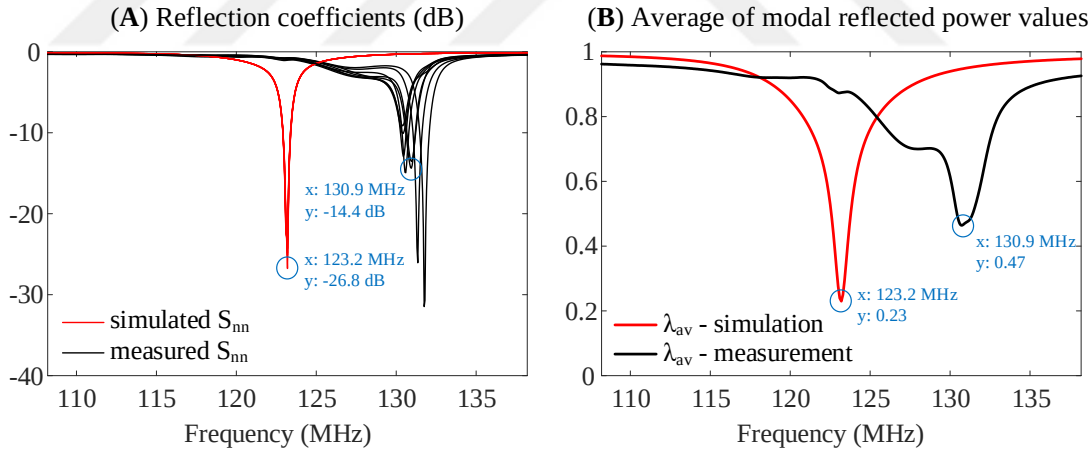

FIGURE 3.4 - Simulated and measured (A) reflection coefficients and (B) the average of modal reflected power values, λ_{av}, of the 8-channel TxArray coil with nearly the same capacitor values as a function of frequency.

Figure 3.5A-B presents the simulated **S**-matrix at 123.2 MHz and the measured **S**-matrix at 130.9 MHz of the 8-channel TxArray coil, respectively. An error matrix is defined as the difference between the simulated and measured **S**-matrix at their resonance frequencies and calculated as $|\mathbf{S}_{simulated}(f=123.2\,\text{MHz}) - \mathbf{S}_{measured}(f=130.9\,\text{MHz})|$ is also illustrated under Figure 3.5C. The maximum difference in the matching and coupling levels are -2.8 dB and -4.8 dB, respectively.

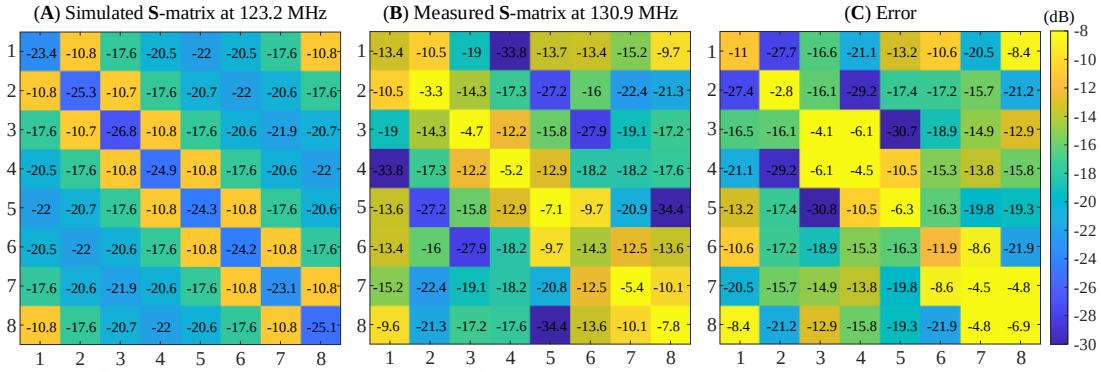

FIGURE 3.5 – (A) Simulated **S**-matrix at 123.2 MHz and (B) measured **S**-matrix at 130.9 MHz of the 8-channel TxArray coil. (C) Difference between the simulated **S**-matrix at 123.2 MHz and measured **S**-matrix at 130.9 MHz.

As expected, the measurement results are significantly different than simulation results when the same capacitors were used in both manufactured and simulated TxArray coil. This difference can be explained by the imperfections of the coil's construction, which indicates that the manufactured and simulated structures are not quite identical. By applying the proposed approach to the manufactured TxArray coil and measuring its inductance and resistance matrices, new quantities of the capacitor values were determined. The optimized capacitor values obtained based on the λ-opt

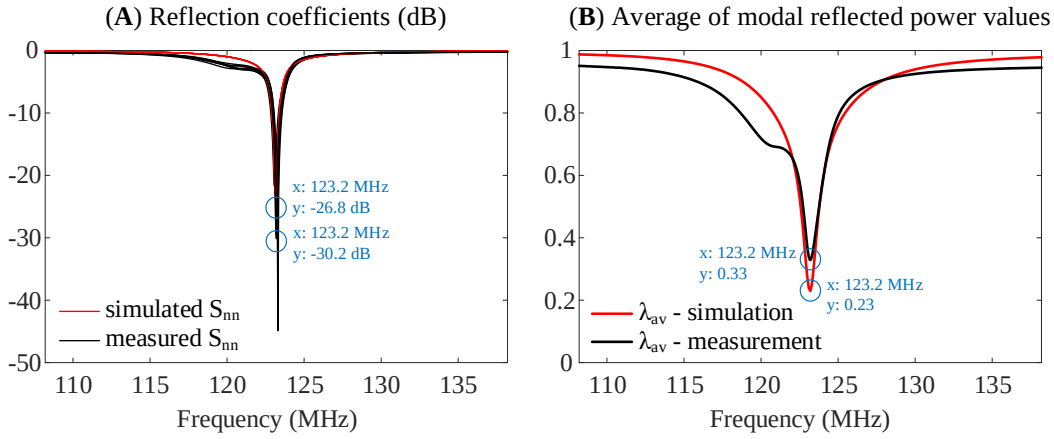

FIGURE 3.6 - Simulated and measured (A) reflection coefficients and (B) the average of modal reflected power values, λ_{av}, of the 8-channel TxArray coil as a function of frequency. Simulation results were obtained with the initial capacitor values (c_d = 12.8 pF, c_t = 9.5 pF, c_m = 34.7 pF, and c_s = 10.5 pF), while the measurement results were achieved with the new capacitor values (c_d = 14.5±0.1 pF, c_t = 10.6±0.7 pF, c_m = 40.4±0.2 pF, and c_s = 12.9±0.1 pF).

approach for the manufactured coil were 14.5±0.1 pF, 10.6±0.7 pF, 40.4±0.2 pF, and 12.9±0.1 pF for c_d, c_t, c_m, and c_s, respectively. Figure 3.6 illustrates the reflection coefficients and λ_{av} for the manufactured 8-channel TxArray coil with the new set of capacitors as a function of frequency. For comparison, this figure also shows the reflection coefficients and λ_{av} for the simulated 8-channel TxArray coil. As shown in Figure 3.6A, all transmit channels of the manufactured TxArray coil resonate at the desired resonance frequency with an acceptable level of matching (≤ -15 dB). Figure 3.6B also demonstrates that the lowest value of λ_{av} for the manufactured TxArray coil is 0.33, which is attained at 123.2 MHz. This value is 0.1 greater than the same value in the simulation, but for the manufactured TxArray coil, it is still the lowest available value of λ_{av}.

Figure 3.7 displays the simulated and measured (1st iteration) all eight λ_n values plus λ_{CP} at 123.2 MHz. For both simulated and manufactured TxArray coils, only one excitation eigenmode, i.e., the eigenvector of $\mathbf{S^H S}$, has an extremely high modal reflected power (> 0.92). This mode, therefore, hardly contributes to the process of transmission. For the simulated TxArray coil, seven excitation eigenmodes have a total

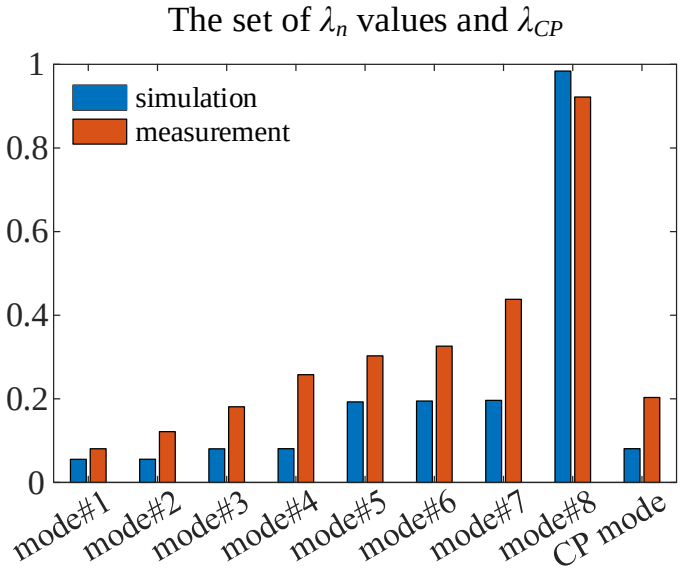

FIGURE 3.7 - Simulated and measured modal reflected power values of the 8-channel TxArray coil at 123.2 MHz. For comparison, λ_{CP} is also shown. Simulated λ values were obtained with the initial capacitor values (c_d = 12.8 pF, c_t = 9.5 pF, c_m = 34.7 pF, and c_s = 10.5 pF), while the measured λ values were achieved with the new capacitor values (c_d = 14.5±0.1 pF, c_t = 10.6±0.7 pF, c_m = 40.4±0.2 pF, and c_s = 12.9±0.1 pF).

reflection of less than 20%. The manufactured TxArray coil, on the other hand, has seven excitation eigenmodes with a maximum total reflection of less than 44%. The normalized reflected power in the CP excitation mode for the simulated and manufactured TxArray coils are 0.08 and 0.2, respectively. In the manufactured TxArray coil (1st iteration) design process, it has been possible to minimize λ_{CP} more, although this has increased λ_{av}.

The simulated and measured (1st iteration) **S**-matrices of the 8-channel TxArray coil at 123.2 MHz are presented in Figure 3.8A-B. For the simulated and manufactured TxArray coils, the maximum coupling is -10.7 dB and -8.9 dB, respectively, which is occurred between the adjacent channels. For non-neighboring channels, the maximum coupling is -17.6 dB and -13.5 dB for the simulated and manufactured TxArray coils, respectively. Furthermore, an error matrix is defined as the difference between the simulated and measured **S**-matrix at the desired frequency and calculated as $|\mathbf{S}_{simulated}(f = 123.2\,\text{MHz}) - \mathbf{S}_{measured}(f = 123.2\,\text{MHz})|$ is also illustrated under Figure 3.8C. The maximum differences in the matching and coupling levels are -13.3 dB and -6.8 dB, respectively, which are lower than the error presented in Figure 3.5C. Note that in the first iteration, only the cost function written in Equation (3.1) at 123.2 MHz was minimized, and no attempt was made to reduce the difference between the simulated and measured **S**-matrices.

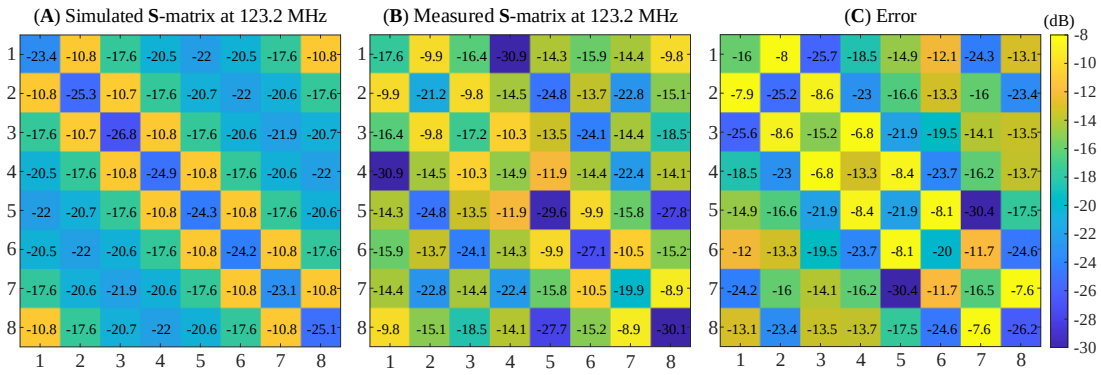

FIGURE 3.8 – (A) Simulated and (B) measured **S**-matrices of the 8-channel TxArray coil at 123.2 MHz. (C) Difference between the simulated and measured **S**-matrices at 123.2 MHz. Simulated **S**-matrix was obtained with the initial capacitor values (c_d = 12.8 pF, c_t = 9.5 pF, c_m = 34.7 pF, and c_s = 10.5 pF), while the measured **S**-matrix was achieved with the new set of the capacitor values (c_d = 14.5±0.1 pF, c_t = 10.6±0.7 pF, c_m = 40.4±0.2 pF, and c_s = 12.9±0.1 pF).

3.5 Discussion and conclusion

Considering the exact manufactured structure of TxArray coils in the design process may reduce the error between the experimental and simulation results caused by the coil's manufacturing imperfection. This chapter developed a practical approach based on modeling of manufactured TxArray coils using distributed lumped-elements. In this approach, the coil's structure can first be simulated in a commercial EM solver to determine the most optimal values for the coil's free parameters in the simulation environment. By assembling the optimum lumped elements and measuring the impedance (scattering) matrix of the fabricated coil in a wide frequency range, and analyzing its equivalent circuit model, it is possible to predict unknown parameters of the circuit model as a function of frequency, including the coil's inductances and resistances. Whenever the equivalent inductances and resistances are determined, the free design parameters can be optimized again to properly design the fabricated TxArray coil.

In developing diagnostic magnetic resonance imaging, the conventional birdcage resonator has played an important role. For whole-body imaging at 1.5T and a wide range of other static field strength ($\mathbf{B}_0$), birdcage coil has been recognized as an efficient and highly homogeneous RF resonator [112]. However, increasing the strength of the static field decreases the electromagnetic wavelength inside of the body, which has a high dielectric constant, and causes a destructive interference on the magnetic field, resulting in an inhomogeneous $\mathbf{B}_1^+$ field [113, 114]. TxArray coils with multichannel excitations can be used to achieve a more uniform $\mathbf{B}_1^+$ field within the sample. However, TxArray coils have been investigated in many types, and each has its advantages and drawbacks. They can be categorized as follows: Loop-based designs with various kinds of inter-element decoupling components [60, 115], microstrip-based designs with [116, 117] or without [5, 6, 36] inter-element decoupling components, dipole-based designs [118, 119], and multiple combinations of these designs [120]. The selection of the suitable TxArray coil design must take account of both theoretical and practical factors imposed by the application goal. The birdcage-like TxArray coils are intrinsically more efficient among loop-based models because of the shared conductors between the neighboring meshes [62, 63]. In the loop-based non-birdcage TxArray coils, the currents flow in both directions of the two adjacent loop conductors. In contrast, these currents are combined in the birdcage-like

TxArray coils, leading to a reduced current along the shared path formed by the rungs of birdcage-like TxArray coils and hence increased efficiency of the coil.

In this chapter, the performance of a shielded 8-channel head TxArray coil at 123.2 MHz together with simulation and experiment, was investigated to validate the proposed method. The framework chosen of the coil has a considerable potential to substitute conventional body coils. The coil performance, if it is driven in the circularly polarized (CP) mode, is comparable to the traditional birdcage coils. Still, the coil can also provide extra flexibility for a wide range of useful TxArray coils applications. In this scheme, the degenerate birdcage TxArray coil was opted to assess. It is a particular case of birdcage-like TxArray coils where the capacitor values are adjusted to collapse all resonating modes to a single (degenerate) frequency [62, 63, 74].

The proposed coil in this chapter was appropriately simulated and designed using the co-simulation strategy [76]. Then it was manufactured by assembling the optimum lumped-elements obtained from the simulation. The results revealed that the measured and simulated **S**-matrices are not matched with each other. Fine-tuning and matching by changing the capacitor values had traditionally been a way forward for us to reduce this mismatch. Through this process, iterative tuning and matching of all transmit channels are needed. If only one channel is designed individually, 4 embedded capacitors control its performance. In this situation, the coupling is not an issue, and fine-tuning and matching can reduce the mismatch in a reasonable time. When all channels are designed simultaneously, the embedded capacitors in one channel will affect the performance of other channels; therefore, all 32 capacitor values need to be changed to reduce the mismatch between the simulation and experiment. Iteratively changing the capacitor values one by one in successive steps can tune all transmit channels to the desired frequency and improve their matching levels. However, these changes will affect the decoupling levels. At the same time, controlling the performance of 8 channels by 32 capacitor values is very tedious and time-consuming. Even if all of them can be designed with an acceptable level of tuning, matching, and decoupling by following the mentioned approach, there is no guarantee that the optimum design is achieved. Since fine-tuning and matching are based on trial and error, there is still a chance to improve the manufactured coil's performance more. However, it was demonstrated that coil modeling could predict the optimum capacitor values and design the manufactured coil properly only by one iteration.

As the co-simulation strategy was used to find the optimum capacitor values only by one iteration in the simulation, this method may also be used in the design process of manufactured coils. In this case, the multi-port **S**-matrix of loaded TxArray coils must be measured by considering all lumped-elements as lumped-ports. Hence, in addition to the excitation ports, all lumped-elements must be replaced with coaxial cables equipped with cable traps. However, these extra cablings in the vicinity of the transmit loops can significantly affect the coils electromagnetic fields and, as a result, add some errors to the measured multi-port **S**-matrix. Furthermore, the extra coaxial cables will add some phases to the measured multi-port **S**-matrix. These additional phases must be measured correctly and deducted from the multi-port **S**-matrix later in the post-processing. Also, this approach requires numerous measurements to obtain the multi-port **S**-matrices elements one by one. For example, for the 8-channel TxArray coil presented in this chapter, the multi-port **S**-matrix calculation, which is a 40×40 matrix, requires 820 individual measurements by a two-port network analyzer. As the number of transmitting and lumped elements increases, these problems will be more considerable and makes this method inefficient.

In this chapter, the TxArray coil design method based on the eigenmode analysis of **S**-matrix [50] was used to find the optimal capacitor values in the simulation and manufacturing. The eigenmode analysis of **S**-matrix is an efficient way that can quantitatively represent the power transfer capabilities of TxArray coils. The insight provided by the eigenmode analysis can categorize the excitation modes of a pre-designed TxArray coil according to their level of power reflections. Earlier, it was shown that the normalized reflected power for a particular excitation mode could be calculated as the weighted sum of the $\mathbf{S^H S}$-matrix's eigenvalues, where the superscript **H** represents the Hermitian transpose. Hence, $\mathbf{S^H S}$-matrix's eigenvalues need to be minimized to expand the excitation space with a low power reflection. Based on all these facts, the eigenmode analysis offers a simple tool for evaluating, comparing, and optimizing the transmission performance of different TxArray coils. In this practice, the optimum capacitor values have been found to minimize all eigenvalues of $\mathbf{S^H S}$-matrix. The capacitors were also adjusted to mitigate the normalized reflected power in the CP excitation, as a critical operation mode of the TxArray coil studied in this chapter.

Chapter 4

Optimized Transmit Array Coil for Minimum Coupling: A Simulation Study on a Degenerate Birdcage Transmit Array Coil

4.1 Preface

The content of this chapter has been partially presented at the International Society of Magnetic Resonance in Medicine (ISMRM)'s 27th Annual Scientific Meeting [104]. Ergin Atalar was involved in conceptualizing the content of this chapter and in its methodology.

4.2 Introduction

Multichannel radiofrequency (RF) transmit array (TxArray) coils can be used to increase image quality, accelerate imaging, and reduce RF safety risks in critical MRI applications. Coupling between individual transmit elements can have a negative impact on the performance of TxArray coils. Magnetic and electric interactions between the individual channels cause extra losses leading to an increase in the power consumption by TxArray coils. Hence the coupling is a major issue in the design process of the TxArray coils. Numerous approaches are employed to reduce the effective coil coupling, including the use of L/C decoupling networks [27-30], overlapping of neighboring array elements [31, 32], transformer decoupling [33],

inserting the induced current elimination (ICE) decoupling elements [34, 35], and adding reactive decoupling circuits among adjacent array elements [36].

In these methods, the physical dimensions of TxArray coils were not considered to be a degree of freedom to reduce the coupling effects. However, the coupling can be categorized as magnetic (mutual-inductance) and electric (mutual-resistance) couplings. For a specific frequency, the magnetic coupling mostly depends on the coil characteristics, and the electrical coupling depends on both the coil and load characteristics. Subsequently, finding the optimal physical sizes in terms of the minimum magnetic coupling can improve decoupling.

In this chapter, a theoretical TxArray coil design strategy is introduced to minimize the magnetic coupling between non-adjacent transmit elements by optimizing the coil's physical sizes. The method is based on the calculation of all self/mutual-inductances and then the minimization of the mutual-inductances normalized by the self-inductances. This method is used to find the optimal sizes of a shielded 12-channel degenerate birdcage head 3T TxArray coil. The optimization is performed to find the optimal coil radius and length, and the width of end-rings and rungs. Finite element electromagnetic simulations are used to confirm the optimal sizes predicted using the proposed method.

4.3 Theory and methods

Figure 4.1 demonstrates the electromagnetic (EM) model and schematic of an unloaded circular symmetric 12-channel degenerate birdcage TxArray coil enclosed by a cylindrical shield. The TxArray coil has a cylindrical shape and comprises of twelve transmit channels of the same dimensions.

For this type of TxArray coils, the neighboring transmit elements are decoupled by adjusting capacitors placed on their mutual rungs. In Figure 4.1B, the capacitor used to decouple the (*q-1)*th and the *q*th channels is denoted as c_d^q, the tuning capacitor in the *q*th channel is denoted as c_t^q, and the matching capacitor in the *q*th channel is represented as c_m^q. Since the coil's geometry is circularly symmetric, the values of the capacitors used in the same sections of various channels are assumed to be equal to decrease the number of unknown parameters. Therefore, in addition to the coil's

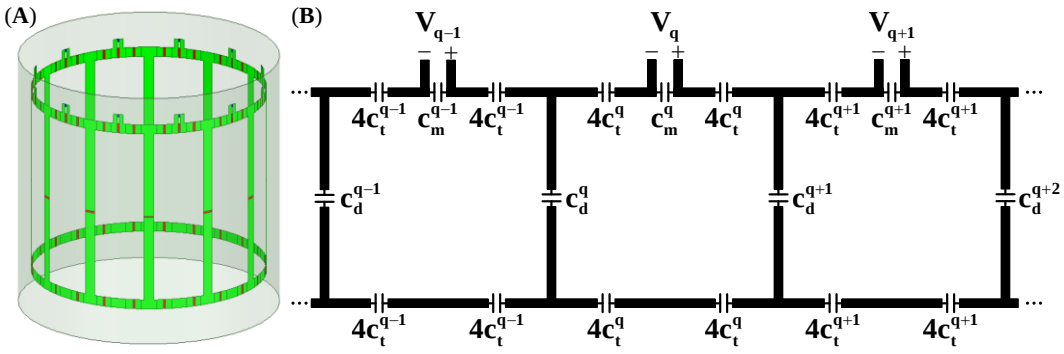

FIGURE 4.1 – (A) Electromagnetics (EM) simulation model and (B) schematic of an unloaded 12-channel degenerate birdcage TxArray coil. $\mathbf{V}_q$ for *q = 1, 2, ..., 12* refers to the input voltage across the *q*th port.

physical parameters, a total of three distinct capacitors, i.e. $\overline{\mathbf{c}} = [c_d \quad c_t \quad c_m]$, are considered as free design parameters to control the performance of the TxArray coil.

4.3.1 Circuit model analysis

Figure 4.2 demonstrates the equivalent circuit model of the TxArray coil shown in Figure 4.1A. In this model, the effects of all self/mutual-inductances originating from the coil and its shield are considered, but only the self-inductances are shown. The coil is not loaded, and both coil and shield are considered to be made from perfect electric conductors. It also is supposed the loss of radiation is negligible; therefore, the circuit model does not include any resistance.

In Figure 4.2, $L_{q,q}^{ring}$ indicates the *q*th arc's self-inductance at the top/bottom end-ring and $L_{q,q}^{rung}$ indicates the *q*th rung's self-inductance. Although it is not indicated in Figure 4.2, the mutual-inductance between the *q*th and *p*th arcs in the same end-ring is referred as $L_{q,p}^{ring}$, the mutual-inductance between the *q*th and *p*th arcs in the different end-rings is referred as $\tilde{L}_{q,p}^{ring}$, and the mutual-inductance between the *q*th and *p*th rungs is referred as $L_{q,p}^{rung}$. Assuming that the shield's length is long enough, the image theory notes that the electromagnetic field generated by the currents induced on the shield's surface is equal to that generated by the image of the original currents running on the TxArray coil. Hence, the shield can be replaced by an imaginary TxArray coil with the same physical shape. The direction of the currents on this imaginary coil should be in the opposite direction of the original currents to fulfill the boundary condition on

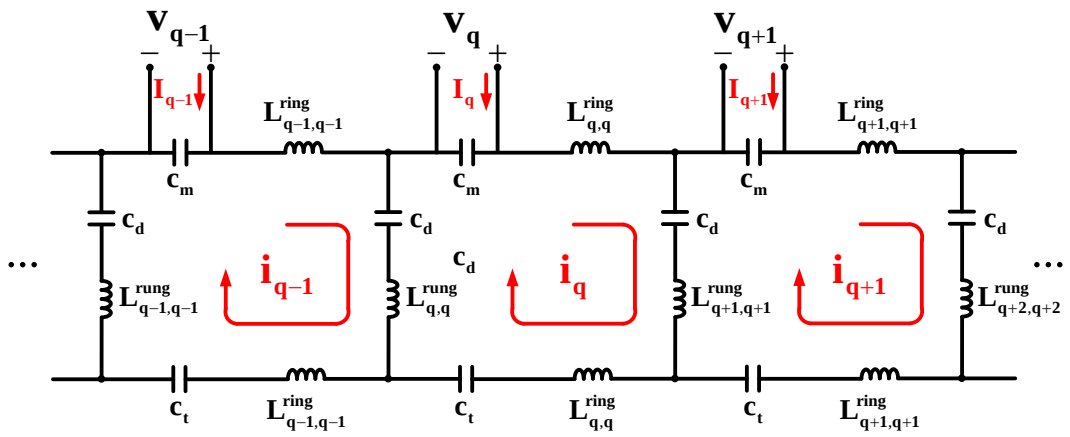

FIGURE 4.2 - Equivalent circuit model of an unloaded 12-channel degenerate birdcage TxArray coil. Although both self- and mutual-inductances of the coil are considered in the equivalent circuit model, only the self-inductors are shown in the model.

the shield's surface. The effects of the shield are then taken into account by adding the mutual-inductance between the *q*th arc and the image of *p*th arc in the same end-ring, which is referred as $L_{q,p}^{ring\prime}$, the mutual-inductance between the *q*th arc and the image of *p*th arc in the different end-rings, which is referred as $\tilde{L}_{q,p}^{ring\prime}$, and the mutual-inductance between the *q*th rung and the image of *p*th rung, which is referred as $L_{q,p}^{rung\prime}$.

By applying the mesh current method to the circuit model and using Kirchhoff's voltage law at the desired frequency, the mesh equations can be derived as the following matrix equation

$$\underbrace{\left(j\omega_0\mathbf{L}+\frac{1}{j\omega_0}\mathbf{C}\right)}_{\mathbf{A}}\mathbf{i}=\frac{1}{j\omega_0 c_m}\mathbf{I} \tag{4.1}$$

where ω_0 is the angular frequency associated with Larmor frequency. $\mathbf{i}=\left[i_q\right]_{12\times1}$ represents the vector of loop currents and $\mathbf{I}=\left[I_q\right]_{12\times1}$ represents the vector of input currents. $\mathbf{C}=\left[C_{q,p}\right]_{12\times12}$ indicates the capacitance matrix, where $C_{q,p}$ is given by

$$C_{q,p} = \begin{cases} \dfrac{2}{c_d} + \dfrac{1}{c_t} + \dfrac{1}{c_m} & \text{if } q = p \\ -\dfrac{1}{c_d} & \text{if } q - p \equiv \pm 1 \text{ (mode 12)} \\ 0 & \text{otherwise} \end{cases} \tag{4.2}$$

$\mathbf{L} = \left[L_{q,p} \right]_{8\times 8}$ indicates the inductance matrix, where $L_{q,p}$ is defined as

$$\begin{aligned} L_{q,p} = {} & L_{q,p}^{rung} - L_{q,p}^{rung\prime} - L_{q+1,p}^{rung} + L_{q+1,p}^{rung\ \prime} - L_{q,p+1}^{rung} + L_{q,p+1}^{rung\ \prime} \\ & + L_{q+1,p+1}^{rung} - L_{q+1,p+1}^{rung\ \prime} + 2(L_{q,p}^{ring} - L_{q,p}^{ring\prime} - \tilde{L}_{q,p}^{ring} + \tilde{L}_{q,p}^{ring\prime}) \end{aligned} \tag{4.3}$$

Given that the coil's geometry is circularly symmetric, both **L** and **C** matrices are symmetric circulant matrices [121]. They can fully be characterized by seven elements, which appears as the first seven elements of the first row (column) of their matrices. As a result, $\mathbf{A} = j\omega_0(\mathbf{L} - \frac{1}{\omega_0^{\ 2}}\mathbf{C})$ is also a symmetric circulant matrix and can be determined by the first seven elements of its first row (column) as follows

$$\begin{aligned} A_{1,1} &= j\omega_0(L_{1,1} - \frac{1}{\omega_0^{\ 2}}(\frac{2}{c_d} + \frac{1}{c_t} + \frac{1}{c_m})) \\ A_{1,2} &= j\omega_0(L_{1,2} + \frac{1}{\omega_0^{\ 2}}\frac{1}{c_d}) \\ A_{1,3} &= j\omega_0 L_{1,3} \\ A_{1,4} &= j\omega_0 L_{1,4} \\ A_{1,5} &= j\omega_0 L_{1,5} \\ A_{1,6} &= j\omega_0 L_{1,6} \\ A_{1,7} &= j\omega_0 L_{1,7} \end{aligned} \tag{4.4}$$

Consider a situation where all non-diagonal elements of **A**-matrix are nulled, then

$$\mathbf{A} = \left[A_{q,p} \right]_{12\times 12} = A_{1,1}\mathbf{U} \tag{4.5}$$

where **U** refers to a *12×12* identity matrix. By substituting Equation (4.5) into Equation (4.1), the vector of loop currents can be written as

$$\mathbf{i} = \frac{1}{j\omega_0 c_m A_{1,1}}\mathbf{I} \tag{4.6}$$

Equation (4.6) illustrates that the current of the *n*th loop depends only on the *n*th input current, i.e., $i_n = \frac{1}{j\omega_0 c_m A_{1,1}} I_n$, which shows that the coupling is zero in this situation. To meet this condition and force the coil to resonate, $L_{1,1}$ needs to be $\frac{1}{\omega_0^{\,2}}(\frac{2}{c_d}+\frac{1}{c_t}+\frac{1}{c_m})$, $L_{1,2}$ needs to be $-\frac{1}{c_d\omega_0^{\,2}}$, and $L_{1,3}$, $L_{1,4}$, …, $L_{1,7}$ all need to be zero. By adjusting the capacitors, only $L_{1,1}$ and $L_{1,2}$ can meet the requirements, and zeroing other inductances is not feasible. This means that considering only the capacitors as the free design parameters can enable us to tune and match each transmit channel individually and also allow us only to cancel the coupling between the adjacent channels. Although it is not possible to null all $L_{1,3}$, $L_{1,4}$, …, $L_{1,7}$, the coil's physical parameters can be optimized to minimize them. In this chapter, a design strategy based on minimizing the mutual-inductances between non-adjacent transmit elements, or in other words, minimizing the magnetic coupling between non-adjacent channels, was employed to determine the optimum coil's physical parameters. Therefore, the optimization problem was formulated as follows

$$\min \quad \left\| \frac{1}{L_{1,1}} \begin{bmatrix} L_{1,3} & L_{1,4} & \cdots & L_{1,11} \end{bmatrix} \right\|_2 \tag{4.7}$$

or

$$\min \quad \sqrt{\frac{2L_{1,3}^{\,2} + 2L_{1,4}^{\,2} + 2L_{1,5}^{\,2} + 2L_{1,6}^{\,2} + L_{1,7}^{\,2}}{L_{1,1}^{\,2}}} \tag{4.8}$$

In equations (4.7) and (4.8), the mutual-inductances normalized with respect to the self-inductance value were minimized.

4.3.2 Self/mutual-inductances calculation

The self/mutual-inductance values can be estimated theoretically using Neumann formula [122], and for low fields (≤ 3T), they are independent of the surface current

values and depend only on the coil's geometry. The mutual-inductance between two conductors v_m and v_n fed with current densities J_m and J_n is evaluated by means of the following expression

$$L_{m,n} = \frac{\mu_0}{4\pi I_m I_n} \int_{v_m} \int_{v_n} \frac{\vec{J}_m(\vec{r}).\vec{J}_n(\vec{r}')}{|\vec{r} - \vec{r}'|} dv dv' \tag{4.9}$$

where μ_0 represents the vacuum permeability, and I_m represents the total current in the conductor v_m. To calculate inductances of an unloaded 12-channel degenerate birdcage TxArray coil, as it is shown in Figure 4.3A, the shield initially needs to be replaced by an imaginary TxArray coil (Figure 4.3B) with a radius of $r_i = r_s^2 / r_c$, where r_c and r_s denote the coil and shield radii, respectively [110, 111]. Then all conductors should be segmentized, as can be seen in Figure 4.3C. In this figure, the coil length is indicated as l_c, the width of the circular conductive end rings is indicated as w_{ring}, the width of the parallel straight conductors of the coil, rungs, is indicated as w_{rung}. In Figure 4.3C, the strips used for feeding were ignored. Also, the capacitor's gaps are replaced by the conductor to reduce the complexity of the problem.

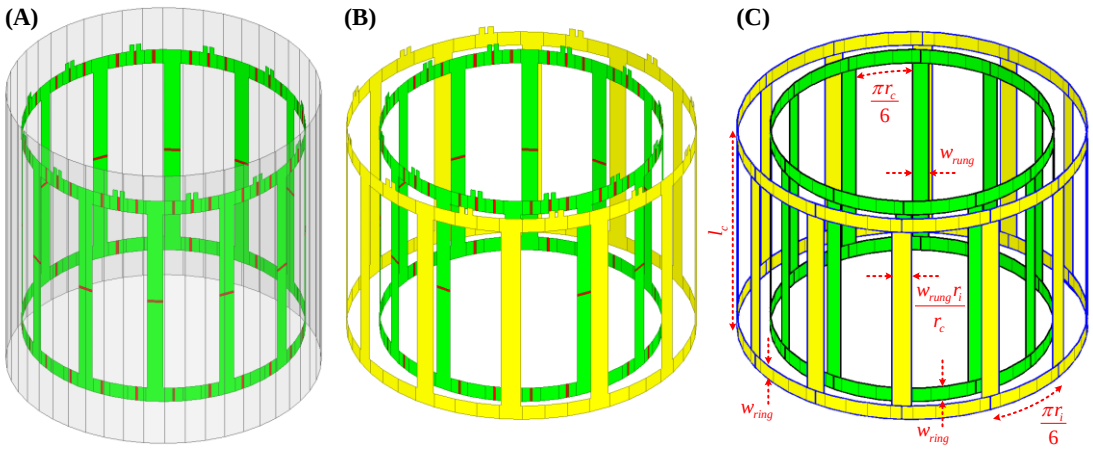

FIGURE 4.3 - (A) EM simulation model of an unloaded 12-channel degenerate birdcage TxArray coil enclosed by a cylindrical shield. (B) The original and imaginary TxArray coils. The cylindrical shield is replaced with an imaginary coil. (C) The original and imaginary segmentized TxArray coils.

In this chapter, the strip thickness is assumed to be negligible, and the current is uniformly distributed across all conductors. Therefore, the current on the qth segment of the original coil's top/bottom end-ring is $\vec{J}_q = I_q \hat{a}_\varphi / w_{ring}$, and the current on the

original coil's qth rung is $\vec{J}_q = I_q \hat{a}_z / w_{rung}$. Besides, the current on the qth segment of the imaginary coil's top/bottom end-ring is $\vec{J}_q = I_q \hat{a}_\varphi / w_{ring}$, and the current on the imaginary coil's qth rung is $\vec{J}_q = I_q \hat{a}_z r_c / w_{rung}\, r_i$. Hence, the mutual-inductances between the end-ring segments and rung segments are zero because their currents are perpendicular to each other. In general, self/mutual-inductance calculation for the TxArray coil can be divided into two simpler subproblems, as shown in Figure 4.4.

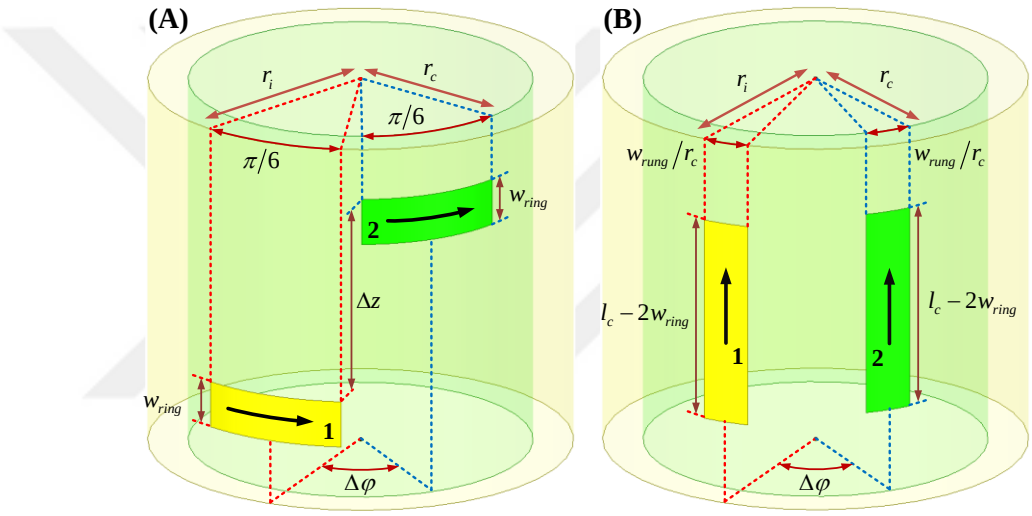

FIGURE 4.4 - (A) Two parallel rung conductors with uniformly currents distributed along the φ-axis and (B) two parallel end-ring conductors with uniformly currents distributed along the z-axis.

Then the mutual-inductance for the inductors shown in Figure 4.4A can be reduced to

$$L_{1,2}^{ring} = \frac{\mu_0 r_c r_i}{4\pi w_{ring}^{\ 2}} \times \int_0^{w_{ring}} \int_0^{\pi/6} \int_{\Delta z}^{\Delta z + w_{ring}} \int_{\Delta\varphi}^{\Delta\varphi + \pi/6} \frac{\cos(\varphi_1 - \varphi_2)}{\sqrt{r_c^{\ 2} + r_i^{\ 2} - 2 r_c r_i \cos(\varphi_2 - \varphi_1) + (z_1 - z_2)^2}} d\varphi_2 dz_2 d\varphi_1 dz_1 \tag{4.10}$$

Similarly, the mutual-inductance for the inductors shown in Figure 4.4B can be written as

$$L_{1,2}^{rung} = \frac{\mu_0 r_c r_i}{4\pi w_{rung}^{\ 2}} \times \int_0^{l_c-2w_{ring}} \int_0^{w_{rung}/r_c} \int_0^{l_c-2w_{ring}} \int_{\Delta\varphi}^{\Delta\varphi+w_{rung}/r_c} \frac{1}{\sqrt{r_c^{\ 2}+r_i^{\ 2}-2r_c r_i\cos(\varphi_2-\varphi_1)+(z_1-z_2)^2}}\, d\varphi_2 dz_2 d\varphi_1 dz_1 \tag{4.11}$$

To simplified Equations (4.10) and (4.11) to a double integral, the integration variables are replaced as follows

$$\begin{aligned} z_1 - z_2 &= z \\ z_1 + z_2 &= z' \end{aligned} \quad \text{and} \quad \begin{aligned} \varphi_1 - \varphi_2 &= \varphi \\ \varphi_1 + \varphi_2 &= \varphi' \end{aligned} \tag{4.12}$$

Then Equations (4.10) and (4.11) can be reduced to

$$\begin{aligned} L_{1,2}^{ring} = \frac{\mu_0 r_c r_i}{4\pi w_{ring}^{\ 2}} \Bigg(& \int_{-\Delta z-w_{ring}}^{-\Delta z} \int_{-\Delta\varphi-\pi/6}^{-\Delta\varphi} \frac{(\varphi+\Delta\varphi+\pi/6)(z+\Delta z+w_{ring})\cos(\varphi)}{\sqrt{r_c^{\ 2}+r_i^{\ 2}-2r_c r_i\cos(\varphi)+z^2}}\, d\varphi dz \\ & - \int_{-\Delta z}^{-\Delta z+w_{ring}} \int_{-\Delta\varphi-\pi/6}^{-\Delta\varphi} \frac{(\varphi+\Delta\varphi+\pi/6)(z+\Delta z-w_{ring})\cos(\varphi)}{\sqrt{r_c^{\ 2}+r_i^{\ 2}-2r_c r_i\cos(\varphi)+z^2}}\, d\varphi dz \\ & - \int_{-\Delta z-w_{ring}}^{-\Delta z} \int_{-\Delta\varphi}^{-\Delta\varphi+\pi/6} \frac{(\varphi+\Delta\varphi-\pi/6)(z+\Delta z+w_{ring})\cos(\varphi)}{\sqrt{r_c^{\ 2}+r_i^{\ 2}-2r_c r_i\cos(\varphi)+z^2}}\, d\varphi dz \\ & + \int_{-\Delta z}^{-\Delta z+w_{ring}} \int_{-\Delta\varphi}^{-\Delta\varphi+\pi/6} \frac{(\varphi+\Delta\varphi-\pi/6)(z+\Delta z-w_{ring})\cos(\varphi)}{\sqrt{r_c^{\ 2}+r_i^{\ 2}-2r_c r_i\cos(\varphi)+z^2}}\, d\varphi dz \Bigg) \end{aligned} \tag{4.13}$$

$$\begin{aligned} L_{1,2}^{rung} = \frac{\mu_0 r_c r_i}{4\pi w_{rung}^{\ 2}} \Bigg(& \int_0^{l_c-2w_{ring}} \int_{-\Delta\varphi-w_{rung}/r_c}^{-\Delta\varphi} \frac{2(\varphi+\Delta\varphi+w_{rung}/r_c)(z+l_c-2w_{ring})}{\sqrt{r_c^{\ 2}+r_i^{\ 2}-2r_c r_i\cos(\varphi)+z^2}}\, d\varphi dz \\ & + \int_0^{-l_c+2w_{ring}} \int_{-\Delta\varphi}^{-\Delta\varphi+w_{rung}/r_c} \frac{2(\varphi+\Delta\varphi-w_{rung}/r_c)(z+l_c-2w_{ring})}{\sqrt{r_c^{\ 2}+r_i^{\ 2}-2r_c r_i\cos(\varphi)+z^2}}\, d\varphi dz \Bigg) \end{aligned} \tag{4.14}$$

These integrals must be calculated to determine the mutual-inductance of two parallel strips, where one strip is placed on the original TxArray coil, and the other one is placed on the imaginary TxArray coil. To determine the mutual-inductance of parallel strips on the original coil, we need to replace all r_i by r_c. Δz and $\Delta\varphi$ should also be considered zero to determine self-inductances.

4.3.3 Numerical simulation

An unloaded 12-channel degenerate birdcage TxArray coil with fixed shield dimension and variability of other parameters within a reasonable range was considered to appreciate the advantage of the proposed optimization method. The length and radius of the shield were considered 400 mm and 200 mm, respectively. In the next stage, coil radius, coil length, end-ring width, and rung width were regarded as free design parameters. The coil radius was ranged from 150 mm to 190 mm, the coil length was ranged from 260 mm to 300 mm, the end ring width was ranged from 10 mm to 40 mm, and the rung width was ranged from 10 mm to 30 mm. Then the variables were optimized to minimize the error function expressed in Equation (4.7), i.e., $EF = \sqrt{\sum_{n=3}^{11} | L_{1,n} / L_{1,1} |^2}$. The solution corresponding to this case is denoted as EF_{min}. In order to clarify that dimensions can affect the coil's performance in terms of coupling, the variables were also adjusted to maximize the error function. The solution corresponding to this case is denoted as EF_{max}.

In the next step, two TxArray coils with the dimensions achieved from EF_{min} and EF_{min} cases were simulated at 123.2 MHz in ANSYS Electronics Desktop 2019 R2 (ANSYS Inc., Canonsburg, PA, USA). TxArray coils were loaded by a uniform cylindrical phantom with a radius of 60 mm, a length of 250 mm, a conductivity of 0.6 S/m, and a relative permittivity of 80. A cylindrical phantom placed in the center of the coil with a conductivity of 0.62 S/m, a relative permittivity of 80, a diameter of 153 mm, and a length of 350 mm is then used to load the coil. All conductors were defined as copper sheets with a finite conductivity boundary [106]. As suggested by the co-simulation strategy [76], the coil's capacitors were replaced by equivalent lumped ports, and after performing finite element analysis on the TxArray coils, a circuit simulation analysis was performed. In order to find the optimum capacitor values for each coil individually, an optimization strategy based on minimizing the magnitudes of the coil's scattering (**S**) parameters was implemented as follows

$$\min_{\bar{\mathbf{c}}} \quad \frac{1}{12} \sum_{n=1}^{12} \sum_{m=1}^{12} | s_{mn} |^2 \tag{4.15}$$

It should be noted that $\sum_{n=1}^{12}\sum_{m=1}^{12}|s_{mn}|^2$ is equivalent to the trace of $\mathbf{S^HS}$ in which the superscript **H** corresponds to the Hermitian transpose. Therefore, it is equal to the summation of the eigenvalues of $\mathbf{S^HS}$-matrix [67]. As earlier shown in Ref. [50], the eigenvalues of $\mathbf{S^HS}$-matrix, i.e., λ_n values, represent the normalized reflected power values for TxArray coil excitation eigenmodes. Previously, normalized reflected power was defined as the total reflected power (P_r^T) to the total incident power (P_i^T) and denoted as λ [50]. Hence, the optimization problem expressed in Equation (4.15) minimizes the average of λ_n values, which is characterized as λ_{av} ($\min\{\lambda_{av}\}$). Therefore, Equation (4.15) can be reduced to

$$\min\{\lambda_{av}\} \quad \Leftrightarrow \quad \min_{\bar{\mathbf{c}}} \quad \lambda_{av} \tag{4.16}$$

For the TxArray coil understudy in this chapter, the circularly-polarized (CP) excitation mode is one of the most critical mode of operation. In order to improve the performance of TxArray coils in the CP mode, another optimization strategy was implemented, which minimizes the normalized reflected power in the CP mode, i.e., λ_{CP}, in addition to minimizing λ_{av} ($\min\{\lambda_{av} + \lambda_{CP}\}$). The optimization problem was formulated as follows

$$\min\{\lambda_{av} + \lambda_{CP}\} \quad \Leftrightarrow \quad \min_{\bar{\mathbf{c}}} \quad \lambda_{av} + \lambda_{CP} \tag{4.17}$$

As can be observed, according to the proposed method, the design of the TxArray coil has changed from a traditional single-stage procedure to a two-stage procedure. Previously, the capacitors were optimized for a TxArray coil with predefined physical parameters [60, 73]. Here, before optimizing capacitors, the coil's physical parameters are optimized to decrease the magnetic coupling. Employing two presented optimization strategies in this chapter for finding the capacitor values can lead to a better understanding of how the second stage optimization can affect the coil's performance.

After finding the optimum capacitor values of TxArray coils, their performances in terms of matching and coupling levels and $\mathbf{B}_1^+$ efficiency were compared. The $\mathbf{B}_1^+$ efficiency was calculated as the average $\mathbf{B}_1^+$ within the phantom at the central axial plane for a unit total incident power in the CP mode.

4.4 Results

After determining **L**-matrix for different sets of variables, it was observed that increasing the coil radius reduces *EF*, while *EF* decreases with decreasing the coil length and the rung width. After a specific value, increasing the end-ring width is also decreasing *EF*. For the given range of the variables, EF_{min} was achieved when the coil radius is 190 mm, the coil length is 260 mm, the end-ring width is 40 mm, and the rung width is 10 mm. Besides, EF_{max} was achieved when the coil radius is 150 mm, the coil length is 300 mm, the end-ring width is 28.5 mm, and the rung width is 30 mm. Figure 4.5 shows the loaded TxArray coils corresponding to dimensions obtained for EF_{min} and EF_{max}. The *EF* ratio for these different coils, i.e., EF_{max}/EF_{min}, was calculated as 2.245.

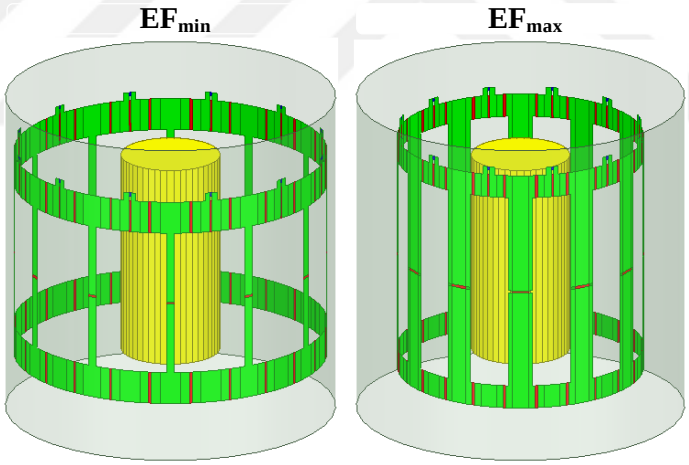

FIGURE 4.5 - EM simulation models of two shielded 12-channel degenerate birdcage TxArray coil loaded by a uniform cylindrical phantom with the minimum (left TxArray coil) and maximum (right TxArray coil) possible *EF* values.

The performance of the TxArray coils at 3T in terms of *EF*, reflection coefficient, maximum coupling, λ_{av}, λ_{CP}, $\mathbf{B}_1^+$ efficiency, and power delivered to the load normalized by the total incident power in the CP mode is evaluated and summarized in Table 4.1. The optimized capacitor values for each coil is also included in this table.

Table 4.1 shows that optimizing the coil's physical parameters for both min{λ_{av}} and min{$\lambda_{av} + \lambda_{CP}$} cases can improve the decoupling level. For the min{λ_{av}} case, the decoupling and matching levels achieved for the EF_{min} solution are -3.1 dB and -9.5 dB, respectively, lower than the values achieved for the EF_{max} solution. Also, the minimum λ_{av} obtained for the EF_{min} solution is half the value obtained for the EF_{max} solution. For the min{$\lambda_{av} + \lambda_{CP}$} case, the level of decoupling obtained for the EF_{min} solution is -6.6 dB lower than that of the EF_{max} solution. The matching levels for both solutions are approximately in the same range. Also, the minimum λ_{av} achieved for the EF_{min} solution is 34% lower than that of the EF_{max} solution. The results show that including λ_{CP} in the optimization process of capacitors enhances the coil's performance in the CP mode. As can be seen, for both solutions in the min{$\lambda_{av} + \lambda_{CP}$} case, less than 4% of the total incident power is reflected. Moreover, for the EF_{min} and EF_{min} solutions, 37% and 91% of the total incident power is absorbed by the load. In contrast, for the EF_{min} solution in the min{$\lambda_{av} + \lambda_{CP}$} case, 82% of the total incident power is reflected, and only 7% of that is delivered to the load. However, for the EF_{max} solution, the whole incident power is reflected. As a result, $\mathbf{B}_1^+$ efficiencies in the min{$\lambda_{av} + \lambda_{CP}$} case is much higher than the same values in the min{λ_{av}} case. The results of the min{$\lambda_{av} + \lambda_{CP}$} case revealed that minimizing coupling has a negative impact on the coil's performance in the CP mode, as $\mathbf{B}_1^+$ efficiency for the EF_{max} solution is 2.5-fold higher than the value achieved for the EF_{min} solution, which is contrary to expectations.

TABLE 4.1 - Summary of the performance of the simulated TxArray coils designed based on the minimum and maximum possible *EF* values

Minimization approach		min{λ_{av}}		min{$\lambda_{av} + \lambda_{CP}$}	
Coil type		EF_{min}	EF_{max}	EF_{min}	EF_{max}
Capacitor values	c_d	21.7 pF	27.5 pF	21.6 pF	21.2 pF
	c_t	50.3 pF	11.2 pF	49.1 pF	20.6 pF
	c_m	256.6 pF	253.6 pF	377.2 pF	147.1 pF
EF		2.19×10^{-2}	4.92×10^{-2}	2.19×10^{-2}	4.92×10^{-2}
$\lvert s_{nn} \rvert$ (dB)		-15.6	-6.1	-5.2	-5.6
$\max\{\lvert s_{mn} \rvert\}\big\rvert_{m\neq n}$ (dB)		-11.8	-8.7	-14.4	-7.8
λ_{av}		0.33	0.66	0.49	0.74
λ_{CP}		0.82	> 0.99	0.04	< 0.01
$\mathbf{B}_1^+$ efficiency in the CP mode ($\mu T/\sqrt{W}$)		0.36	0.04	0.84	1.23
$P_{phantom}/P_i^T$ in CP mode		0.07	$< 10^{-3}$	0.37	0.91

For a TxArray coil with a fixed shield dimension, increasing the coil radius can improve the decoupling level. However, increasing the radius of the TxArray coil reduces its distance from the imaginary coil. Decreasing this distance can have a destructive effect on the total produced field, as the fields generated by the imaginary TxArray coil will be more similar to the fields generated by the original coil except that they are in the opposite direction. Hence, there is a trade-off between increasing the coil radius that decreases the coupling level and reducing the coil radius that increases the $\mathbf{B}_1^+$ efficiency. In order to investigate this issue, 8 loaded 12-channel degenerate birdcage TxArray coils with various radii are simulated. The TxArray coils are quite similar to the TxArray coil designed for the EF_{min} solution (Figure 4.4(left)) except that their radii are varied between 140 mm and 195 mm. For each coil, the optimal capacitors were individually determined based on the $\min\{\lambda_{av}\}$ and $\min\{\lambda_{av} + \lambda_{CP}\}$ strategies.

Figure 4.6 compares the performance of the TxArray coils respect to r_c when the coil's capacitor values were optimized to minimize λ_{av} ($\min\{\lambda_{av}\}$). Figure 4.6A demonstrates reflection coefficients and maximum coupling levels at 123.2 MHz. As expected, increasing the coil radius leads to a better level of matching and decoupling. As shown in Figure 4.6B, both λ_{av} and λ_{CP} decrease as the coil radius is increasing. Also, for all 8 TxArray coils, λ_{CP} is higher than $\lambda_{av,}$ which reveals that the CP excitation mode is almost composed of the eigenmodes with a higher level of reflection. Figure 4.6C displays how increasing the coil radius can increase $\mathbf{B}_1^+$ efficiency in the CP mode. If the coil distance from the shield is more than 15 mm, the total incident power in the CP mode will be reflected entirely, resulting in a very low $\mathbf{B}_1^+$ efficiency. Figure 4.6D shows where the total transmitted power in the CP mode is consumed in each TxArray coil. The results show that the total accepted power by the coils is mostly dissipated in the coil's conductors and absorbed by the load. Dissipation power on the shield's conductors and losses due to the radiation are both negligible.

Figure 4.7 is also comparing the performance of the TxArray coils respect to r_c when the coil's capacitors were optimized to minimize both λ_{av} and λ_{CP} ($\min\{\lambda_{av} + \lambda_{CP}\}$). Figure 4.7A demonstrates that the lowest matching and decoupling levels could be achieved when the coil has the shortest distance from the shield. Figure 4.6B shows that increasing the coil radius could decrease λ_{av}, while it increases λ_{CP}. A comparison of Figures 4.7B and 4.6B illustrates that including λ_{CP} in the minimization problem

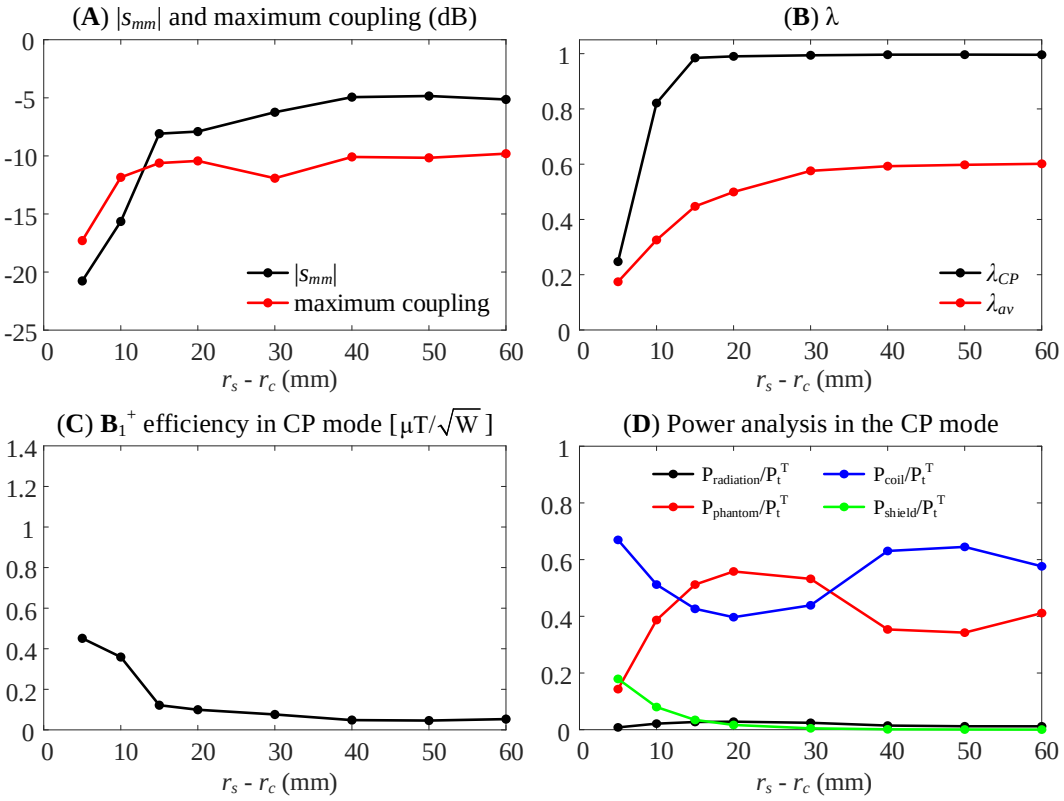

FIGURE 4.6 - Analysis performance of 8 loaded 12-channel degenerate birdcage TxArray coils designed by min{λ_{av}} approach with different r_c ranging from 140 mm to 195 mm when l_c = 260 mm, w_{ring} = 40 mm, w_{rung} = 10 mm, and r_s = 200 mm. (A) Reflection coefficient and maximum coupling, (B) λ_{av} and λ_{CP}, (C) $\mathbf{B}_1^+$ efficiency in the CP mode, and (D) power analysis in the CP mode.

can increase λ_{av}. Figure 4.7C indicates that the increase in the coil radius in the CP mode causes a decrease in $\mathbf{B}_1^+$ efficiency. The power consumption in the CP mode is also shown in Figure 4.7D. The results reveal that increasing r_c could increase the power loss due to the coil and shield conductors resulting in a less absorbed power by the load. It should be noted the CP mode is not only the excitation operation mode of these TxArray coils. Increasing the coil radius, which decreases λ_{av}, could enhance the average performance of the coil for all possible operation modes. However, to improve the coil's performance in the CP mode, r_c should be reduced. Therefore, the finding of the optimal coil radius is a trade-off between the minimization of λ_{av} and increasing $\mathbf{B}_1^+$ efficiency.

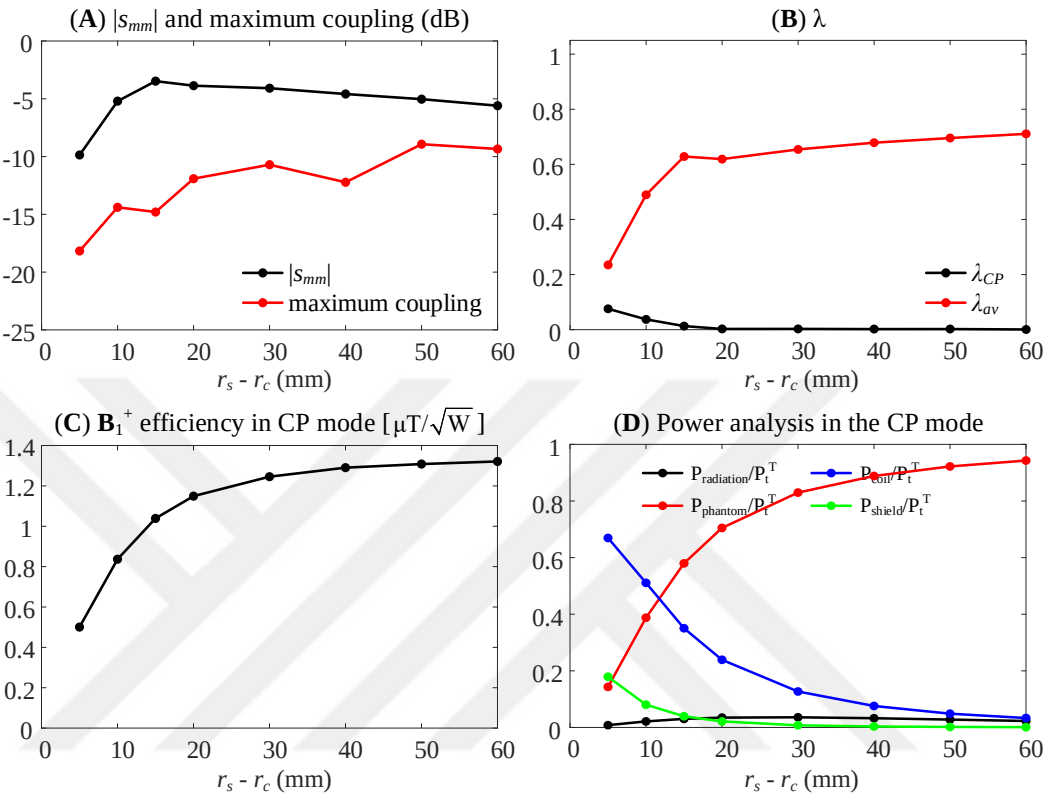

FIGURE 4.7 - Analysis performance of 8 loaded 12-channel degenerate birdcage TxArray coils designed by min{$\lambda_{av} + \lambda_{CP}$} approach with different r_c ranging from 140 mm to 195 mm when l_c = 260 mm, w_{ring} = 40 mm, w_{rung} = 10 mm, and r_s = 200 mm. (A) Reflection coefficient and maximum coupling, (B) λ_{av} and λ_{CP}, (C) $\mathbf{B}_1^+$ efficiency in the CP mode, and (D) power analysis in the CP mode.

4.5 Discussion and conclusion

In a typical TxArray coil building process, after the coil's general structure has been decided, the values of the discrete elements (mostly capacitors) are calculated using an optimization process. The limitation of the optimization process to assessing only capacitor values results in the loss of some of the TxArray coil's degrees of freedom. In this chapter, a theoretical approach was presented that, in addition to capacitor values, also considered TxArray coil sizes as a degree of freedom in the coil's design procedure. An optimization method was then introduced to minimize the magnetic coupling between non-adjacent transmit channels of a TxArray coil by optimizing some of its physical parameters. The method relied on calculating all self/mutual-inductances and minimizing the mutual-inductances normalized by the self-

inductances. The proposed approach was then employed to predict the optimum radius, length, and the width of end-rings and rungs of a shielded 12-channel degenerate birdcage 3T TxArray coil.

The optimization results demonstrated that for a degenerate birdcage TxArray coil enclosed by a shield with a fixed dimension, increasing the coil radius and end-rings width could minimize the coupling level. In contrast, reducing the coil length and the width of the rungs results in a reduction in the coupling level. The EM simulations results confirmed the optimum sizes obtained by the proposed method. However, the simulations were shown that increasing the coil radius could negatively impact the TxArray coil's performance in terms of $\mathbf{B}_1^+$ efficiency. The results of the simulations indicated that adequate coil distance from the shield could continue to improve the coil's $\mathbf{B}_1^+$ efficiency.

Chapter 5

Reconfigurable MRI Technology for Low-SAR Imaging of Deep Brain Stimulation at 3T: Application in Bilateral Leads, Fully-Implanted Systems, and Surgically Modified Lead Trajectories

5.1 Preface

The content of this chapter has been partially presented at the International Society of Magnetic Resonance in Medicine (ISMRM)'s 27th Annual Scientific Meeting [123] and published in NeuroImage [24]. The text, figures, and tables presented in this chapter are all based upon the journal publication [24]. Laleh Golestani Rad, Julie Pilitsis, Joshua Rosenow, Lawrence Larry Wald, Ergin Atalar, Behzad Elahi, Sunder Rajan, Alireza Vali, Boris Keil contributed to this chapter. I have been involved in the preparation of all the simulation files presented in this chapter, their data extraction, and the analysis and representation of the results.

5.2 Introduction

Deep brain stimulation (DBS) is a U.S. Food and Drug Administration (FDA)-approved neurostimulation procedure treating drug resistant Parkinson's disease (PD),

essential tremor (ET), and dystonia [124-128], with applications rapidly expanding to neuropathic pain [129, 130], obsessive compulsive disorder [131, 132], epilepsy [133], and Alzheimer's disease [134]. Although decades have passed since the inception of DBS and its clinical applications have grown exponentially, its biophysical mechanisms remain unclear. Uncertainties remain about which circuits are affected, which exact neural populations need to be targeted, and the most efficacious stimulation protocol [135]. There is a consensus that meticulous use of neuroimaging, both for target verification and for postoperative monitoring of functional changes induced in the affected brain networks can help interpreting clinical outcomes and design enhanced therapeutic protocols [136, 137]. Due to its excellent soft tissue contrast and non-invasive nature, magnetic resonance imaging (MRI) is excellently poised to answer open questions regarding DBS mechanism and targeting. Unfortunately, the interaction of radiofrequency (RF) fields of MRI scanners and implanted leads results in safety hazards that limit postoperative accessibility of MRI to these patients [138, 139]. Today, MRI of DBS patients is limited to MR-conditional devices, which require pulse sequences with a whole-head SAR of 0.1 W/kg (30 times below the FDA limit for imaging in the absence of conductive implants) and 3T systems are absolutely contraindicated [140, 141]. This excludes sequences that are essential to rule out complications (e.g., diffusion and T2-weighted imaging to detect stroke and hemorrhage), state-of-the-art fast imaging techniques that have become an integral part of functional studies (e.g., simultaneous multi-slice imaging [142]), and novel high-precision electrode localization methods (e.g., zero-TE phase imaging [143]).

The phenomenology of RF heating in the presence of conductive implants in the MRI environment has been studied extensively [144-149]. The consensus is that the tangential component of the electric field (E_{tan}) along the length of elongated conductive implants acts as a local voltage source generating RF currents on the leads. When these currents are dissipated in the tissue at the exposed tip of the lead, local SAR amplification and temperature rise will occur, which can damage the tissue. The past few years have witnessed a spike in feasibility studies investigating the applicability of parallel transmit methodologies to reduce the SAR during DBS MRI [18, 22, 43-45, 150-152], although such techniques have not been implemented in clinical settings yet. Recently, the concept of patient-adjustable reconfigurable MRI technology was introduced for DBS imaging at 1.5T. The system is based on a

mechanically rotating transmitter which steers a zero-electric field onto the electrode, then images with a high SNR close-fitting receive array [46, 47, 153]. Numerical simulations with realistic models of single isolated DBS leads demonstrated virtual elimination of SAR amplification around electrode contacts in nine patient models [46]. With promising preliminary results at 1.5T, substantial interest has arisen toward scaling the technology to higher fields where imaging can render significant benefits. The present work in this chapter sets the ground for the advancement of the reconfigurable MRI technology to 3T. Here, the scalability of the system for imaging at 127 MHz is assessed, its performance is evaluated in patients with bilateral implants and fully implanted systems, and for the first time, the result of modifications is reported in the DBS surgical procedure that enhances the subsequent performance of the new coil. Finally, the benefits of the technology are discussed in terms of the possibility of using pulse sequences currently not accessible to DBS patients due to their high SAR.

Below is a brief description of the motivations and novel contributions of this chapter.

5.2.1 Is reconfigurable MRI technology scalable to 3T?

Recent studies have demonstrated the feasibility of using a rotating transmit coil to reduce the SAR during MRI of DBS patients at 1.5T [46, 47, 153]. There is, however, a strong incentive toward DBS imaging at 3T for target verification and ruling out complications. This is because 1.5T MRI consistently underestimates the anterior and lateral boundaries of subthalamic nucleus and globus pallidus (DBS main target nuclei) compared to 3T fast gray matter T1 inversion recovery acquisitions [154], and a clear delineation between healthy and diseased tissue that allows detection of intracranial hemorrhage is better achieved at 3T.As the reconfigurable coil works by steering a low **E**-field region of the transmit coil such that it maximally contains the implant trajectory, question arises as whether this low **E**-field region is "thick" enough at 3T to fully contain realistic leads trajectories. This is especially important considering that DBS leads have complex trajectories with substantially out-of-plane segments, and that the spatial homogeneity of MRI RF fields is reduced at higher frequencies.

5.2.2 Applicability to bilateral leads

To date, studies that have investigated shaping or steering of MRI electric fields to reduce the SAR during DBS imaging have focused on single (unilateral) implants [22, 43, 150-152, 155, 156]. In practice, however, most patients with Parkinson's disease undergo bilateral lead implantation [157], and 52% of patients with essential tremor who originally receive unilateral DBS eventually need bilateral stimulation [158].

In the context of reconfigurable MRI, the optimal coil rotation angle to minimize the SAR depends on individual lead trajectories [46], meaning a rotating transmit coil has to be positioned at different angles to minimize the SAR of different leads. This raises the concern as whether the technique can ever be used in patients with bilateral implants. As far as is known, the issue of RF heating of bilateral DBS leads has not been addressed in the context of **E**-field steering techniques, including techniques based on parallel transmit and dual-drive systems [22, 43, 44, 150-152, 155, 156].

5.2.3 Isolated leads vs. fully implanted DBS systems

DBS surgery is performed in two stages. First, electrodes are implanted at specific target nuclei (e.g., subthalamic nucleus and globus pallidus for PD, ventrointermedius nucleus for ET) and the other end of the lead is tucked under the scalp for later connection to the neurostimulator (Figure 5.1A). MRI is useful at this stage for electrode localization and target verification [137]. In the next step, an implantable pulse generator (IPG) is implanted in the chest or abdomen, and leads are connected to the IPG via subcutaneous extensions (Figure 5.1B). Functional MRI studies that seek to disclose the neuromodulatory effect of DBS are performed on fully implanted systems [159].

To date, the performance of SAR reduction strategies based on **E**-field steering has been only investigated in isolated leads. However, it is established that the presence, position, and configuration of the IPG have a significant effect on RF heating [160, 161]. Therefore, it is imperative to investigate the efficacy of field-shaping techniques when applied to fully implanted DBS systems.

5.2.4 Surgical lead management combined with rotating coil technology

Unlike the meticulously planned intracranial trajectory of the electrode, for which almost every neurosurgeon follows textbook guidelines to determine the entry point on the skull and chose the angle of penetration to the target nuclei, there are no guidelines for the placement of extra cranial portions of the leads. Commercial DBS leads come in a series of fixed lengths at 30 cm, 40 cm, and 50 cm, which are longer than the distance from the surgical burr hole (where leads exist the skull) and the point where leads are connected to extensions (Figure 5.1). Surgeons usually loop the leads arbitrarily on the skull to avoid positioning the excess material against soft tissue of the neck. This, causes a large variation in lead trajectories depending on surgeons' preference and practice style.

The concept of surgical lead management to reduce the risk of MRI RF heating was first introduced by Baker in phantom studies [162], suggesting the use of external guides to incorporate concentric loops in the trajectory of DBS leads to reduce RF

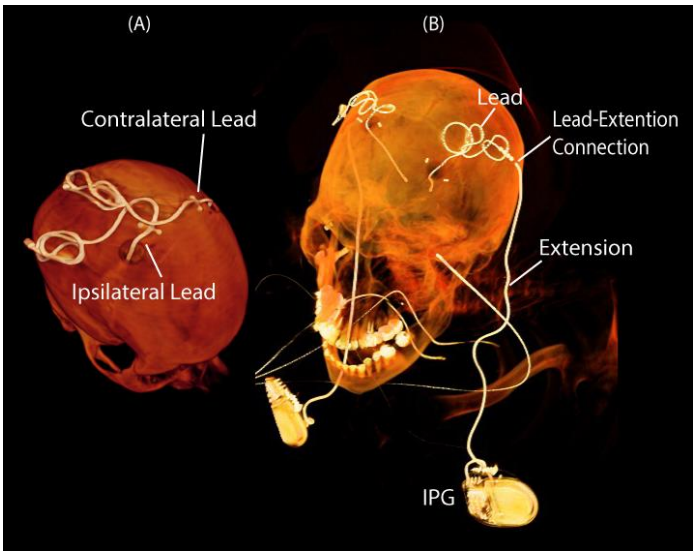

FIGURE 5.1 - CT images of patients with isolated and fully implanted DBS devices. (A) Patient with bilateral leads prior to their connection to the implantable pulse generator (IPG). Labels "contralateral" and "ipsilateral" are with respect to the body side that the IPG is planned to be implanted later. (B) A patient with a fully implanted DBS system consisting of two IPGs, two leads, and two extension cables connecting leads to the IPGs.

heating during MRI at 1.5T and 3T. These findings were later corroborated in simulation studies [163] and demonstrated to be practically implementable in clinic [149]. Theoretically, lead management techniques can be modified for use in combination with **E**-field steering techniques to augment their benefit. This chapter reports the first result of implementing such surgical modifications tailored to enhance the performance of reconfigurable MRI technology.

In what follows, a brief overview of the theory and concept of reconfigurable coil technology is given for low-SAR DBS imaging, the details of coil design, numerical simulations, and patient models are discussed; the SAR reduction performance of the coil is evaluated for unilateral and bilateral DBS leads as well as fully implanted systems; a surgical lead management strategy that significantly enhances the performance of the rotating coil is introduced; and the sensitivity of coil positioning to operational errors and electrical properties of the tissue is discussed. Finally, the temperature rise in the tissue around tips of DBS leads is investigated during eight typical MRI exams in a patient will fully implanted DBS system scanned with the body coil as well as the rotating coil in its optimum position.

5.3 An overview of patient-adjustable MRI coil technology

An overview of the working principle of the reconfigurable MRI coil technology is given in Figure 5.2, depicting a linearly-polarized (LP) rotating birdcage transmitter loaded with a human head implanted with a patient-derived model of bilateral DBS leads. The electric field of the coil is given on a transverse plane passing through the center of the head. Such a linearly-polarized birdcage transmitter has a slab-like region of the low electric field, which can be steered to coincide with the implant trajectory by mechanically rotating the coil around the patient's head. Figure 5.2B gives the maximum of 1g-averaged SAR around tips of left and right DBS leads as the coil rotates around the patient's head. As it can be observed, local SAR around DBS contacts can be minimized by positioning the coil at an optimum rotating angle such that the low **E**-field region maximally contains lead trajectories.

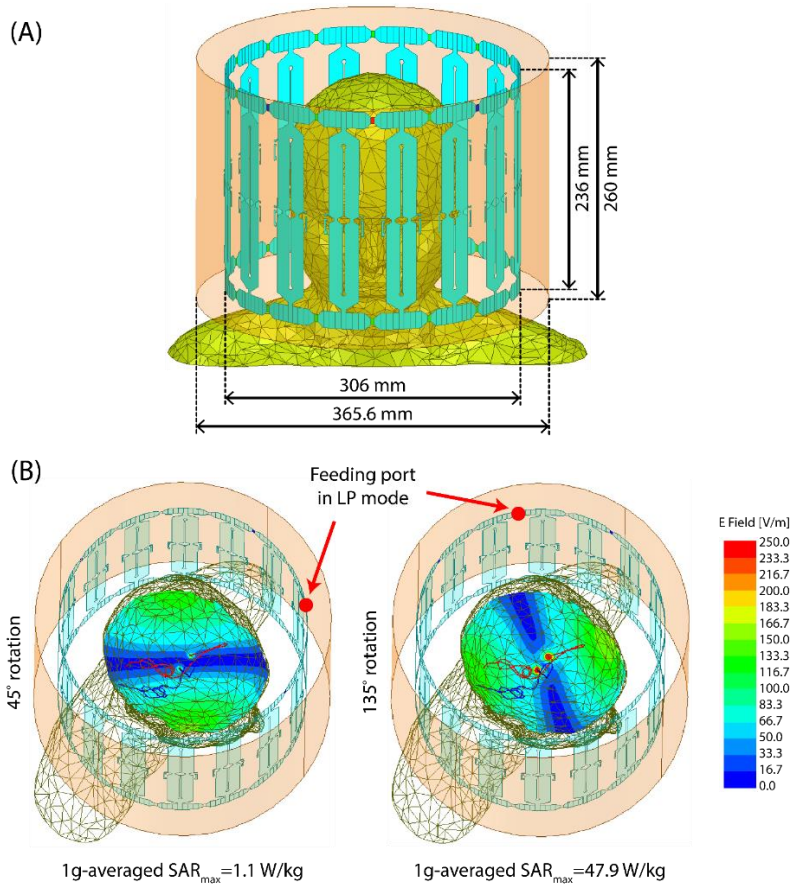

FIGURE 5.2 - Overview of the working principle of the rotating coil system. A linearly polarized birdcage transmitter has a slab-like region of low electric field. The orientation of this low **E**-field region can be steered by mechanically rotating the coil around patient's head. The heating of conductive wire implants can be minimized when they are maximally contained within this low field region. In this figure, the coil input power is adjusted to produce a mean $\mathbf{B}_1^+ = 2$ μT on a central axial plane passing through the head.

5.4 Numerical simulations: Rotating coil and patient models

To assess the performance of the rotating coil system at 3T, realistic lead models were constructed from postoperative computed tomography (CT) images of 13 patients implanted with bilateral DBS leads. From these, 12 patients had isolated leads, and one patient had a fully implanted DBS system with bilateral IPGs. The prospective use of imaging data for simulation and modeling was approved by the ethics review board of Northwestern University and by the Institutional Review Board at Albany Medical

College. Details of image segmentation and model construction were similar to those reported in Ref. [149]. The coil was a shielded 16-rung high-pass linearly-polarized birdcage transmitter with a diameter of 306 mm and a length of 236 mm, fed through a cable connected to the upper ring over a matching capacitor. The reference position for the feed ($\varphi = 0°$) was set to be in front of the patient's nose. The shield was an open solid copper cylinder with a length of 260 mm and a diameter of 365.6 mm. ANSYS Electronics Desktop 18.2 (ANSYS Inc. Canonsburg PA) was used to implement numerical simulations. The coil was tuned and matched to operate at 127 MHz using a combined finite element method and circuit analysis approach, as described in Refs. [46, 47, 76, 149, 163, 164].

Isolated lead models were registered to a homogeneous head phantom ($\varepsilon_r = 76$, $\sigma = 0.47$ S/m) that extended to the base of the neck. The fully implanted system was modeled using the silhouette of the patient constructed from head and chest CT images. Figure 5.3 shows patient-derived models and details of DBS contact electrodes.

For each patient model, the coil was rotated around the head with 5.625° increments and the maximum of 1g-averaged SAR was calculated around tips of left and right DBS leads in a 20 mm × 20 mm × 20 mm cubic area that surrounded all four electrode contacts (Figure 5.4). SAR values were calculated based on the IEEE STD P1528.4 recommendation [165] using the built-in SAR calculator module in ANSYS HFSS. Although there are FDA recommended limits of 3.2 W/kg for the global head SAR, and 10 W/kg for 10g-averaged local head SAR when operating in normal mode, there is no guideline for the local SAR in the presence of medical implants. However, it is well established that implant-induced RF heating is a local phenomenon that occurs in the first few millimeters of the device and dies off fast [166]. For this reason, 1g-averaged local SAR was calculated, which gives a more focal description of heating in the vicinity of DBS leads.

A fine mesh resolution was enforced in the tissue surrounding electrode contacts with the mesh size < 0.7 mm. The mesh size on metallic contacts and internal wires was set to be < 0.3 mm. The computing space had ~4 million tetrahedral mesh after numerical convergence was achieved. Total computation time for each finite element simulation was ~ 4 hours on a Dell PowerEdge R740xd system with 1.5 TB RAM and two Intel(R) Xenon(R) Gold 6140 CPUs (2.30 GHz, 18 cores).

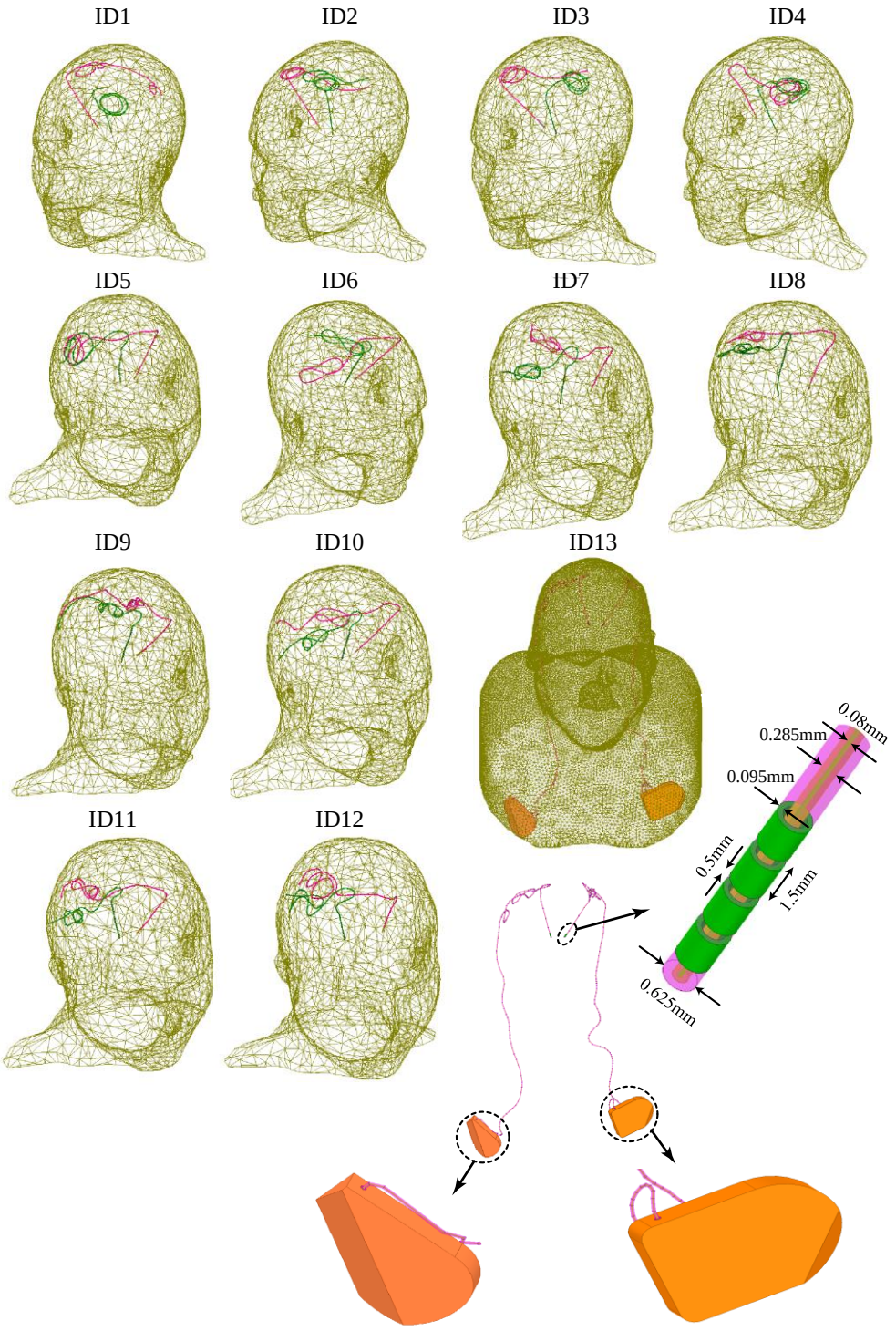

FIGURE 5.3 - Reconstructed models of DBS leads registered in a head phantom for finite element simulations. CT images of 12 patients with isolated leads and one patient with a fully implanted system were used to extract lead trajectories. Models of electrode contacts and the insulation were built around each trajectory.

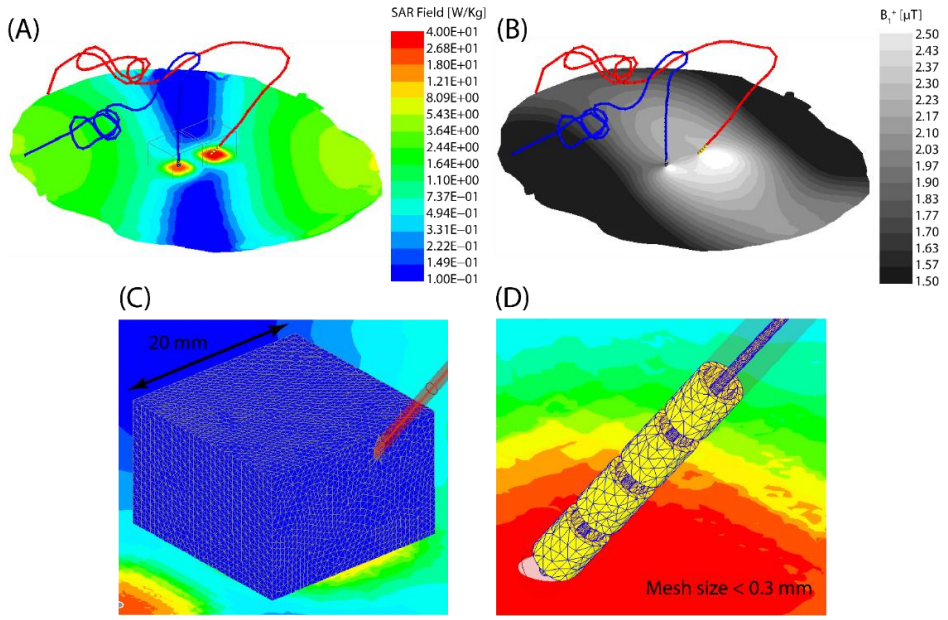

FIGURE 5.4 – (A) Spatial distribution of 1g-averaged SAR around DBS contact leads. The maximum of local SAR was calculated inside a cubic area surrounding all four electrode contacts. (B) The spatial distribution of $\mathbf{B}_1^+$ field on a central axial plane. For all simulations, the input power of the coil was adjusted to produce a $\mathbf{B}_1^+$ field with a spatial mean of 2 μT. (C-D) Finite element mesh in the area surrounding the leads and on the electrode contacts. Mesh resolution was < 0.7 mm in the cubic area surrounding the leads and < 0.3 mm on the electrode contacts.

A total of 832 simulations were performed (13 patients × 64 coil positions). To compare the SAR of linearly-polarized rotating coil with the SAR generated by a conventional circularly polarized (CP) body coil, a typical 3T high-pass birdcage coil was simulated with dimensions given in the literature [167]. To properly load the body coil, isolated DBS leads were registered into a homogeneous head and torso phantom that extended to the upper chest. Details of the body coil's geometry, head and torso phantom, and positioning of patient-derived DBS lead models in the body coil are given in Figure 5.5. For all simulations, the input power of the coils was adjusted to produce a $\mathbf{B}_1^+$ on a central axial plane with a spatial mean of 2 μT.

5.5 SAR reduction performance

Figure 5.6 (solid lines) gives the maximum of 1g-averaged SAR (Max1gSAR) around tips of right and left DBS electrodes for a full range of coil rotation angles. The Max1gSAR generated in the tissue by the body coil is also given for comparison

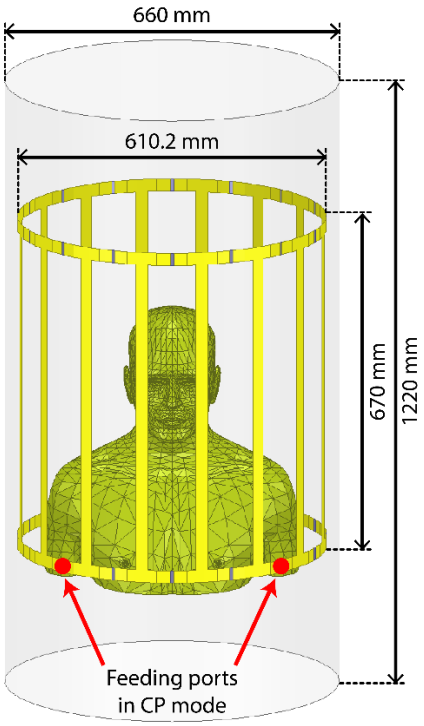

FIGURE 5.5 - Model of a typical high-pass CP birdcage coil at 3T. The body model has been extended to the chest to load the body coil properly.

(dashed-lines). For 11 patients, including the one with the fully-implanted system, an optimum coil rotation angle could be found that reduced the SAR at tips of both leads to a level below the Max1gSAR generated by the coil operated in CP mode.

5.5.1 SAR reduction for unilateral leads

To quantify the SAR-reduction performance of the coil, a metric called SAR-reduction efficiency (SRE) was defined for each lead and at each coil rotation angle as:

$$\mathrm{SRE}_{Uni,n,i}(\varphi) = 100 \times \frac{\mathrm{Max1gSAR}_{CP,n,i} - \mathrm{Max1gSAR}_{LP,n,i}(\varphi)}{\mathrm{Max1gSAR}_{CP,n,i}} \qquad (5.1)$$

where $\mathrm{Max1gSAR}_{CP,n,i}$ is the maximum of 1g-averaged SAR at the tip of lead i (i = right, left) in patient n generated by the CP body coil, and $\mathrm{Max1gSAR}_{LP,n,i}(\varphi)$ is the maximum of 1g-averaged SAR at the tip of lead i in patient n generated by the linearly-polarized rotating coil positioned at angle φ.

When considering each lead alone, an average SRE of 83.06%±12.38% was achieved over all 26 leads. The unilateral SRE was positive for all leads, meaning that a rotating position could always be found that reduced the SAR at the tip of a unilateral

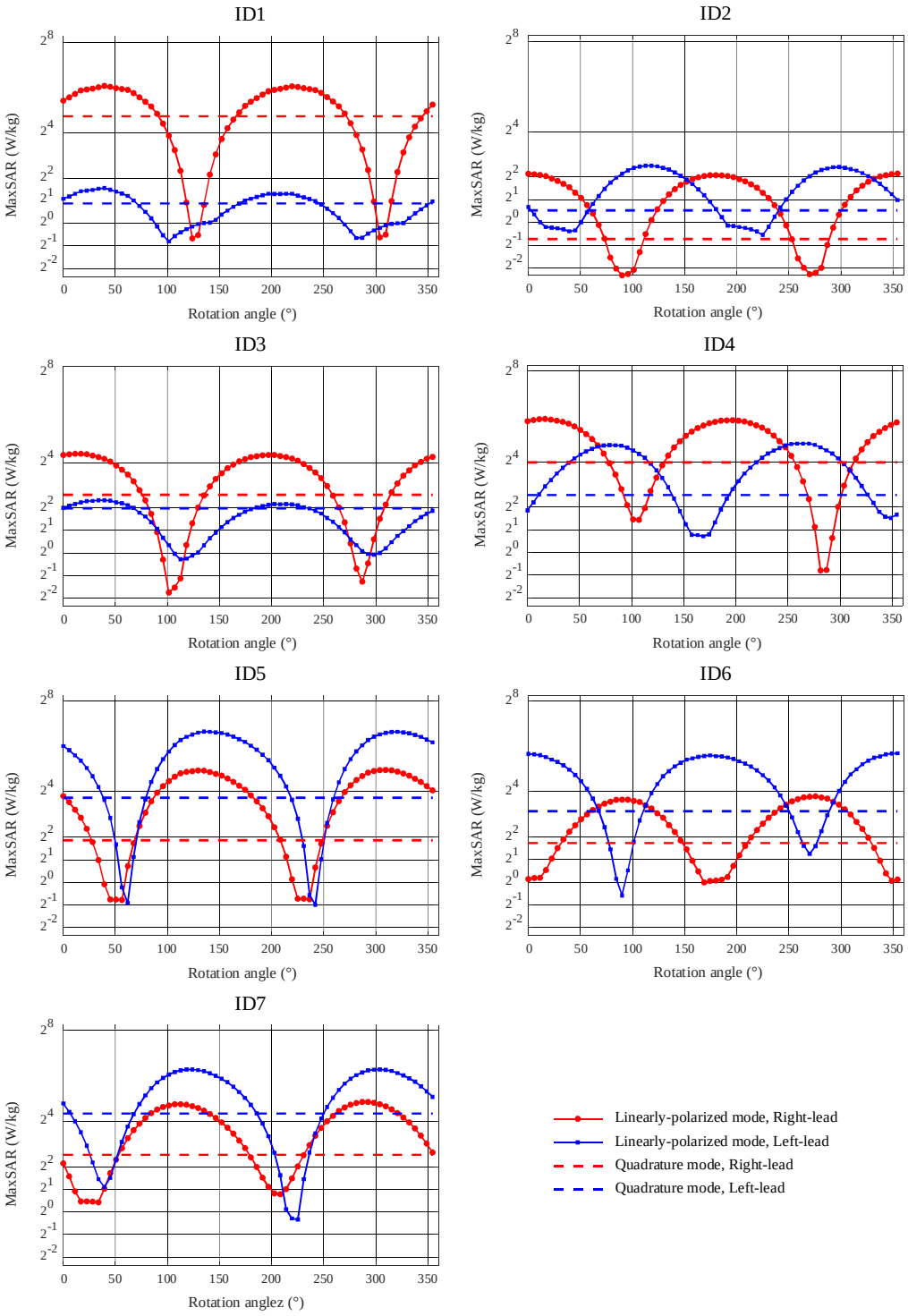

FIGURE 5.6 - The maximum of 1g-averaged SAR calculated around tips of left and right DBS leads as a function of rotating coil angle φ° (solid lines). The input power of the coil is adjusted to generate a mean $\mathbf{B}_1^+ = 2$ μT on a central axial plane. The maximum of 1g-averaged SAR is also given for the body coil generating the same mean $\mathbf{B}_1^+ = 2$ μT (dashed-lines).

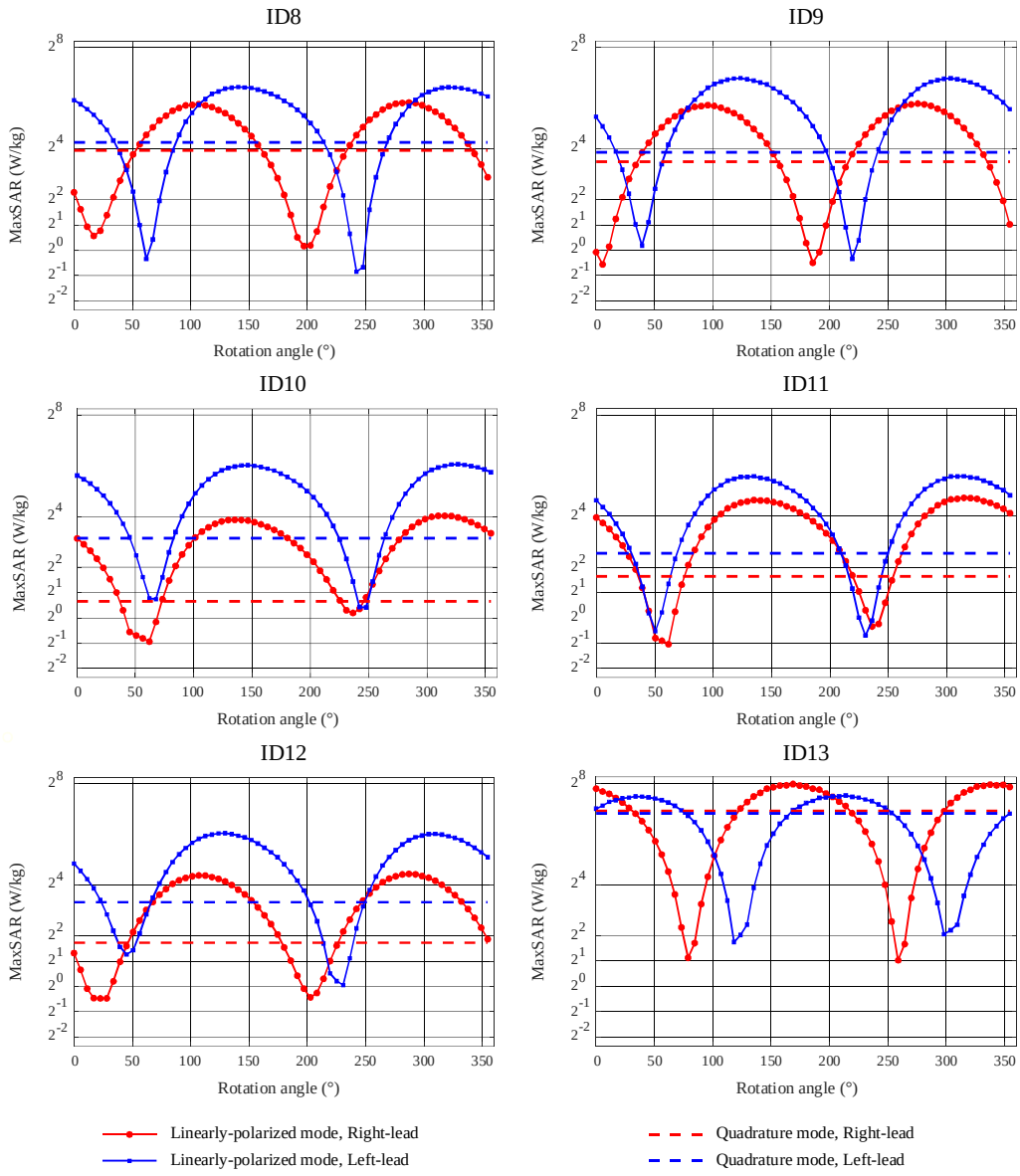

FIGURE 5.6 (continued) - The maximum of 1g-averaged SAR calculated around tips of left and right DBS leads as a function of rotating coil angle $\varphi°$ (solid lines). The input power of the coil is adjusted to generate a mean $\mathbf{B}_1^+ = 2$ µT on a central axial plane. The maximum of 1g-averaged SAR is also given for the body coil generating the same mean $\mathbf{B}_1^+ = 2$ µT (dashed-lines).

lead to a value below the SAR generated by the body coil. As expected, the optimum coil rotation angle that minimized the SAR was different for each lead, emphasizing the importance of taking realistic trajectories into account [132-134].

Figure 5.6 also demonstrates the periodic nature of the SAR profile exhibiting two minima as the coil rotates a full circle. The mean value of the first optimum rotation angle was 73.99°±41.65° averaged over all leads. From the practical point of view, this means that constructing the coil housing such that allows 180° rotational maneuverability around a default feed position at 73.99° will be sufficient to cover most typical DBS cases.

5.5.2 SAR reduction for bilateral leads

A bilateral SAR reduction metric can be defined as:

$$\mathrm{SRE}_{Bi,n}(\varphi) = 100 \times \frac{\mathrm{Max1gSAR}_{CP,n} - \mathrm{Max1gSAR}_{LP,n}(\varphi)}{\mathrm{Max1gSAR}_{CP,n}} \tag{5.2}$$

where the $\mathrm{Max1gSAR}_{CP/LP,n}$ is the maximum of 1g-averaged SAR in the tissue of patient n at whichever lead that produces the higher SAR. When considering both

TABLE 5.1 - Maximum of unilateral and bilateral SAR Reduction Efficiency ($\mathrm{SRE}_{Uni,n,i}$ and $\mathrm{SRE}_{Bi,n}$) for each patient and their corresponding optimum coil rotating angles

Patients	Coil angle (°)	$\mathrm{SRE}_{\text{Right-lead}}$ (%)	Coil angle (°)	$\mathrm{SRE}_{\text{Left-lead}}$ (%)	Coil angle (°)	$\mathrm{SRE}_{\text{Bilateral}}$ (%)
ID1	124	98	101	69	124	97
ID2	90	67	39	47	56	-18
ID3	101	95	113	79	113	86
ID4	107	83	169	72	124	22
ID5	56	84	62	96	56	94
ID6	169	70	90	92	68	-15
ID7	34	77	39	89	39	89
ID8	17	90	62	96	45	49
ID9	6	94	39	92	28	52
ID10	62	67	68	81	68	81
ID11	62	84	51	88	51	88
ID12	23	78	45	76	39	71
ID13	79	98	118	97	101	70
Mean	71	83	77	83	70	59
Standard deviation	45	11	38	14	32	38

leads, an average bilateral SRE of 59%±38% was achieved over all patients. Table 5.1 gives the values of the maximum of $SRE_{Uni,n,i}$ and $SRE_{Bi,n}$ for each patient and their corresponding optimum coil rotating angles.

5.6 Surgical lead management to enhance the performance of reconfigurable coil

The feasibility and effectiveness of surgeon-initiated improvements in the routing of DBS leads to mitigate the risk of MRI-induced RF heating has been recently brought into attention [149]. Regarding the reconfigurable coil technology, one can think of implementing similar surgical strategies that ensure the optimal performance of the rotating coil for bilateral leads. This can be achieved by implementing a few modifications. First, incorporating concentric loops close to the surgical bur hole will further reduce the SAR amplification at tips of both left and right leads through the cancelation of induced voltages, as described in Ref. [149]. Second, aligning and overlapping the trajectories of right and left leads and extension cables will allow the rotating coil to maximally contain both leads in its low E field region and thus minimizing the SAR at the tips of both implants simultaneously. In cases where two IPGs are implanted bilaterally to stimulate left and right leads separately, this can be done by careful planning to assure both leads, extensions, and IPGs are positioned into the same coronal plane. In the case where a single double-channel IPG is implanted unilaterally to stimulate both leads, this can be done much easier by overlapping extension cables.

To assess the feasibility of implementing surgically modified lead trajectories, a 74-year-old female PD patient was implanted with a dual-channel IPG (Medtronic ACTIVA PC, Medtronic Inc., Minneapolis MN) stimulating both left and right leads. To guide the lead trajectory, curved mayo scissors that passed posterior and to the left of the incision were used. The blades of the scissors were then opened to their widest to create a pocket for a coiled lead to be inserted (Figure 5.7). The lead was looped into 2-3 concentric circles at the burr-hole, and the rest of the lead was passed toward the temporal lobe where it would be later connected to the extension. The IPG was implanted in the left pectoralis (Figure 5.8). Leads and extension trajectories were aligned and overlapped, as shown in Figure 5.8. A head and chest CT image of the

patient was acquired after the full system was implanted, and lead and extension trajectories were extracted from the image for model construction and simulations similar to previous patients.

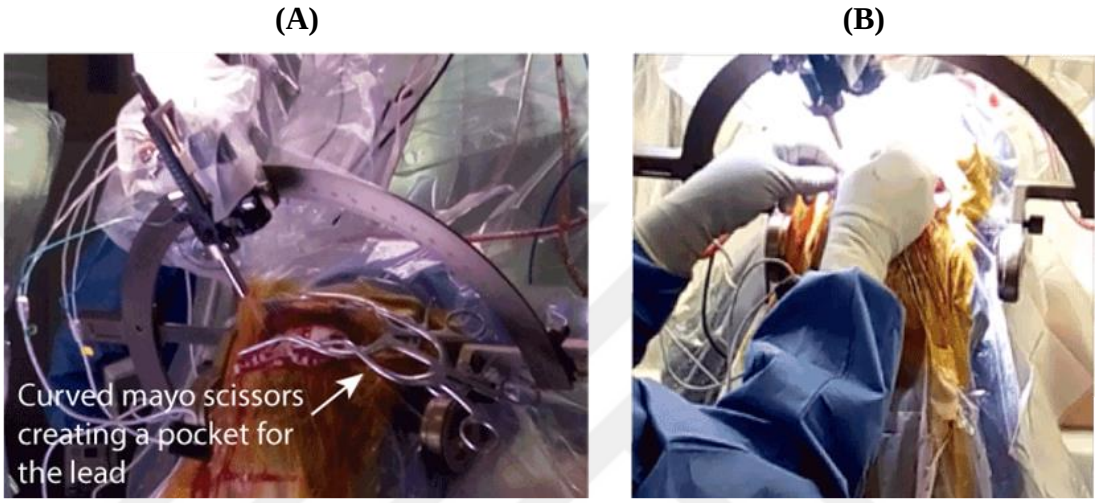

FIGURE 5.7 – (A) curved mayo scissors with blades opened to the max were used to create a pocket for the looped leads to be inserted. (B) Leads were looped 2-3 turns concentrically and placed on top of the surgical burr hole.

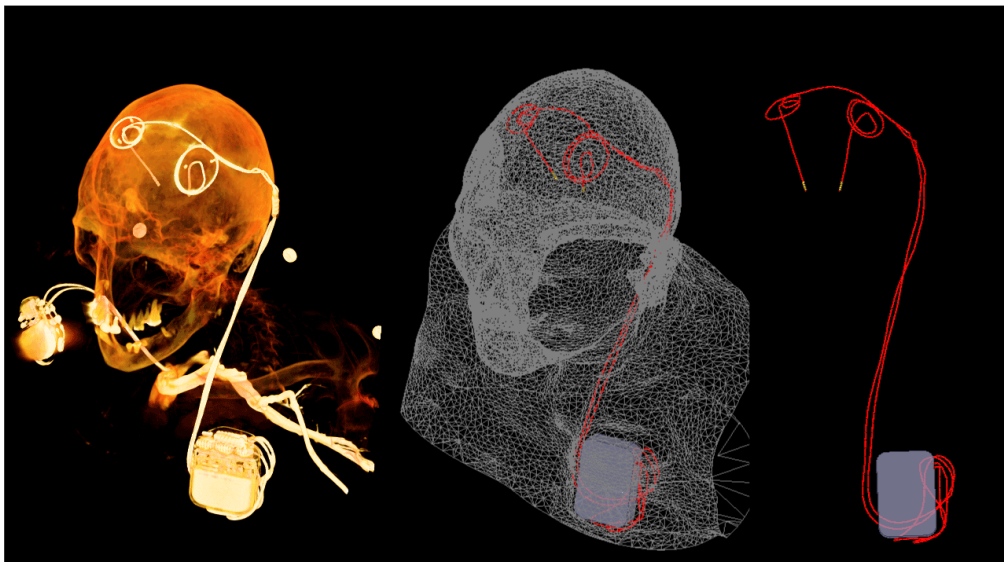

FIGURE 5.8 - Postoperative CT image of a patient implanted with bilateral DBS leads connected to a double-channel pulse generator implanted in the right pectoral region. Concentric loops were incorporated into lead trajectories at the surgical burr. The rest of the lead trajectories and extension cables were aligned and overlapped to follow the same path. A model of the patient's silhouette and the fully implanted device was constructed based on the CT image for finite element simulations.

Figure 5.9 gives the maximum of 1g-averaged SAR at the tips of left and right DBS leads as a function of the coil's rotation angle. The SAR values generated by the body coil are also given for comparison. As expected, when lead trajectories are surgically overlapped, the SAR profile of left and right leads vary in phase. A maximum bilateral SRE of 95% could be achieved in this case for the coil positioned at φ = 95.625°.

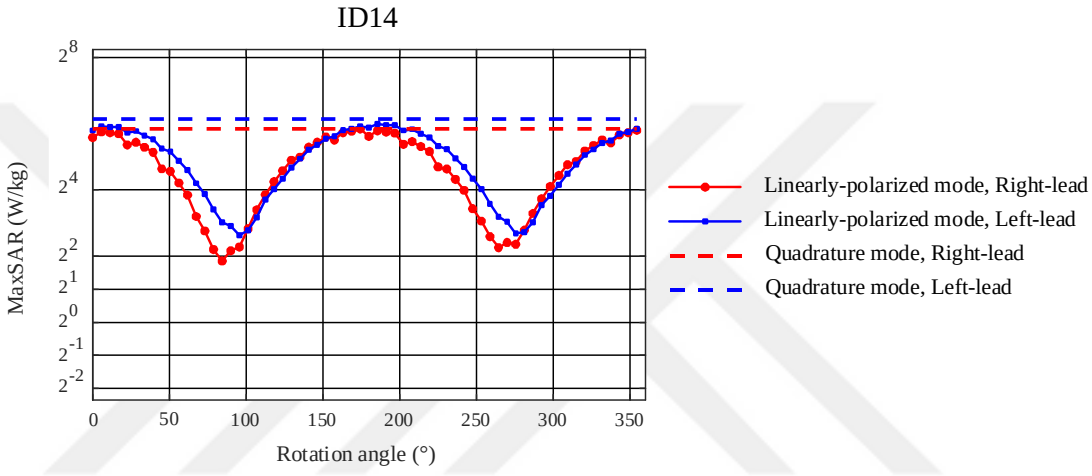

FIGURE 5.9 - The maximum of 1g-averaged SAR calculated around tips of left and right DBS leads of patient #14 as a function of rotating coil angle φ° (solid lines). The input power of the coil is adjusted to generate a mean $\mathbf{B}_1^+$ = 2 μT on a central axial plane. The maximum of 1g-averaged SAR is also given for the body coil generating the same $\mathbf{B}_1^+$ (dashed-lines). As expected, when lead trajectories are overlapped the SAR profiles of right and left leads vary very similarly as a function of the coil rotation angle. This significantly enhances bilateral SAR reduction by allowing simultaneous SAR minimization at the tips of both leads at a common optimum angle.

5.7 Sensitivity to operational errors

From Figure 5.6, it can be observed that large deviations from the coil's optimal angle generate a SAR that is higher than the SAR produced by the body coil (when normalized to the same $\mathbf{B}_1^+$). This has important safety implications considering both operational errors and uncertainties in determining the optimum angle. To assess the sensitivity of SAR to the deviation of the coil from its optimal position, a metric called permissible rotation range (PRR) was defined as the maximum deviation from the optimal position in either direction that increased the SAR to the level produced by the CP coil:

$$PRR_i = |\varphi_{i,opt} - \varphi_{i,CP}| \quad (5.3)$$

where $\varphi_{i,opt}$ is the optimum angle for lead *i* and $\varphi_{i,CP}$ is the angle that produces the SAR equal to the SAR generated by the CP coil. PRR was 20.16°±12.78° averaged over leads. For a coil constructed such that it allows rotational increments of 5° (which is practical), the PRR will be at least 4 times larger than the coil's rotation resolution.

5.8 Effect of electrical properties of the tissue on optimal coil position

A possible approach to determine the optimal position of the coil for individual patients is to perform simulations on patient-derived models of implanted device to determine the coil position that minimizes the SAR for each individual. If such simulation approach is adopted, it will be important to evaluate the sensitivity of the coil's positioning to electrical properties of the body model. To assess this, simulations were repeated in two cases with (a) a patient with isolated bilateral leads (ID5, Figure 5.3) and (b) the patient with a fully-implanted system and a double-channel unilateral IPG (ID14, Figure 5.7), with a range of low to high tissue conductivities covering the limits reported in the literature (0.2 S/m - 0.65 S/m). Figure 5.10 gives the result of Max1gSAR as a function of the coil rotating angle for each tissue conductivity. As expected, the absolute value of the SAR changed by varying the conductivity of the tissue. However, the position of the coil's optimum angle was insensitive to the electrical properties of the body model (< 1° change).

5.9 Temperature rise in the tissue during typical clinical scans

Although local SAR has been widely used as a surrogate to predict the severity of RF heating during MRI, temperature rise in the tissue (ΔT) is the ultimate measure of RF safety that dictates the limits. To have an estimate of the rotating coil's performance in terms of reducing the temperature rise in tissue, ΔT was calculated around the tips of left and right leads in patient 14 during eight typical MRI exams. Simulations were performed for the rotating coil positioned at its optimum angle as well as the scanner's built-in body coil, where the input power to both coils was adjusted to produce the

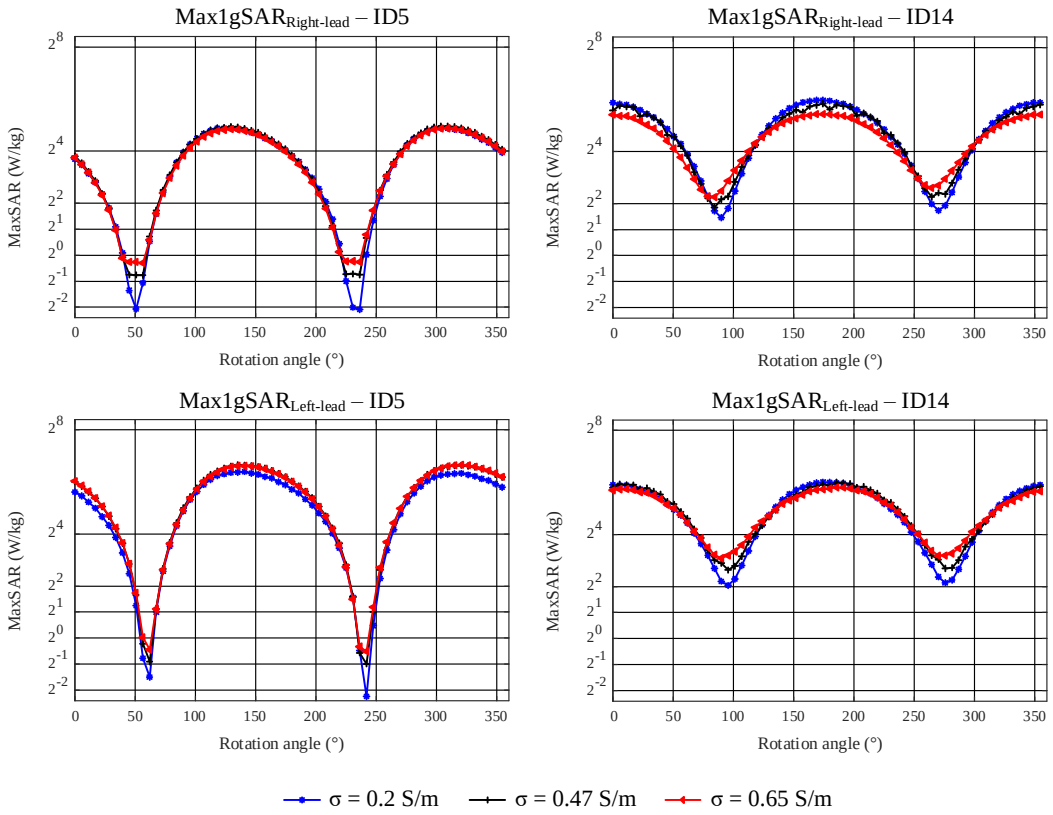

FIGURE 5.10 - Maximum of 1g-averaged SAR in the tissue of patients 5 and 14 as a function of different coil rotation angles and at different values of tissue conductivity. The predicted optimum angle of the coil was insensitive to changes in the change of tissue's electrical property.

same flip angle on a central axial plane passing through the head. Table 5.2 gives the sequences and their parameters. Combined electromagnetic-thermal simulation was performed as described in Ref. [164]. Scan parameters of Table 5.2 are based on typical clinical sequences on a Siemens 3T Skyra system that routinely is used in the Department of Radiology at Northwestern University. Thermal simulations were performed using the transient thermal analyses solver of ANSYS Mechanical (ANSYS Inc., Canonsburg, PA), which solves the Penne bioheat equation:

$$c\rho\frac{\partial T}{\partial t}-\nabla k\nabla T=\rho(SAR) \tag{5.4}$$

where c is the specific heat capacity of the tissue (4150 Jkg-1C-1 W/m/C [168]), k is the isotropic thermal conductivity (0.42 W/m-1C-1 [168]), ρ is the density (1000

kg/m^3), and *T* is the temperature. The initial body temperature was set to 37°C. ΔT in the tissue generated by the rotating coil in its optimum angle remained below 1°C for all imaging sequences, whereas temperature increases as high as 10.8°C was reached during imaging with the body coil.

TABLE 5.2 - Sequences and scan parameters used in typical brain exams and in thermal simulations. Here TR refers to repetition time, TE to echo time, FOV to field of view, FA to flip angle, and ST to slice thickness.

Index	Sequence	TR (ms)	TE (ms)	FOV (cm)	$\mathbf{B}_1^+$ (μT)	Acq. Time (s)	ΔT [°C] Body coil / LP coil
1	Localizer	8.6	4	250	0.4	0:13	< 0.1° / < 0.1°
2	AX T1 TSE	486	13	200	2.4	2:46	6.9° / 0.3°
3	AX T2 TSE	4500	83	240	2.8	3:47	10.8° / 0.7°
4	AX FLAIR	9000	81	220	1.7	2:44	2.2° / 0.2°
5	AX CISS	8.21	3.81	180	2.4	5:30	8.0° / 0.4°
6	AX 3D TOF	21	3.43	200	2.3	5:52	7.1° /0.5°
7	Diffusion	6600	99	220	1.3	1:54	2.0° / 0.1°
8	fMRI	2020	20	170	0.9	8:33	1.3° / < 0.1°

5.10 Discussion and conclusion

A significant obstacle to develop and test hypotheses on the mechanism of action of DBS is the lack of a quantitative understanding of the extent and influence of the stimulation on the neural elements involved. Much of the scientific effort to address this question has focused on the cellular effects of stimulation near the electrode [169-177]. While this interesting question continues to be explored, it is proposed that it may not be the fundamental issue underlying the therapeutic mechanisms of DBS, and that changes in the underlying dynamics of the stimulated brain networks may represent the intervention's core effect [178]. When investigating the neuromodulatory effects of DBS, neuroimaging studies have largely used either positron emission tomography (PET) or single photon emission tomography [179, 180]. MRI has clear advantages to both of these techniques due to its excellent soft-tissue contrast, easy access, non-invasive nature, and the richness of the post-processing analytical methods that are available to use. Present MRI technology, however, is limited in its post-operative applicability for DBS patients due to safety risks.

In the past few years, manufacturers of electronic implantable medical devices have largely reduced the use of ferromagnetic components to diminish the risk of device dislodgement due to static magnetic fields. Device programming has also been significantly enhanced to minimize the risk of malfunction due to interference from gradient fields. RF heating, however, remains a major challenge. Although some manufacturers have relaxed their guidelines to allow the use of body coils, which was previously prohibited, major practical challenges are virtually unaffected as stringent power monitoring remains in place (new guidelines limit the maximum RMS of $\mathbf{B}_1^+$ field to 2 μT and in cases where the scanner does not report the B field, the more conservative whole-head SAR limit of 0.1 W/kg should be applied). Considerable effort has been dedicated to understand and control safety risks by characterizing the problem of RF heating accounting for factors such as lead configuration [139, 162, 163, 181], the position with respect to MRI RF coil [144, 160, 164], and lead material [182, 183]. There is, however, a consensus that MRI RF safety is a complex phenomenon with a plethora of interplaying factors. As such, it should be tackled from different fronts, meaning that efforts in designing MR-compatible leads, novel DBS-friendly MRI coils, and surgical lead management should be combined together to mitigate the risks effectively.

Recently the concept of reconfigurable MRI coil technology was introduced for low-SAR imaging of patients with DBS implants at 1.5T. In this chapter, the feasibility of advancing the technology to 3T was demonstrated where MRI could render major benefits. For the first time, the possibility of including patients with bilateral leads and fully implanted systems were assessed, which are the most common practices.

5.10.1 Inter-subject variability of implanted lead trajectories and the role of surgical planning

During the past five years, postoperative CT images of more than 120 patients with DBS leads were examined for numerical simulations assessing the SAR. These patients have been operated at three different centers in Massachusetts General Hospital, Albany Medical Center, and Northwestern Memorial Hospital, and by at least four different neurosurgeons. A striking observation was the substantial patient-to-patient variation in the trajectory of extra cranial portion of the leads (see Figure 5.3). Unlike the meticulously planned intracranial trajectory of the electrode, for which

almost every neurosurgeon follows textbook guidelines to determine the entry point on the skull and chose the angle of penetration to the target nuclei, there are no guidelines for the placement of extra cranial portions of the leads. This causes a large variation in lead trajectories depending on surgeons' preference and practice style. In the context of rotating coil technology, such variation poses a problem for the simultaneous reduction of the SAR at tips of bilateral leads, as it can be observed from Figure 5.6. In cases where left and right leads have non-overlapping trajectories, the optimum rotation angle that minimizes the SAR for one lead could be far from optimum for the other lead. A relatively simple surgical modification can address this problem by aligning and overlapping trajectories of left and right leads and extension cables. This chapter demonstrated the first results of such modification implemented in a patient who was implanted with a bilateral lead system. The bilateral SAR Reduction Efficiency (SRE) of the coil was substantially higher for the patient with modified lead trajectories compared to the average in patients who were operated without any specific instruction (95% vs. 59%). An interesting observation was that the SAR generated by the rotating coil at all rotation angles was always lower than the SAR generated by the body coil in the patient with modified DBS trajectories. This is a significant result as it suggests surgical modifications can significantly reduce the risks associates with operational errors when the rotating coil is used on patients. In general, the rotating head coil significantly outperformed the body coil in patients with fully-implanted systems (ID13 and ID14), which was predictable considering a substantial portion of the DBS device will be outside of the head coil's field of view.

5.10.2 Limitations of DBS MRI in clinical settings

Currently, Abbott (Abbott Laboratories, Chicago IL) is the only manufacturer of MR-conditional directional DBS leads that allow for current steering and selective target stimulation for which postoperative fMRI will provide invaluable information on the mechanism of action of stimulation. MRI labeling of Abbott DBS systems limits the $\mathbf{B}_1^+$ to 1.3 μT for fully implanted systems. From Table 5.2, it can be observed that this value is well exceeded in many typical MRI brain exams. For example, running a T2-weighted turbo spin-echo sequence, which is the gold standard protocol for stroke diagnosis, produced a 10.8° temperature rise when the body coil was used, whereas the rotating head coil generated < 1° heating. Other useful but high-SAR sequences

are time of flight angiography and constructive interference in steady-state (CISS) MRI. CISS MRI, in particular, is widely used in the evaluation of the cranial nerves, CSF rhinorrhea and aqueduct stenosis [184]. Both sequences generated > 7° temperature rise in simulations with the body coil and < 0.5° heating when the rotating coil was used at its optimum angle. It is important to note that although the presented simulations were performed using simplified DBS lead models, which do not reflect the actual temperature rise of the commercial device, they still give a fair comparative view of RF heating generated by the MRI body coil and the rotating coil system.

This chapter presents a feasibility study to scale the reconfigurable MRI coil technology for low SAR imaging of DBS patients at 3T. Finite element simulations were performed using patient-derived models of DBS systems with realistic device configurations. Both isolated leads and fully implanted systems were evaluated. A total of 832 simulations were performed to evaluate the SAR reduction performance of a rotating 3T head coil. The results showed a promising SAR reduction efficiency of > 80% for unilateral leads and > 59% for bilateral leads. A simple surgical modification in implantation of DBS leads boosted the coil's SAR reduction efficiency to > 90%, leading to a 15-fold reduction in temperature rise in the tissue during typical MRI exams compared to a CP body coil. The results suggest that the reconfigurable MRI technology offers a promising solution to the problem of RF safety of deep brain stimulation implants at 3T.

Chapter 6

RF Heating of Deep Brain Stimulation Implants during MRI in 1.2T Vertical Scanners versus 1.5T Horizontal Systems: A Simulation Study with Realistic Lead Configurations

6.1 Preface

The content of this chapter has been partially presented at the 2020 42nd Annual International Conference of the IEEE Engineering in Medicine & Biology Society (EMBC) [185] and published in Magnetic Resonance in Medicine [186]. Laleh Golestani Rad, Ergin Atalar, Joshua Rosenow, Behzad Elahi, John Kirsch, Bhumi Bhusal, Jasmine Vu, Bach Thanh Nguyen, Stella Lin contributed to this chapter. I have been involved in the preparation of all the simulation files presented in this chapter, their data extraction, and the analysis and representation of the results.

6.2 Introduction

Deep brain stimulation (DBS) is the neurosurgical procedure of choice for treating several major neurological and psychiatric disorders. It uses an implantable pulse generator (IPG) in the patient's chest to deliver electrical pulses to specific nuclei in

the brain via subcutaneous leads and extensions. DBS was approved as a treatment of Parkinson's disease [187], dystonia [127, 128], essential tremor [124, 125], obsessive-compulsive disorder [131, 132], and epilepsy [133] by the US Food and Drug Administration (FDA). From a strictly clinical point of view, precise 3D localization of DBS leads is a critical issue as they are implanted on the anatomical regions requiring submillimeter-positioning accuracy to enhance therapeutic benefits. Deviation of lead position from the target can cause side effects like migraine, depression, ocular deviation, and muscle contractions [188]. On the other hand, a lack of understanding of the biophysical mechanisms of DBS prohibits the use of DBS in an extensive range of mental disorders. Magnetic resonance imaging (MRI) has a significant capacity to target and localize DBS leads and address unanswered questions regarding DBS mechanisms due to its excellent soft-tissue contrast, non-invasive nature, and the abundance of accessible post-processing MR tools. Unfortunately, MRI is widely inaccessible for DBS patients because of the interaction between RF fields of scanner and DBS leads, causing safety concerns associated with RF heating of implants [138, 139]. The electric field generated by the RF transmit coil induces currents on implanted conductor leads, which raises the energy absorption level in the tissue surrounding the lead tips and subsequently increases the local specific absorption rate (SAR) [189]. In effect, such high energy may cause an excessive increase in temperature and damage to the tissue. Severe damage has highlighted the importance of RF heating as a significant safety issue [190]. Subsequently, the conditions where MRI is recommended for DBS patients are limited to restrict these damages. For instance, according to the latest guidelines, MRI in DBS patients is allowed for only 1.5T horizontal scanners and pulse sequences with highly reduced power (whole-head SAR of < 0.1 W/kg - 30 times lower than the FDA limit, or the RMS of $\mathbf{B}_1^+$ field < 2 μT) are recommended. These restrictions in most clinical applications are well exceeded [24].

To date, the majority of MRI safety studies have been performed on horizontal closed-bore MRI systems. Vertical scanners, originally introduced as low-field open-bore systems, are now available at high field strength capable of high-resolution structural and functional studies. Generally, vertical MRI systems generate a fundamentally different distribution of electric and magnetic fields inside patient's bodies because of their 90° rotated RF coils. As the orientation and phase of MRI incident electric field along the trajectory of an elongated implant has a substantial

effect on the local SAR at the electrode tips [45, 139, 146, 163, 164, 191, 192], it was hypothesized that vertical scanners generate a statistically different RF heating compared to horizontal systems. The hypothesis is based on a preliminary study of RF heating analysis of DBS patients in a commercially available vertical open-bore 1.2T MRI scanner (OASIS, Hitachi Healthcare Americas, OH USA) [186]. In this study, numerical simulations were conducted in a 1.2T vertical coil and a 1.5T horizontal coil to compare the SAR amplification around the electrode tips of DBS leads. Three patient-derived models of bilateral DBS systems were involved in the simulations. The results of this study showed a 4- to 14-fold reduction in the maximum local SAR implication around the electrode tips of the DBS leads in the vertical coil in comparison with the horizontal coil.

Throughout this chapter, the previous work in Ref. [186] is extended to investigate a lager patient-derived DBS lead cohort to confirm that the commercial vertical 1.2T coil heats up the electrode tips less than the conventional horizontal 1.5T coil. This extension is accomplished by electromagnetic simulations of 90 DBS lead models with realistic trajectories registered in a homogeneous human model constructed by image segmentation of postoperative computed tomography (CT) data of each patient. To investigate the effect of rigid-body movements or position shifts on the induced electromagnetic field across the patient models and know whether the reduction of SAR implication is only specific to one specimen, all DBS patients simulated in two different positions respect to the coils isocenter.

6.3 Methods

6.3.1 RF coil models

Numerical models of a 1.2T high-pass radial planar birdcage coil made of 12 vertical rungs and a 1.5T high-pass birdcage coil consisting of 16 horizontal rungs were constructed and tuned to their respective Larmor frequencies (i.e., 50.35 MHz for 1.2T proton imaging and 64 MHz for 1.5T) in the simulation environment. The vertical coil was modeled in line with the commercial RF coil (Oasis, Hitachi Healthcare) described in Ochi et al. [193]. Figure 6.1 shows the geometrical details of both coil models and Figure 6.2 shows their $\mathbf{B}_1^+$ and $\mathbf{E}$ fields destructions within a human body model with no implant. Horizontal coil dimensions were chosen similar to those

reported in the literature [167]. The vertical coil was derived by four feeding ports arranged in the upper and lower segments, based on information provided by the manufacturer. Both coils were derived in the quadrature excitation mode by feeding their ports with the same amplitudes and different phases, as shown in Figure 6.2. There are two main differences between the 1.2T OASIS coil and the 1.5T birdcage coil; first, they have fundamentally different field orientations, and second, they have different resonance frequencies. To distinguish the effects of field increases and changes in field orientation on the results, a 1.2T horizontal birdcage coil with the same physical dimensions of the 1.5T birdcage coil (shown in Figure 6.1B) returned at 50.35 MHz.

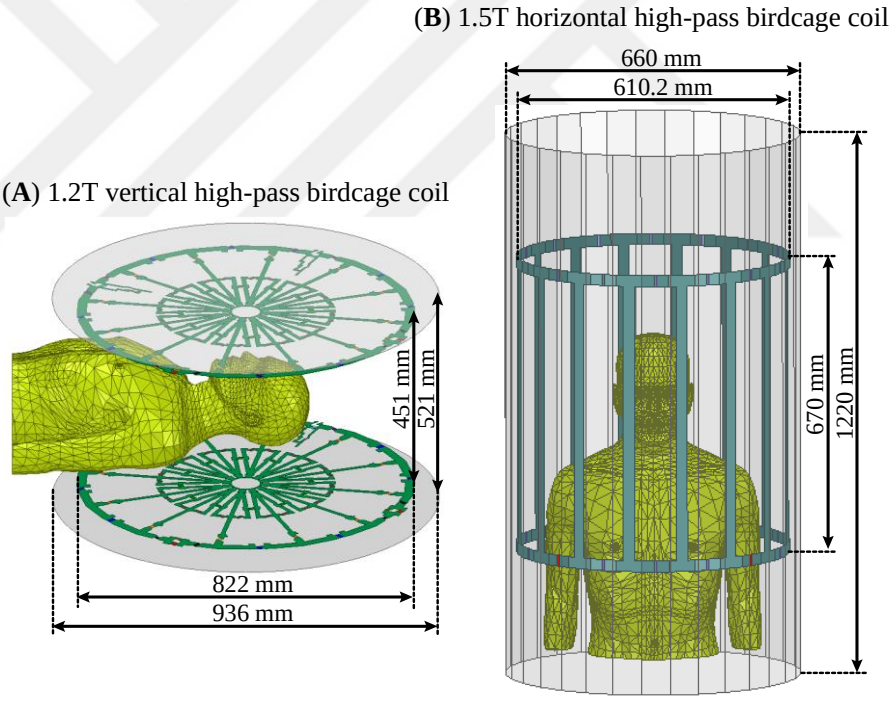

FIGURE 6.1 - Geometry configuration of (A) 1.2T high-pass radial planar birdcage coil and (B) 1.5T high-pass birdcage coil.

The body model is placed in two different positions to evaluate the effect of rigid-body movements or position shifts on the induced electromagnetic field across the group of patient models (Figure 6.3). In the first case, the human model was centered by placing the nose at the isocenter of the coils (denoted as "head landmark"), and in the second case, the human model was centered by placing the center of the chest at the isocenter (denoted as "chest landmark").

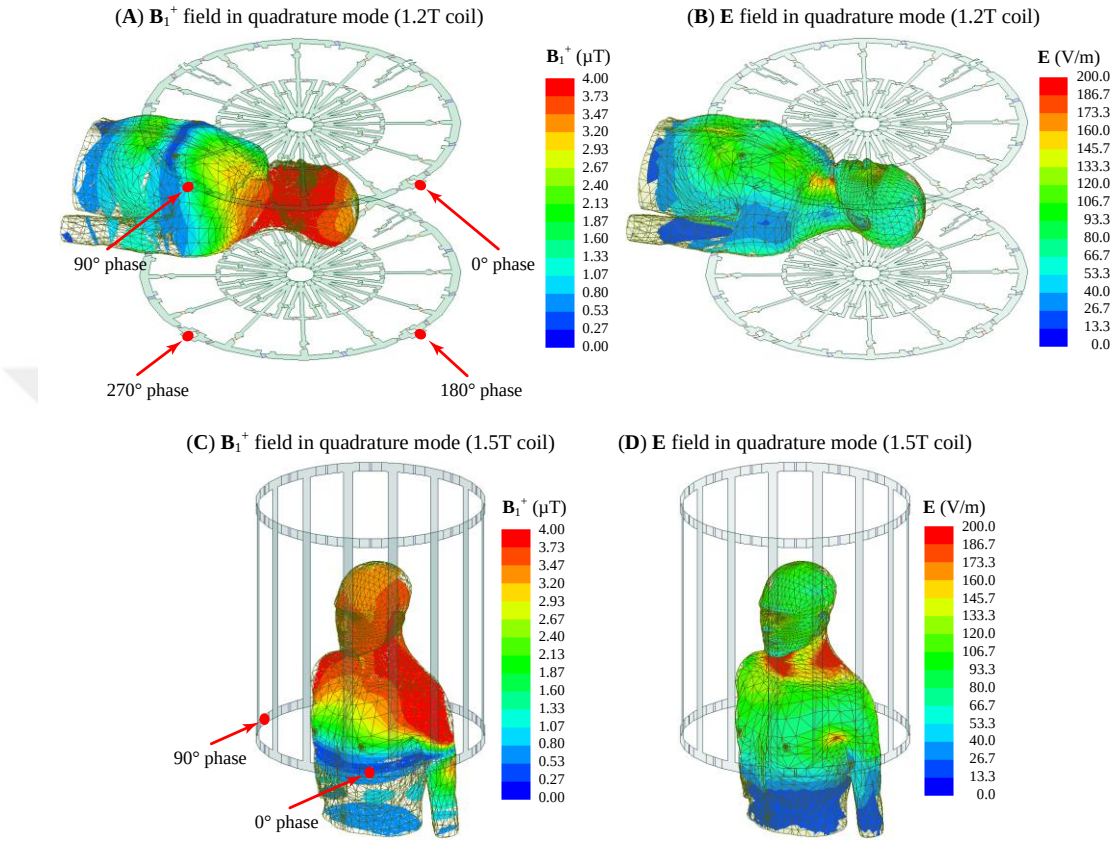

FIGURE 6.2 - $\mathbf{B}_1^+$ and **E** fields distributions of (A-B) 1.2T vertical coil and (C-D) 1.5T horizontal coil within a human body model with no implants. Both coils' input power is adjusted to generate a mean $\mathbf{B}_1^+ = 4$ μT over a circular plane placed on an axial plane passing through the coils' iso-center.

6.3.2 Patient-derived DBS lead models and numerical simulations

In this chapter, 90 DBS lead models were simulated with realistic trajectories based on postoperative computed tomography (CT) images from 37 patients with bilateral DBS leads (ID1-ID32 and ID47-ID51) and 16 patients with unilateral DBS leads (ID33-ID46 and ID52-ID53). Northwestern University's ethics review board approved the prospective use of imaging data for simulation modeling for the first twenty patients (ID1-ID20, Figure 6.4). On the other hand, the use of image data from other patients (ID21-ID53, Figures 6.5-6.6) was approved by Albany Medical College's institutional review board. The 3D implant models were constructed utilizing a similar process outlined in Refs. [18, 44, 191]. The implant details, as used in numerical

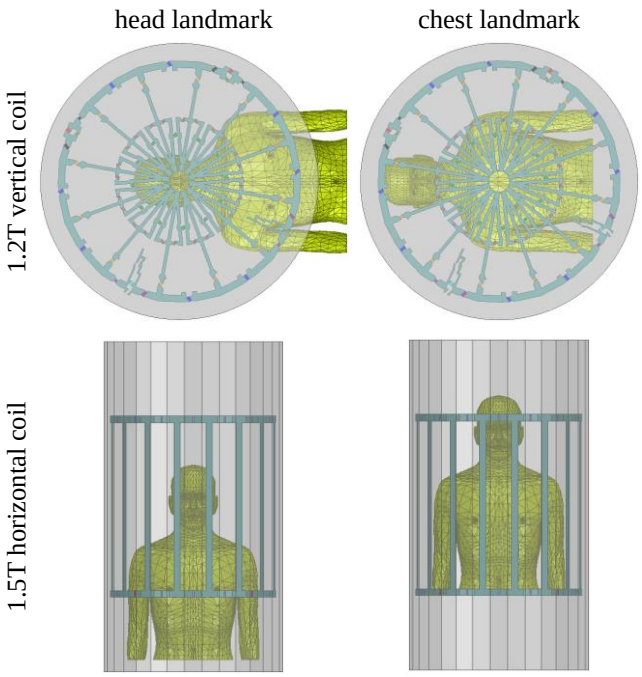

FIGURE 6.3 - Coil configuration of 1.2T vertical and 1.5T horizontal coils loaded with a human body model placed at two different positions corresponding to head and chest imaging.

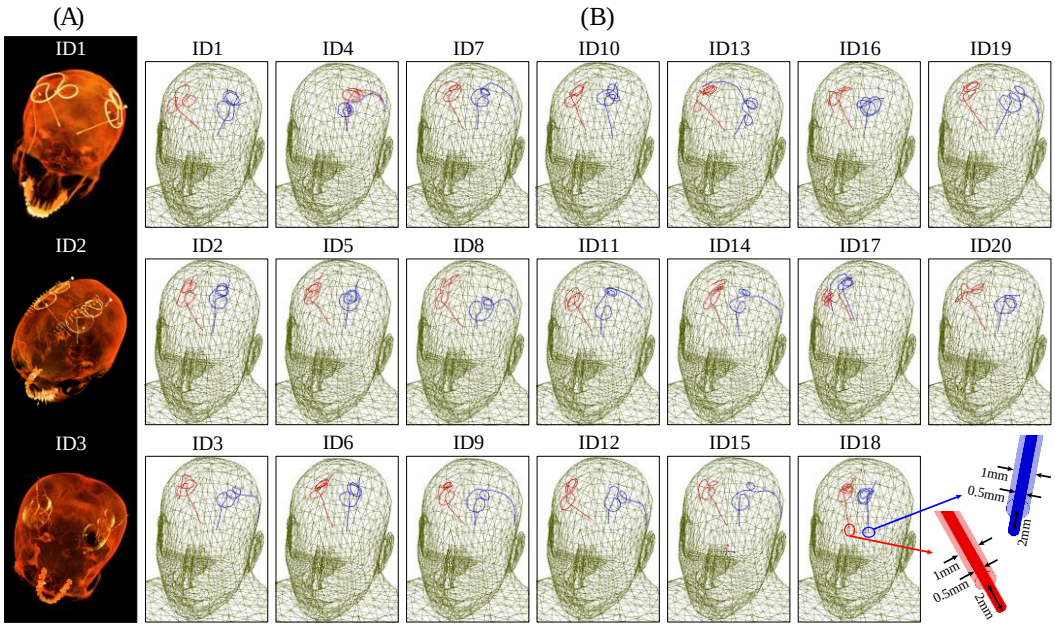

FIGURE 6.4 – (A) Examples of postoperative CT images of three patients (patient numbers ID1-ID3). (B) Reconstructed models of isolated DBS leads with approval form Northwestern University's ethics review board. Lead trajectories were extracted using CT images of 20 patients with bilateral DBS implantation (patient numbers ID1-ID20) and were registered in a homogeneous body phantom for electromagnetic simulations.

simulations, are shown in Figure 6.4. Each lead was modeled as a solid straight

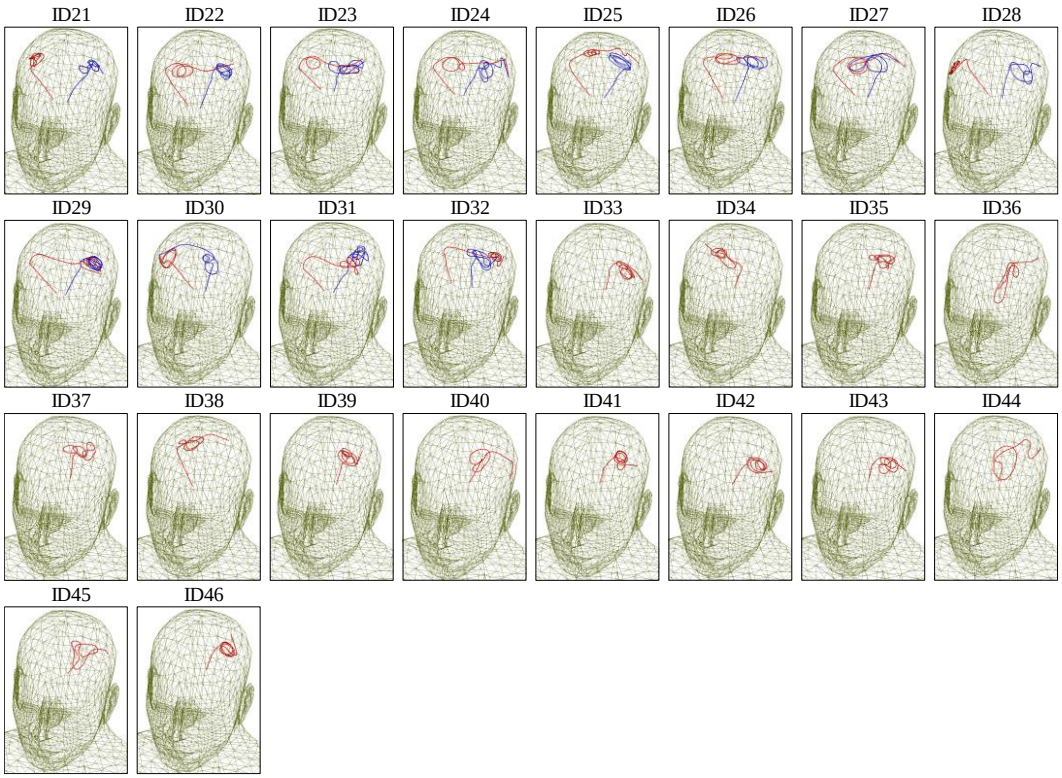

FIGURE 6.5 - Reconstructed models of isolated DBS leads with approval from Albany Medical College's institutional review board. Lead trajectories were extracted using CT images of 12 patients with bilateral DBS implantation (ID21-ID32) and 14 patients with unilateral DBS implantation (ID33-ID46) were all registered to a standard homogeneous head and torso model.

platinum-iridium (Pt:Ir) core (diameter = 0.5 mm, $\sigma = 4\times10^6$ S/m) embedded into a urethane insulation (diameter = 1 mm, $\varepsilon_r = 3.5$) with a 2 mm exposed tip. The reconstructed DBS implant models of 46 patients (ID1-ID46) had isolated leads that were not connected to any IPG and registered to a standard homogeneous head and torso model ($\sigma = 0.47$ S/m, $\varepsilon_r = 80$). In contrast, 7 patients (ID47-ID53, Figure 6.6) had a fully implanted DBS system connected to IPG. In these patients, lead trajectories were registered in the patients' corresponding homogeneous body models, all with a conductivity of 0.47 S/m and s relative permittivity of 80.

All simulations were implemented in ANSYS Electronics Desktop 19.2 (ANSYS Inc., Canonsburg, PA). For each simulation, the input power of coils was adjusted to produce a mean $\mathbf{B}_1^+ = 4$ μT over a circular plane with a diameter of 48 mm positioned inside the body model on an axial plane passing through the coil's iso-center. The

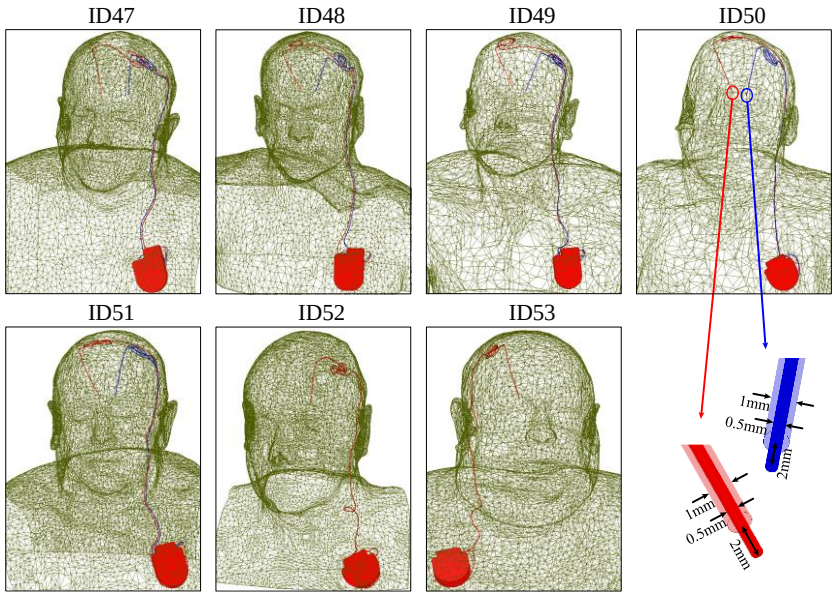

FIGURE 6.6 - Reconstructed models of fully implanted DBS systems. Lead trajectories were extracted using CT images of 5 patients with bilateral DBS implantation (ID47-ID51) and two patients with unilateral DBS implantation (ID52-ID53) were all registered in their corresponding homogeneous body models for electromagnetic simulations.

induced electromagnetic field in the patient models caused by each coil was computed using a combined numerical method and circuit analysis approach based on ANSYS Electronics [44, 46, 47, 76, 164, 191]. The maximum of 0.1g-averaged SAR (0.1g-SAR_{max}) was calculated inside a cubic volume of $20 \times 20 \times 20$ mm^3 surrounding the tip of the lead. HFSS built-in SAR calculator module that implements the IEEE STD P1528.4 recommendation was used for 0.1g-averaged SAR assessments [66]. At the beginning of each simulation, triangle edge lengths on the coils, lumped ports, and shields, respectively, were restricted to < 5 mm, < 1 mm, and < 25 mm. Within the body volume, the tetrahedron edge lengths were restricted to < 35 mm, with the exception of the cubic volumes surrounding both implant tips, which enforced edge lengths to be less than 1 mm. Also, the triangle edge lengths on the surface of all electrodes and their insulations were set to be < 0.5 mm. Mesh operations were refined the initial meshing iteratively until the scattering parameters were converged (3% convergence tolerance). Upon numerical convergence, the computing space and time for each simulation of the vertical and horizontal coils on a Dell PowerEdge R740xd system with 1.5 TB RAM and two Intel(R) Xenon(R) Gold 6140 CPUs (2.3 GHz, 36 cores) were summarized in Table 6.1.

TABLE 6.1 - Computation space and time for each simulation of the OASIS coil and horizontal birdcage coil.

Coil type	Field strength	DBS system type		Tetrahedral meshes	Simulation time	Simulation size
OASIS	1.2T	Unilateral	Isolated system	~ 3.9×10^6	~ 11 h	~ 160 GB
			Full system	~ 4.6×10^6	~ 12 h	~ 185 GB
		Bilateral	Isolated system	~ 4.8×10^6	~ 14 h	~ 195 GB
			Full system	~ 5.9×10^6	~ 16 h	~ 240 GB
Horizontal Birdcage	1.2T	Unilateral	Isolated system	~ 3.0×10^6	~ 4 h	~ 30 GB
			Full system	~ 4.1×10^6	~ 8 h	~ 65 GB
		Bilateral	Isolated system	~ 4.1×10^6	~ 6 h	~ 40 GB
			Full system	~ 5.1×10^6	~ 11 h	~ 100 GB
Horizontal Birdcage	1.5T	Unilateral	Isolated system	~ 3.0×10^6	~ 4 h	~ 30 GB
			Full system	~ 4.1×10^6	~ 8 h	~ 65 GB
		Bilateral	Isolated system	~ 4.1×10^6	~ 6 h	~ 40 GB
			Full system	~ 5.1×10^6	~ 11 h	~ 100 GB

6.4 Results

Figure 6.7 shows the distribution of local SAR for one of the patients who showed a very high value of 0.1g-SAR_{max} among other patients (ID47), for the vertical coil at 1.2T and the horizontal coils at 1.2T and 1.5T for both imaging landmarks. The local SAR maps are shown on an axial plane passing through the electrode tips. For the head (chest) landmark, the 0.1g-SAR_{max} around the tips of left and right leads were reduced by 32-fold (31-fold) and 130-fold (131-fold), respectively, in the OASIS coil compared to the horizontal coil at 1.5T. Moreover, the OASIS coil reduced the 0.1g-SAR_{max} around the tips of left and right leads by 33-fold (33-fold) and 184-fold (112-fold), respectively, compared to the 1.2T horizontal coil for the head (chest) landmark.

Figure 6.8 depicts the box plot of the 0.1g-SAR_{max} over all 90 lead models. This plot shows the median value and interquartile range (IQR) of 0.1g-SAR_{max} for the 1.2T vertical OASIS coil and 1.2T and 1.5T horizontal birdcage coils with two different landmarks. The outliers were plotted individually using a red '+' symbol. For the head landmark, the 0.1g-SAR_{max} was 17±26.8 W/kg for the 1.2T OASIS vertical coil and 519.3±694.6 W/kg for the 1.5T horizontal birdcage coil. At the chest landmark, the 0.1g-SAR_{max} was 10.2±35.5 W/kg for the 1.2T OASIS coil and 268.3±671.5 W/kg for the 1.5T birdcage coil. A paired two-tail t-test showed a significant reduction in SAR with a large effect-size during head MRI ($p < 7.7\times10^{-10}$, Cohen's d = 1.02) as well as

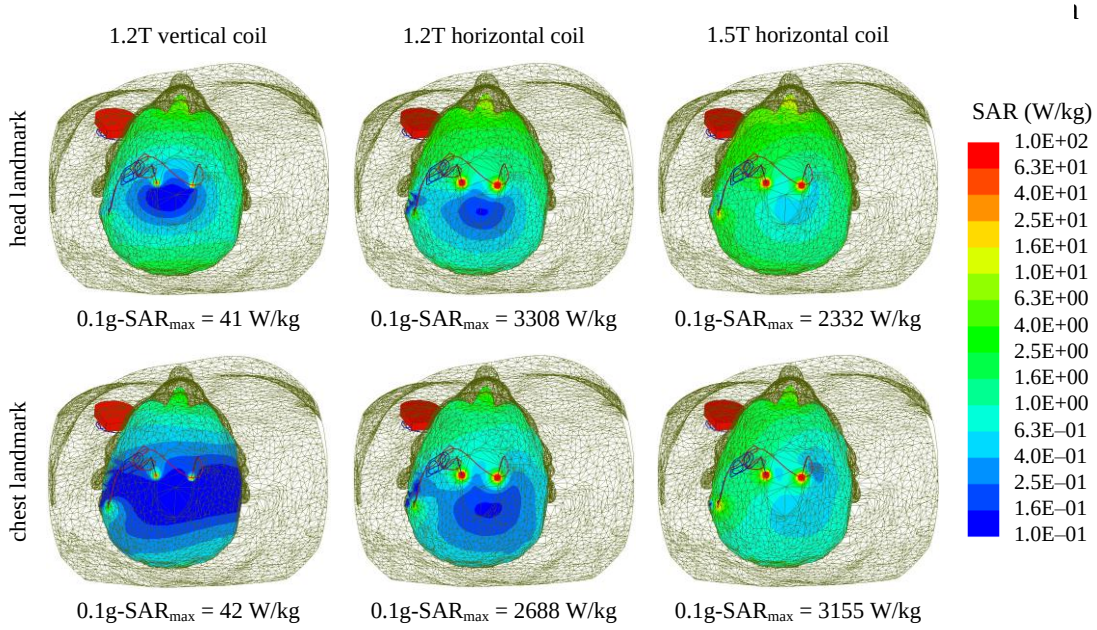

FIGURE 6.7 - Local SAR distributions in patient 47 (ID47) for the 1.2T OASIS coil and 1.2T and 1.5T horizontal birdcage coils all with head and chest landmarks on an axial plane that passes through the tips of implants. In all maps, the coil's input power is adjusted to generate a mean $\mathbf{B_1}^+ = 4$ μT over a circular plane placed on an axial plane passing through the coil's iso-center.

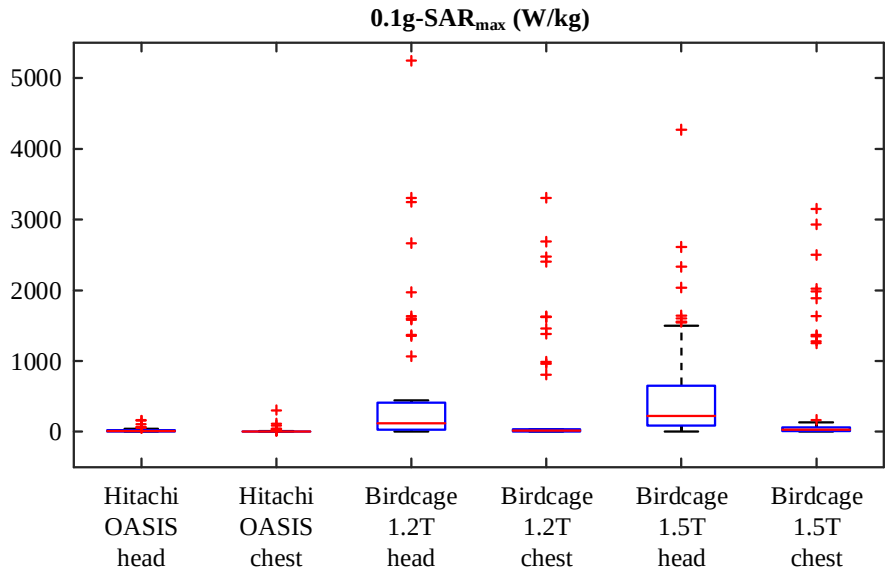

FIGURE 6.8 - Local 0.1g-SAR_{max} over 90 leads shown for the 1.2T vertical coil and 1.2T and 1.5T horizontal coils for head and chest landmarks. Box and whisker plot are showing data range, median, and interquartile range (IQR). The outliers were plotted individually using a red '+' symbol.

standard 1.5T birdcage coil. Besides, for the 1.2T horizontal birdcage coil, the 0.1g-SAR_{max} was 608.9±1077.1 W/kg and 411.2±836.9 W/kg, respectively, for the head and chest landmarks. More details on the median values and interquartile ranges (IQR) of 0.1g-SAR_{max} for different coils with head can chest landmarks are provided in Table 6.2.

TABLE 6.2 - Maximum of 0.1g SAR

Coil type	Field strength	Body landmark	Median (W/kg)	IQR (W/kg)	Mean (W/kg)	SD (W/kg)
OASIS	1.2T	Head	8.6	15.4	17	26.8
		Chest	2	3.8	10.2	35.5
Horizontal Birdcage	1.2T	Head	122.4	372.2	608.9	1077.1
		Chest	12.4	31.5	411.2	836.9
Horizontal Birdcage	1.5T	Head	223.7	568.4	519.3	694.6
		Chest	28.9	49.3	268.3	671.5

6.5 Discussion and conclusion

Over the past decade, DBS has evolved into a remarkable treatment for a variety of mental and neurological disorders. MRI is extremely useful in patients with DBS implants both for electrode localization and ruling out complications, and for evaluating the stimulation's therapeutic effects. The key impediment for these patients to benefit from MRI is the RF heating due to the interaction between RF fields of the MR scanner and DBS leads and extensions. However, this issue is a complicated multi-varying problem in MRI environments involving a numerous of interplaying factors which include the implant's configuration and position in the body [161, 194, 195], the patient's anatomy and position in the RF coil [164, 196, 197], and the orientation and phase of the incident electric field [45, 46, 146, 198]. Recent years have witnessed a spike in attempts to mitigate the problem of MRI-induced implant heating. In recent years, attempts to minimize the MRI-induced implant heating issue have been increasing. Most of these studies have focused on geometry, structure, or material modifications of implants [38, 52, 58, 59, 61, 115, 182, 183, 199, 200]. Despite a large number of researches over the last two decades, RF heating remains a significant issue for DBS patients and cannot be addressed exclusively by device manufacturers. Therefore, a number of groups focused on the modification of MRI hardware to limit localized heating levels through shaping and manipulating the spatial distribution of the RF electric field. Recent techniques are based on parallel RF

transmission strategies [18, 22, 23, 43-45], and reconfigurable MRI technology [24, 25, 45-47, 201].

Open MRI scanners typically utilize magnets with vertical fields, since they provide a convenient platform to carry out interventional studies. The existing literature on MRI RF safety, as well as MR-labeling of DBS devices, are limited to horizontal closed-bore MRI scanners. Vertical MRI systems, which produce a substantially different distribution of magnetic and electric fields, have not been studied in the context of RF heating of implants. Recently, the first simulation study of RF heating analysis of three patients implanted bilaterally with realistic DBS lead configurations in a commercially available vertical open-bore 1.2T MRI scanner was presented, and the SAR amplification around the electrode tips of DBS leads with a conventional horizontal closed-bore 1.5T MRI scanner was compared [186]. It was observed a 4- to 14-fold decrease in the maximum local SAR implication around the electrode tips of the DBS implants in the vertical coil in comparison with the horizontal coil.

This chapter presents a finite element electromagnetic simulation study of DBS device RF heating a relatively large sample (N = 90) of patient-derived realistic lead models to verify the preliminary results that were found in Ref. [186]. Simulations were performed on a commercial vertical 1.2T coil and a conventional horizontal 1.5T coil, loaded by a homogeneous human body model implanted with DBS lead models. To explore the impact of rigid-body movements or location shifts on the coupled field along with the implants and to determine whether the SAR reduction is only unique to a single position, all simulations were conducted in two different body positions with respect to the coils isocenter, labeled as head and chest landmarks. As the resonance frequencies and field orientations of the 1.2T OASIS coil and the 1.5T birdcage coil are fundamentally different, the DBS patients were tested with a 1.2T horizontal birdcage coil to distinguish the effects of field increases and changes in field orientation on the results. On average, the results showed that 0.1g-averaged SAR was reduced by 31-fold for head imaging and by 26-fold for chest imaging in MRI with a 1.2T vertical coil compared to a standard 1.5T horizontal body coil. It was also observed that for the head (chest) landmark, the 1.2T OASIS vertical coil, on average, decreased 0.1g-averaged SAR by 36-fold (40-fold) compared to the 1.2T horizontal birdcage coil. Interestingly, vertical scanners were initially being developed to facilitate open access to patients and, thus, provide an ideal platform for image-guided

DBS surgery. These results, if verified in experiments, can open the door to a plethora of MRI applications to guide and interpret DBS therapy.

Chapter 7

Summary and Conclusions

In this dissertation, a variety of innovative techniques towards designing transmit array (TxArray) coils and mitigating radiofrequency (RF) heating of implanted patients during MRI were studied. Here, the dissertation is concluded by providing a summary of the contributions.

The first contribution of this dissertation was on the eigenmode analysis of the scattering (**S**) matrix for the design of MRI transmit array (TxArray) coils. This contribution is proposed to obtain efficient operation modes of TxArray coils. Then, the concept of modal reflected power and excitation eigenmodes, which are calculated as the eigenvalues and eigenvectors of $\mathbf{S}^{\mathbf{H}}\mathbf{S}$-matrix, were introduced. The normalized reflected power, which is the ratio of the total reflected power to the total incident power of TxArray coils for a given excitation signal, was formulated as the weighted sum of the modal reflected power. By minimizing the modal reflected power of TxArray coils, the excitation space with a low total reflection was increased. The algorithm was tested on four dual-row 3T TxArray coils with 8-32 channels. By minimizing the modal reflected power, an 8-element TxArray coil was designed to have a low reflection for 7 out of 8 dimensions of the excitation space. Similarly, the minimization of the modal reflected power of a 16-element TxArray coil provided the opportunity to enlarge the dimension of the excitation space by 50% compared with commonly employed design techniques. Moreover, it demonstrated that the low total reflected power for some critical excitation modes, such as the circularly polarized (CP) mode, can be achieved for all TxArray coils even with a high level of coupling. The finding of this study demonstrated that the eigenmode analysis is an efficient

method that intuitively provides a quantitative and compact representation of the coil's power transmission capabilities. This method also provided an insight into the excitation modes with low reflection and the required number of transmit elements to achieve efficient RF shimming in terms of power consumption. In addition, it offered a simple tool for quantifying, comparing, and optimizing the performance of TxArray coils.

The second contribution of this dissertation was on the development of a fast fine-tuning technique that could be used in the design process of manufactured TxArray coils. This contribution proposed an approach for designing TxArray coil precisely by integrating the fabricated coil's equivalent circuit model and its simulation results to reduce measurement and simulation differences caused by the imperfection in manufacturing. The performance of the proposed fine-tuning method was investigated on an 8-element 3T TxArray coil. The coil was simulated and appropriately designed at 123.2 MHz ($|s_{nn}| \leq$ -23 dB and $|s_{mn}| \leq$ -11 dB) and then constructed by assembling the optimum capacitor values obtained from the simulation. After measuring **S**-matrix as a function of frequency and fitting them to the coil's equivalent circuit model, all self/mutual-inductances and self/mutual-resistances of the manufactured coil were estimated. The capacitor values were recalculated based on this circuit model by minimizing the modal reflected power of the coil. The experimental results showed the resonances of the coil elements were at least 7 MHz higher than the desired resonance frequency because of the imperfections in the manufacturing process. The coil's **S**-matrix was then measured to predict all inductances and resistances accurately. Finally, the finely-tuned capacitor values were calculated and mounted on the coil. The **S**-matrix of the fine-tune coil ($|s_{nn}| \leq$ -15 dB and $|s_{mn}| \leq$ -9 dB) did not need a second iteration. The maximum error between the calculated and measured **S**-matrix was calculated as -7 dB. The finding of this study showed that considering the exact manufactured structure of TxArray coils may reduce the error between the simulation and measurement results and substantially accelerate the fine-tuning process.

The third contribution of this dissertation was on the theoretical optimization of a TxArray coil for minimum coupling. This contribution introduced a methodology to minimize the magnetic coupling between non-adjacent transmit channels of a TxArray coil by optimizing some of its physical parameters. The method was based on calculating all self/mutual-inductances and then minimizing the mutual-inductances

normalized by the self-inductances. Accordingly, the proposed method was used to determine the optimum radius, length in the longitudinal direction, the width of end-rings, and the width of rungs of a 3T shielded 12-element head degenerate birdcage TxArray coil with capacitive decoupled loops. The optimization showed that the coil radius and end-rings width should increase to reduce the coupling level. In contrast, the coil length and the width of the rungs should decrease. This study's findings revealed that a sufficient coil distance from the shield should maintain to increase the coil's $\mathbf{B}_1^+$ efficiency. Finite element electromagnetic simulation results confirmed the validity of the proposed method in determining the coil's optimal sizes.

The fourth contribution of this dissertation was on evaluating specific absorption rate (SAR) reduction performance at tips of bilateral deep brain stimulation (DBS) implants during MRI at 3T using a recently introduced reconfigurable MRI coil technology, which uses a mechanically rotating linearly polarized birdcage transmitter. Patient-derived realistic models of bilateral DBS leads both in isolation and fully implanted DBS systems were developed from postoperative CT images of 13 patients and finite element simulations were performed to calculate SAR amplification at electrode contacts during MRI with a reconfigurable rotating coil at 3T. Compared to a conventional quadrature body coil, the reconfigurable coil system reduced the SAR on average by 83% for unilateral leads and by 59% for bilateral leads. A simple surgical modification in the trajectory of implanted leads was demonstrated to increase the SAR reduction efficiency of the rotating coil to > 90% in a patient with a fully implanted bilateral DBS system. Thermal analysis of temperature-rise around electrode contacts during typical brain exams showed a 15-fold heating reduction using the rotating coil, generating < 1°C temperature rise during ~ 4-minute imaging with high-SAR sequences where a conventional CP coil generated > 10°C temperature rise in the tissue for the same flip angle.

The last contribution of this dissertation was on the RF heating assessment of DBS implants with realistic lead configurations during MRI in 1.2T vertical scanners versus 1.5T horizontal systems. To date, all MR labeling of conductive implants and the entirety of studies on the RF heating analysis of DBS implants are restricted to horizontal close-bore MRI scanners. However, vertical open-bore MRI scanners are becoming accessible at 1.2T with the ability to produce high resolution structural and functional images. Therefore, this contribution presented a simulation analysis of RF

heating in a large cohort of DBS patients in vertical scanners, which have a significantly different distribution of electromagnetic fields. A commercially available vertical open-bore 1.2T coil and a standard horizontal closed-bore 1.5T coil were simulated to compare the local SAR amplification surrounding the tips of DBS leads. Simulations were performed at two major imaging landmarks representing head and chest imaging. On average, 0.1g-averaged SAR was reduced by 31-fold for head imaging and by 26-fold for chest imaging in MRI with a 1.2T vertical coil compared to a standard 1.5T horizontal body coil. This contribution's findings will open up the doors to a variety of MRI applications to interpret and facilitate DBS therapy.

Bibliography

[1] C. K. Kuhl, H. Kooijman, J. Gieseke, and H. H. Schild, "Effect of B-1 inhomogeneity on breast imaging at 3.0 T," *Radiology,* vol. 244, no. 3, pp. 929-930, Sep 2007.

[2] C. Geppert, J. Nistler, W. Renz, I. Panagiotelis, and T. Speckner, "Reduced B1-inhomogeneities in breast MRI using optimized RF excitation," *In Proceedings of the 16th Annual Meeting of ISMRM, Toronto, Canada, Abstract 2726,* 2008.

[3] Z. W. Wang, J. C. Lin, W. H. Mao, W. Z. Liu, M. B. Smith, and C. M. Collins, "SAR and temperature: Simulations and comparison to regulatory limits for MRI," *Journal of Magnetic Resonance Imaging,* vol. 26, no. 2, pp. 437-441, Aug 2007.

[4] J. Nadobny, M. SArntenings, D. Diehl, E. Stetter, G. Brinker, and P. Wust, "Evaluation of MR-induced hot spots for different temporal SAR modes using a time-dependent finite difference method with explicit temperature gradient treatment," *IEEE Transactions on Biomedical Engineering,* vol. 54, no. 10, pp. 1837-1850, Oct 2007.

[5] G. Adriany *et al.*, "Transmit and receive transmission line arrays for 7 tesla parallel imaging," *Magnetic Resonance in Medicine,* vol. 53, no. 2, pp. 434-445, Feb 2005.

[6] G. Adriany *et al.*, "A 32-Channel Lattice Transmission Line Array for Parallel Transmit and Receive MRI at 7 Tesla," *Magnetic Resonance in Medicine,* vol. 63, no. 6, pp. 1478-1485, Jun 2010.

[7] S. H. G. Rietsch, S. Orzada, A. K. Bitz, M. Gratz, M. E. Ladd, and H. H. Quick, "Parallel transmit capability of various RF transmit elements and arrays at 7T MRI," *Magnetic Resonance in Medicine,* vol. 79, no. 2, pp. 1116-1126, Feb 2018.

[8] N. I. Avdievich *et al.*, "Evaluation of transmit efficiency and SAR for a tight fit transceiver human head phased array at 9.4 T," *NMR in Biomedicine,* vol. 30, no. 2, Feb 2017.

[9] A. Sadeghi-Tarakameh *et al.*, "In vivo human head MRI at 10.5T: A radiofrequency safety study and preliminary imaging results," *Magnetic Resonance in Medicine,* Nov 21 2019.

[10] A. Sadeghi-Tarakameh *et al.*, "Improving radiofrequency power and specific absorption rate management with bumped transmit elements in ultra-high field MRI," *Magnetic Resonance in Medicine,* Jun 23 2020.

[11] A. Sadeghi-Tarakameh *et al.*, "Optimizing the topography of transmit coils for SAR management," *In Proceedings of the 26th Annual Meeting of ISMRM-ESMRMB, Paris, France, Abstract 0297,* 2018.

[12] A. Sadeghi-Tarakameh *et al.*, "A New Coil Element for Highly-Dense Transmit Arrays: An Introduction to Non-Uniform Dielectric Substrate (NODES) Antenna," *In Proceedings of the 27th Annual Meeting of ISMRM, Montreal, Canada, Abstract 0732,* 2019.

[13] Z. H. Zhang, C. Y. Yip, W. Grissom, D. C. Noll, F. E. Boada, and V. A. Stenger, "Reduction of transmitter B-1 inhomogeneity with transmit SENSE slice-select pulses," *Magnetic Resonance in Medicine,* vol. 57, no. 5, pp. 842-847, May 2007.

[14] R. Schneider, F. Boada, J. Haueisen, and J. Pfeuffer, "Automated Slice-Specific Simultaneous Z-Shim Method for Reducing B1 Inhomogeneity and Susceptibility-Induced Signal Loss with Parallel Transmission at 3T," *Magnetic Resonance in Medicine,* vol. 74, no. 4, pp. 934-944, Oct 2015.

[15] K. Setsompop *et al.*, "Parallel RF transmission with eight channels at 3 Tesla," *Magnetic Resonance in Medicine,* vol. 56, no. 5, pp. 1163-1171, Nov 2006.

[16] C. A. T. Van den Berg *et al.*, "Simultaneous B-1(+) homogenization and specific absorption rate hotspot suppression using a magnetic resonance phased array transmit coil," *Magnetic Resonance in Medicine,* vol. 57, no. 3, pp. 577-586, Mar 2007.

[17] U. Katscher and P. Bornert, "Parallel RF transmission in MRI," *NMR in Biomedicine,* vol. 19, no. 3, pp. 393-400, May 2006.

[18] C. E. McElcheran *et al.*, "Numerical Simulations of Realistic Lead Trajectories and an Experimental Verification Support the Efficacy of Parallel Radiofrequency Transmission to Reduce Heating of Deep Brain Stimulation Implants during MRI," *Scientific Reports,* vol. 9, no. 1, p. 2124, 2019.

[19] A. S. Childs, S. J. Malik, D. P. O'Regan, and J. V. Hajnal, "Impact of number of channels on RF shimming at 3T," *Magnetic Resonance Materials in Physics Biology and Medicine,* vol. 26, no. 4, pp. 401-410, Aug 2013.

[20] M. Kozlov and R. Turner, "Analysis of RF transmit performance for a multi-row multi-channel MRI loop array at 300 and 400 MHz," *Asia-Pacific Microwave Conference 2011,* pp. 1190-1193, 2011.

[21] B. Guerin *et al.*, "Comparison of Simulated Parallel Transmit Body Arrays at 3 T Using Excitation Uniformity, Global SAR, Local SAR, and Power Efficiency Metrics," *Magnetic Resonance in Medicine,* vol. 73, no. 3, pp. 1137-1150, Mar 2015.

[22] Y. Eryaman *et al.*, "Parallel transmit pulse design for patients with deep brain stimulation implants," *Magnetic Resonance in Medicine,* vol. 73, no. 5, pp. 1896-1903, 2015.

[23] B. Guerin, L. M. Angelone, D. Dougherty, and L. L. Wald, "Parallel transmission to reduce absorbed power around deep brain stimulation devices in MRI: Impact of number and arrangement of transmit channels," *Magnetic Resonance in Medicine,* Aug 7 2019.

[24] E. Kazemivalipour *et al.*, "Reconfigurable MRI technology for low-SAR imaging of deep brain stimulation at 3T: Application in bilateral leads, fully-implanted systems, and surgically modified lead trajectories," *Neuroimage,* vol. 199, pp. 18-29, Oct 1 2019.

[25] L. Golestanirad *et al.*, "Reconfigurable MRI coil technology can substantially reduce RF heating of deep brain stimulation implants: First in-vitro study of RF heating reduction in bilateral DBS leads at 1.5 T," *PLoS One,* vol. 14, no. 8, Aug 7 2019.

[26] D. I. Hoult, "The principle of reciprocity in signal strength calculations - A mathematical guide," *Concepts in Magnetic Resonance,* vol. 12, no. 4, pp. 173-187, 2000.

[27] X. Z. Zhang and A. Webb, "Design of a capacitively decoupled transmit/receive NMR phased array for high field microscopy at 14.1 T," *Journal of Magnetic Resonance,* vol. 170, no. 1, pp. 149-155, Sep 2004.

[28] B. Wu, X. L. Zhang, P. Qu, and G. X. Shen, "Design of an inductively decoupled microstrip array at 9.4 T," *Journal of Magnetic Resonance,* vol. 182, no. 1, pp. 126-132, Sep 2006.

[29] A. Sadeghi-Tarakameh, E. Kazemivalipour, T. Demir, U. Gundogdu, and E. Atalar, "Accelerating the CoSimulation Method for Fast Design of Transmit Array Coils: An Example Study on a Degenerate Birdcage Coil," *In Proceedings of the 26th Annual Meeting of ISMRM-ESMRMB, Paris, France, Abstract 4404,* 2018.

[30] A. Sadeghi-Tarakameh, E. Kazemivalipour, T. Demir, U. Gundogdu, and E. Atalar, "Design of a Degenerate Birdcage Radiofrequency Transmit Array Coil for the Magnetic Resonance Imaging Using Equivalent Circuit Model," *In Proceedings of the 34th Annual Scientific Meeting of ESMRMB, Barcelona, Spain,* pp. 300-301, 2017.

[31] P. B. Roemer, W. A. Edelstein, C. E. Hayes, S. P. Souza, and O. M. Mueller, "The Nmr Phased-Array," *Magnetic Resonance in Medicine,* vol. 16, no. 2, pp. 192-225, Nov 1990.

[32] B. Keil *et al.*, "Size-optimized 32-Channel Brain Arrays for 3 T Pediatric Imaging," *Magnetic Resonance in Medicine,* vol. 66, no. 6, pp. 1777-1787, Dec 2011.

[33] N. I. Avdievich, A. Pfrommer, I. A. Giapitzakis, and A. Henning, "Analytical modeling provides new insight into complex mutual coupling between surface loops at ultrahigh fields," *NMR in Biomedicine,* vol. 30, no. 10, Oct 2017.

[34] X. Q. Yan, J. C. Gore, and W. A. Grissom, "New resonator geometries for ICE decoupling of loop arrays," *Journal of Magnetic Resonance,* vol. 277, pp. 59-67, Apr 2017.

[35] Y. Li, Z. T. Xie, Y. Pang, D. Vigneron, and X. L. Zhang, "ICE decoupling technique for RF coil array designs," *Medical Physics,* vol. 38, no. 7, pp. 4086-4093, Jul 2011.

[36] N. I. Avdievich, J. W. Pan, and H. P. Hetherington, "Resonant inductive decoupling (RID) for transceiver arrays to compensate for both reactive and resistive components of the mutual impedance," *NMR in Biomedicine,* vol. 26, no. 11, pp. 1547-1554, Nov 2013.

[37] Z. Mahmood, B. Guérin, E. Adalsteinsson, L. L. Wald, and L. Daniel, "An Automated Framework to Decouple pTx Arrays with Many Channels," *In Proceedings of the 21st Annual Meeting of ISMRM, Utah, USA, Abstract 2722,* 2013.

[38] N. I. Avdievich, I. A. Giapitzakis, A. Pfrommer, G. Shajan, K. Scheffler, and A. Henning, "Decoupling of a double-row 16-element tight-fit transceiver phased array for human whole-brain imaging at 9.4 T," *NMR in Biomedicine,* vol. 31, no. 9, Sep 2018.

[39] M. Kozlov, E. Lucano, and L. M. Angelone, "Effects of Tuning Conditions on Near Field of MRI Transmit Birdcage Coil at 64 MHz," *2016 38th Annual International Conference of the IEEE Engineering in Medicine and Biology Society (EMBC),* pp. 6242-6245, 2016.

[40] M. Kozlov and R. Turner, "Engineering of 7T transmit multi-row arrays," *2012 Annual International Conference of the IEEE Engineering in Medicine and Biology Society (EMBC),* pp. 1089-1092, 2012.

[41] J. P. Reilly, "Neuroelectric mechanisms applied to low frequency electric and magnetic field exposure guidelines - Part I: Sinusoidal waveforms," *Health Physics,* vol. 83, no. 3, pp. 341-355, Sep 2002.

[42] M. D. Fox, R. L. Buckner, H. S. Liu, M. M. Chakravarty, A. M. Lozano, and A. Pascual-Leone, "Resting-state networks link invasive and noninvasive brain stimulation across diverse psychiatric and neurological diseases," *In Proceedings of the National Academy of Sciences of the United States of America,* vol. 111, no. 41, pp. E4367-E4375, Oct 14 2014.

[43] C. E. McElcheran, B. S. Yang, K. J. T. Anderson, L. Golenstani-Rad, and S. J. Graham, "Investigation of Parallel Radiofrequency Transmission for the Reduction of Heating in Long Conductive Leads in 3 Tesla Magnetic Resonance Imaging," *PLoS One,* vol. 10, no. 8, p. e0134379, 2015.

[44] C. E. McElcheran, B. S. Yang, K. J. Anderson, L. Golestanirad, and S. J. Graham, "Parallel radiofrequency transmission at 3 tesla to improve safety in bilateral implanted wires in a heterogeneous model," *Magnetic Resonance in Medicine,* vol. 78, no. 6, pp. 2406-2415, 2017.

[45] Y. Eryaman, B. Akin, and E. Atalar, "Reduction of Implant RF Heating Through Modification of Transmit Coil Electric Field," *Magnetic Resonance in Medicine,* vol. 65, no. 5, pp. 1305-1313, May 2011.

[46] L. Golestanirad *et al.*, "Construction and modeling of a reconfigurable MRI coil for lowering SAR in patients with deep brain stimulation implants," *Neuroimage,* vol. 147, pp. 577-588, Feb 15 2017.

[47] L. Golestanirad, B. Keil, L. M. Angelone, G. Bonmassar, A. Mareyam, and L. L. Wald, "Feasibility of using linearly polarized rotating birdcage transmitters and close-fitting receive arrays in MRI to reduce SAR in the vicinity of deep brain simulation implants," *Magnetic Resonance in Medicine,* vol. 77, no. 4, pp. 1701-1712, 2017.

[48] E. Kazemivalipour, A. Sadeghi-Tarakameh, U. Gundogdu, and E. Atalar, "Design of multi-row multi-channel degenerate birdcage array coil based on minimum total reflection for the single-channel and circularly polarized modes of excitation," *In Proceedings of the 27th Annual Meeting of ISMRM, Montreal, Canada, Abstract 1532,* 2019.

[49] E. Kazemivalipour, A. Sadeghi-Tarakameh, and E. Atalar, "Design of transmit array coils for MRI by minimizing the modal reflection coefficients," *In Proceedings of the 28th Virtual Annual Meeting of ISMRM, Abstract 0762,* 2020.

[50] E. Kazemivalipour, A. Sadeghi-Tarakameh, and E. Atalar, "Eigenmode analysis of the scattering matrix for the design of MRI transmit array coils," *Magnetic Resonance in Medicine,* 2020.

[51] I. R. O. Connell, K. M. Gilbert, M. A. Abou-Khousa, and R. S. Menon, "MRI RF Array Decoupling Method With Magnetic Wall Distributed Filters," *IEEE Transactions on Medical Imaging,* vol. 34, no. 4, pp. 825-835, Apr 2015.

[52] M. Kozlov and R. Turner, "Analysis of RF transmit performance for a 7T dual row multichannel MRI loop array," *2011 Annual International Conference of the IEEE Engineering in Medicine and Biology Society (EMBC),* pp. 547-553, 2011.

[53] B. Guerin, K. Setsompop, H. H. Ye, B. A. Poser, A. V. Stenger, and L. L. Wald, "Design of Parallel Transmission Pulses for Simultaneous Multislice with Explicit Control for Peak Power and Local Specific Absorption Rate," *Magnetic Resonance in Medicine,* vol. 73, no. 5, pp. 1946-1953, May 2015.

[54] B. Guerin, M. Gebhardt, S. Cauley, E. Adalsteinsson, and L. L. Wald, "Local Specific Absorption Rate (SAR), Global SAR, Transmitter Power, and Excitation Accuracy Trade-Offs in Low Flip-Angle Parallel Transmit Pulse Design," *Magnetic Resonance in Medicine,* vol. 71, no. 4, pp. 1446-1457, Apr 2014.

[55] D. O. Brunner and K. P. Pruessmann, "Optimal Design of Multiple-Channel RF Pulses Under Strict Power and SAR Constraints," *Magnetic Resonance in Medicine*, vol. 63, no. 5, pp. 1280-1291, May 2010.

[56] J. T. Vaughan *et al.*, "7T vs. 4T: RF power, homogeneity, and signal-to-noise comparison in head images," *Magnetic Resonance in Medicine*, vol. 46, no. 1, pp. 24-30, Jul 2001.

[57] B. van den Bergen, C. A. T. van den Berg, D. W. J. Klomp, and J. J. W. Lagendijk, "SAR and Power Implications of Different RF Shimming Strategies in the Pelvis for 7T MRI," *Journal of Magnetic Resonance Imaging*, vol. 30, no. 1, pp. 194-202, Jul 2009.

[58] M. Kozlov and R. Turner, "Effects of Tuning Condition, Head Size and Position on the SAR of a MRI Dual-row Transmit Array at 400 MHz," *In Proceedings PIERS, Taipei*, pp. 422-426, 2013.

[59] X. Q. Yan, J. O. Pedersen, L. Wei, X. L. Zhang, and R. Xue, "Multichannel Double-Row Transmission Line Array for Human MR Imaging at Ultrahigh Fields," *IEEE Transactions on Biomedical Engineering*, vol. 62, no. 6, pp. 1652-1659, Jun 2015.

[60] G. Shajan, M. Kozlov, J. Hoffmann, R. Turner, K. Scheffler, and R. Pohmann, "A 16-Channel Dual-Row Transmit Array in Combination with a 31-Element Receive Array for Human Brain Imaging at 9.4 T," *Magnetic Resonance in Medicine*, vol. 71, no. 2, pp. 870-879, Feb 2014.

[61] J. Hoffmann, G. Shajan, K. Scheffler, and R. Pohmann, "Numerical and experimental evaluation of RF shimming in the human brain at 9.4 T using a dual-row transmit array," *Magnetic Resonance Materials in Physics Biology and Medicine*, vol. 27, no. 5, pp. 373-386, Oct 2014.

[62] V. Alagappan *et al.*, "Degenerate mode band-pass birdcage coil for accelerated parallel excitation," *Magnetic Resonance in Medicine*, vol. 57, no. 6, pp. 1148-1158, Jun 2007.

[63] R. Stara *et al.*, "A Degenerate Birdcage with Integrated Tx/Rx Switches and Butler Matrix for the Human Limbs at 7 T," *Applied Magnetic Resonance,* vol. 48, no. 3, pp. 307-326, Mar 2017.

[64] D. M. Pozar, *Microwave engineering,* 4th ed. Hoboken, NJ: Wiley, 2012, pp. xvii, 732 pages.

[65] C. Volmer, J. Weber, R. Stephan, K. Blau, and M. A. Hein, "An eigen-analysis of compact antenna arrays and its application to port decoupling," *IEEE Transactions on Antennas and Propagation,* vol. 56, no. 2, pp. 360-370, Feb 2008.

[66] S. Irteza, E. Schafer, R. Stephan, A. Hornbostel, and M. A. Hein, "Compact antenna array receiver for robust satellite navigation systems," *International Journal of Microwave and Wireless Technologies,* vol. 7, no. 6, pp. 735-745, Dec 2015.

[67] R. A. Horn and C. R. Johnson, *Matrix analysis*. Cambridge Cambridgeshire ; New York: Cambridge University Press, 1985, pp. xiii, 561 p.

[68] D. C. Lay, S. R. Lay, and J. McDonald, *Linear algebra and its applications*, Sixth edition . ed. Boston: Pearson, 2020, p. pages cm.

[69] L. N. Trefethen and D. Bau, *Numerical linear algebra*. Philadelphia: Society for Industrial and Applied Mathematics, 1997, pp. xii, 361 p.

[70] M. Kozlov and R. Turner, "Comprehensive analysis of transmit performance for an 8-element loop MRI RF coil at 300 MHz," *40th European Microwave Conference,* pp. 328-331, 2010.

[71] E. Kazemivalipour, A. Sadeghi-Tarakameh, U. Yilmaz, V. Acikel, B. Sen, and E. Atalar, "A 12-Channel Degenerate Birdcage Body Transmit Array Coil for 1.5T MRI Scanners," *In Proceedings of the 26th Annual Meeting of ISMRM-ESMRMB, Paris, France, Abstract 1708,* 2018.

[72] J. Nistler, R. Kurth, M. Vester, and W. Renz, "B1 inhomogenisation using a multichannel transmit array," *In Proceedings of the 14th Annual Meeting of ISMRM, Seattle, USA, Abstract 2471,* 2006.

[73] A. Sadeghi-Tarakameh, E. Kazemivalipour, U. Gundogdu, S. Erdogan, and E. Atalar, "Accelerating the co-simulation method for the design of transmit array coils for MRI," *Magnetic Resonance Materials in Physics Biology and Medicine*, Jun 27 2020.

[74] E. Kazemivalipour, A. Sadeghi-Tarakameh, U. Yilmaz, and E. Atalar, "Design of an 8-channel transmit array coil using the equivalent circuit model of the manufactured structure," *In Proceedings of the 28th Virtual Annual Meeting of ISMRM, Abstract 0758*, 2020.

[75] C. A. Balanis, *Advanced engineering electromagnetics*, 2nd ed. Hoboken, N.J.: Wiley, 2012, pp. xx, 1018 p.

[76] M. Kozlov and R. Turner, "Fast MRI coil analysis based on 3-D electromagnetic and RF circuit co-simulation," *Journal of Magnetic Resonance*, vol. 200, no. 1, pp. 147-152, 2009.

[77] C. E. Hayes and M. G. Eash, "Shield for decoupling RF and gradient coils in an NMR apparatus," *US patent #4642569A*, 1987.

[78] N. Gurler and Y. Z. Ider, "Gradient-based electrical conductivity imaging using MR phase," *Magnetic Resonance in Medicine*, vol. 77, no. 1, pp. 137-150, Jan 2017.

[79] C. Gabriel, S. Gabriel, E. H. Grant, B. S. J. Halstead, and D. M. P. Mingos, "Dielectric parameters relevant to microwave dielectric heating," *Chemical Society Reviews*, vol. 27, no. 3, pp. 213-223, May 1998.

[80] S. A. Winkler and B. K. Rutt, "Practical Methods for Improving B-1(+) Homogeneity in 3 Tesla Breast Imaging," *Journal of Magnetic Resonance Imaging*, vol. 41, no. 4, pp. 992-999, Apr 2015.

[81] L. I. Sacolick, F. Wiesinger, I. Hancu, and M. W. Vogel, "B1 mapping by Bloch-Siegert shift," *Magnetic Resonance in Medicine*, vol. 63, no. 5, pp. 1315-22, May 2010.

[82] E. A. Turk, Y. Z. Ider, A. S. Ergun, and E. Atalar, "Approximate Fourier domain expression for Bloch-Siegert shift," *Magnetic Resonance in Medicine*, vol. 73, no. 1, pp. 117-25, Jan 2015.

[83] A. C. Ludwig, "Mutual Coupling, Gain and Directivity of an Array of 2 Identical Antennas," *IEEE Transactions on Antennas and Propagation*, vol. 24, no. 6, pp. 837-841, 1976.

[84] S. H. Chae, S. K. Oh, and S. O. Park, "Analysis of mutual coupling, correlations, and TARC in WiBro MIMO array antenna," *IEEE Antennas and Wireless Propagation Letters*, vol. 6, pp. 122-125, 2007.

[85] J. M. Hannula, T. Saarinen, J. Holopainen, and V. Viikari, "Frequency Reconfigurable Multiband Handset Antenna Based on a Multichannel Transceiver," *IEEE Transactions on Antennas and Propagation*, vol. 65, no. 9, pp. 4452-4460, Sep 2017.

[86] S. B. King, S. M. Varosi, and G. R. Duensing, "Eigenmode analysis for understanding phased array coils and their limits," *Concepts in Magnetic Resonance Part B-Magnetic Resonance Engineering*, vol. 29b, no. 1, pp. 42-49, Feb 2006.

[87] S. B. King, S. M. Varosi, and G. R. Duensing, "Optimum SNR Data Compression in Hardware Using an Eigencoil Array," *Magnetic Resonance in Medicine*, vol. 63, no. 5, pp. 1346-1356, May 2010.

[88] C. S. Wang, P. Qu, and G. X. Shen, "Potential advantage of higher-order modes of birdcage coil for parallel imaging," *Journal of Magnetic Resonance*, vol. 182, no. 1, pp. 160-167, Sep 2006.

[89] T. Santini *et al.*, "In-vivo and numerical analysis of the eigenmodes produced by a multi-level Tic-Tac-Toe head transmit array for 7 Tesla MRI," *PLoS One*, vol. 13, no. 11, Nov 27 2018.

[90] P. A. Bottomley, R. W. Redington, W. A. Edelstein, and J. F. Schenck, "Estimating Radiofrequency Power Deposition in Body Nmr Imaging," *Magnetic Resonance in Medicine*, vol. 2, no. 4, pp. 336-349, 1985.

[91] D. I. Hoult, C. N. Chen, and V. J. Sank, "The Field-Dependence of Nmr Imaging .2. Arguments Concerning an Optimal Field-Strength," *Magnetic Resonance in Medicine*, vol. 3, no. 5, pp. 730-746, Oct 1986.

[92] T. S. Ibrahim and L. Tang, "Insight into RF power requirements and B-1 field homogeneity for human MRI via rigorous FDTD approach," *Journal of Magnetic Resonance Imaging*, vol. 25, no. 6, pp. 1235-1247, Jun 2007.

[93] T. S. Ibrahim, "A numerical analysis of radio-frequency power requirements in magnetic resonance imaging experiment," *IEEE Transactions on Microwave Theory and Techniques*, vol. 52, no. 8, pp. 1999-2003, Aug 2004.

[94] J. F. Villena *et al.*, "Fast Electromagnetic Analysis of MRI Transmit RF Coils Based on Accelerated Integral Equation Methods," *IEEE Transactions on Biomedical Engineering*, vol. 63, no. 11, pp. 2250-2261, Nov 2016.

[95] J. Chen, Z. M. Feng, and J. M. Jin, "Numerical simulation of SAR and B-1-field inhomogeneity of shielded RF coils loaded with the human head," *IEEE Transactions on Biomedical Engineering*, vol. 45, no. 5, pp. 650-659, May 1998.

[96] B. Khalichi, O. Ergul, and V. B. Erturk, "Broadband Solutions of Potential Integral Equations With NSPWMLFMA," *IEEE Transactions on Antennas and Propagation*, vol. 67, no. 6, pp. 4307-4312, Jun 2019.

[97] B. Khalichi, O. Ergul, M. Takrimi, and V. B. Erturk, "Solution of Potential Integral Equations with NSPWMLFMA," *2018 IEEE Antennas and Propagation Society International Symposium on Antennas and Propagation & Usnc/Ursi National Radio Science Meeting*, pp. 2307-2308, 2018.

[98] B. Khalichi, V. B. Erturk, and O. Ergul, "Fast Solutions of Multiscale Electromagnetic Problems Using Potential Integral Equations," *2020 IEEE AP-S Symposium on Antennas and Propagation and USNC-URSI Radio Science Meeting*, July 2020 2020.

[99] B. Khalichi, O. Ergul, and V. B. Erturk, "Error Analysis of {QR}-Decomposition-Based Nondirective Stable Plane Wave MLFMA," *2018 IEEE*

AP-S Symposium on Antennas and Propagation and USNC-URSI Radio Science Meeting, June 2018 2018.

[100] A. Rogovich, A. Monorchio, P. Nepa, G. Manara, G. Giovannetti, and L. Landini, "Design of Magnetic Resonance Imaging (MRI) RF coils by using the method of moments," *IEEE Antennas and Propagation Society Symposium, Vols 1-4 2004, Digest*, pp. 950-953, 2004.

[101] W. Zhao *et al.*, "Nineteen-Channel Receive Array and Four-Channel Transmit Array Coil for Cervical Spinal Cord Imaging at 7T," *Magnetic Resonance in Medicine*, vol. 72, no. 1, pp. 291-300, Jul 2014.

[102] X. Q. Yan *et al.*, "Optimization of an 8-Channel Loop-Array Coil for a 7 T MRI System with the Guidance of a Co-Simulation Approach," *Applied Magnetic Resonance*, vol. 45, no. 5, pp. 437-449, May 2014.

[103] A. M. Maunder, M. Daneshmand, P. Mousavi, B. G. Fallone, and N. De Zanche, "Stray Capacitance Between Magnetic Resonance Imaging Coil Elements: Models and Application to Array Decoupling," *IEEE Transactions on Microwave Theory and Techniques*, vol. 61, no. 12, pp. 4667-4677, Dec 2013.

[104] E. Kazemivalipour, A. Sadeghi-Tarakameh, and E. Atalar, "Optimization of the degenerate birdcage transmit array coil for minimum coupling," *In Proceedings of the 27th Annual Meeting of ISMRM, Montreal, Canada, Abstract 1604*, 2019.

[105] N. I. Avdievich, I. A. Giapitzakis, A. Pfrommer, and A. Henning, "Decoupling of a tight-fit transceiver phased array for human brain imaging at 9.4T: Loop overlapping rediscovered," *Magnetic Resonance in Medicine*, vol. 79, no. 2, pp. 1200-1211, Feb 2018.

[106] "HFSS Online Help, Ansoft Corporation," 2019.

[107] D. A. Seeber, I. Jevtic, and A. Menon, "Floating shield current suppression trap," *Concepts in Magnetic Resonance Part B-Magnetic Resonance Engineering*, vol. 21b, no. 1, pp. 26-31, Apr 2004.

[108] D. M. Peterson, B. L. Beck, C. R. Duensing, and J. R. Fitzsimmons, "Common mode signal rejection methods for MRI: Reduction of cable shield currents for

high static magnetic field systems," *Concepts in Magnetic Resonance Part B-Magnetic Resonance Engineering,* vol. 19b, no. 1, pp. 1-8, Oct 2003.

[109] M. D. Harpen, "Equivalent-Circuit for Birdcage Resonators," *Magnetic Resonance in Medicine,* vol. 29, no. 2, pp. 263-268, Feb 1993.

[110] J. M. Jin, R. L. Magin, G. Shen, and T. Perkins, "A Simple Method to Incorporate the Effects of an Rf Shield into Rf Resonator Analysis for Mri Applications," *IEEE Transactions on Biomedical Engineering,* vol. 42, no. 8, pp. 840-843, Aug 1995.

[111] D. F. Lu and P. M. Joseph, "A technique of double-resonant operation of 19F and 1H quadrature birdcage coils," *Magnetic Resonance in Medicine,* vol. 19, no. 1, pp. 180-5, May 1991.

[112] C. E. Hayes, "The development of the birdcage resonator: a historical perspective," *NMR in Biomedicine,* vol. 22, no. 9, pp. 908-918, Nov 2009.

[113] D. I. Hoult, "Sensitivity and power deposition in a high-field imaging experiment," *Journal of Magnetic Resonance Imaging,* vol. 12, no. 1, pp. 46-67, Jul 2000.

[114] C. M. Collins, W. Z. Liu, W. Schreiber, Q. X. Yang, and M. B. Smith, "Central brightening due to constructive interference with, without, and despite dielectric resonance," *Journal of Magnetic Resonance Imaging,* vol. 21, no. 2, pp. 192-196, Feb 2005.

[115] K. M. Gilbert, A. T. Curtis, J. S. Gati, L. M. Klassen, and R. S. Menon, "A radiofrequency coil to facilitate B-1(+) shimming and parallel imaging acceleration in three dimensions at 7 T," *NMR in Biomedicine,* vol. 24, no. 7, pp. 815-823, Aug 2011.

[116] B. Wu, X. L. Zhang, P. Qu, and G. X. Shen, "Capacitively decoupled tunable loop microstrip (TLM) array at 7 T," *Magnetic Resonance Imaging,* vol. 25, no. 3, pp. 418-424, Apr 2007.

[117] R. F. Lee, C. R. Westgate, R. G. Weiss, D. C. Newman, and P. A. Bottomley, "Planar strip array (PSA) for MRI," *Magnetic Resonance in Medicine,* vol. 45, no. 4, pp. 673-683, Apr 2001.

[118] A. J. E. Raaijmakers *et al.*, "Design of a Radiative Surface Coil Array Element at 7 T: The Single-Side Adapted Dipole Antenna," *Magnetic Resonance in Medicine,* vol. 66, no. 5, pp. 1488-1497, Nov 2011.

[119] A. J. E. Raaijmakers *et al.*, "The fractionated dipole antenna: A new antenna for body imaging at 7 Tesla," *Magnetic Resonance in Medicine,* vol. 75, no. 3, pp. 1366-1374, Mar 2016.

[120] Y. Eryaman *et al.*, "SAR Reduction in 7T C-Spine Imaging Using a "Dark Modes" Transmit Array Strategy," *Magnetic Resonance in Medicine,* vol. 73, no. 4, pp. 1533-1539, Apr 2015.

[121] J. Gutierrez-Gutierrez, "Positive integer powers of complex symmetric circulant matrices," *Applied Mathematics and Computation,* vol. 202, no. 2, pp. 877-881, Aug 15 2008.

[122] F. W. Grover, *Inductance calculations : working formulas and tables* (Dover Books on Engineering). Mineola, N.Y: Dover Publications, 2009, pp. xiv, 286 : ill. ; 22 cm.

[123] E. Kazemivalipour, E. Atalar, A. Vali, B. Keil, J. Pilitsis, and L. Golestanirad, "Reconfigurable coil technology significantly reduces the SAR at the tips of bilateral deep brain simulation leads during MRI at 3T: A realistic case study of isolated leads and fully-implanted systems," *In Proceedings of the 27th Annual Meeting of ISMRM, Montreal, Canada, Abstract 0727,* 2019.

[124] E. D. Flora, C. L. Perera, A. L. Cameron, and G. J. Maddern, "Deep brain stimulation for essential tremor: a systematic review," *Movement Disorders,* vol. 25, no. 11, pp. 1550-1559, 2010.

[125] J. P. Hubble, K. L. Busenbark, S. Wilkinson, R. D. Penn, K. Lyons, and W. C. Koller, "Deep brain stimulation for essential tremor," *Neurology,* vol. 46, no. 4, pp. 1150-1153, 1996.

[126] P. Blomstedt, G.-M. Hariz, M. I. Hariz, and L.-O. Koskinen, "Thalamic deep brain stimulation in the treatment of essential tremor: a long-term follow-up," *British Journal of Neurosurgery,* vol. 21, no. 5, pp. 504-509, 2007.

[127] R. Kumar, A. Dagher, W. D. Hutchison, A. E. Lang, and A. M. Lozano, "Globus pallidus deep brain stimulation for generalized dystonia: clinical and PET investigation," *Neurology,* vol. 53, no. 4, pp. 871-874, 1999.

[128] J. L. Ostrem and P. A. Starr, "Treatment of dystonia with deep brain stimulation," *Neurotherapeutics,* vol. 5, no. 2, pp. 320-330, Apr 2008.

[129] S. Owen, A. Green, D. Nandi, R. Bittar, S. Wang, and T. Z. Aziz, "Deep brain stimulation for neuropathic pain," in *Operative Neuromodulation*: Springer, 2007, pp. 111-116.

[130] S. G. Boccard, E. A. Pereira, L. Moir, T. Z. Aziz, and A. L. Green, "Long-term outcomes of deep brain stimulation for neuropathic pain," *Neurosurgery,* vol. 72, no. 2, pp. 221-231, 2012.

[131] L. Gabriels, P. Cosyns, B. Nuttin, H. Demeulemeester, and J. Gybels, "Deep brain stimulation for treatment-refractory obsessive-compulsive disorder: psychopathological and neuropsychological outcome in three cases," *Acta Psychiatrica Scandinavica,* vol. 107, no. 4, pp. 275-282, 2003.

[132] B. D. Greenberg *et al.*, "Deep brain stimulation of the ventral internal capsule/ventral striatum for obsessive-compulsive disorder: worldwide experience," *Molecular Psychiatry,* vol. 15, no. 1, pp. 64-79, 2008.

[133] P. Boon *et al.*, "Deep brain stimulation in patients with refractory temporal lobe epilepsy," *Epilepsia,* vol. 48, no. 8, pp. 1551-1560, 2007.

[134] A. W. Laxton and A. M. Lozano, "Deep brain stimulation for the treatment of Alzheimer disease and dementias," *World Neurosurgery,* vol. 80, no. 3-4, pp. S28. e1-S28. e8, 2013.

[135] A. M. Lozano *et al.*, "Deep brain stimulation: current challenges and future directions," *Nature Reviews Neurology,* p. 1, 2019.

[136] N. R. Williams, J. J. Taylor, K. Lamb, C. A. Hanlon, E. B. Short, and M. S. George, "Role of functional imaging in the development and refinement of invasive neuromodulation for psychiatric disorders," *World Journal of Radiology*, vol. 6, no. 10, p. 756, 2014.

[137] Z. Cui and Z. Ling, "A paradigm shift toward MRI-guided and MRI-verified DBS surgery Response," *Journal of Neurosurgery*, vol. 124, no. 4, pp. 1137-1138, 2016.

[138] A. R. Rezai *et al.*, "Is magnetic resonance imaging safe for patients with neurostimulation systems used for deep brain stimulation?," *Neurosurgery*, vol. 57, no. 5, pp. 1056-1062, 2005.

[139] A. R. Rezai *et al.*, "Neurostimulation system used for deep brain stimulation (DBS): MR safety issues and implications of failing to follow safety recommendations," *Investigative Radiology*, vol. 39, no. 5, pp. 300-303, 2004.

[140] Medtronic, "MRI Guidelines for Medtronic Deep Brain Stimulation Systems (http://manuals.medtronic.com/wcm/groups/mdtcom_sg/@emanuals/@era/@neuro/documents/documents/contrib_228155.pdf)," 2015

[141] St. Jude Medical, "MRI procedure Information," *https://manuals.sjm.com*, 2018.

[142] D. A. Feinberg and K. Setsompop, "Ultra-fast MRI of the human brain with simultaneous multi-slice imaging," *Journal of Magnetic Resonance*, vol. 229, pp. 90-100, 2013.

[143] S. Ramani, R. Schulte, G. Mckinnon, J. Ashe, J. Pilitsis, and I. Hancu, "Accurate localization of individual DBS contacts by MRI using zero-TE phase images," *In Proceedings of the 26th Annual Meeting of ISMRM, Paris, France, Abstract 2687*, 2018.

[144] W. R. Nitz, A. Oppelt, W. Renz, C. Manke, M. Lenhart, and J. Link, "On the heating of linear conductive structures as guide wires and catheters in interventional MRI," *Journal of Magnetic Resonance Imaging*, vol. 13, no. 1, pp. 105-114, 2001.

[145] S. M. Park, R. Kamondetdacha, and J. A. Nyenhuis, "Calculation of MRI-induced heating of an implanted medical lead wire with an electric field transfer function," *Journal of Magnetic Resonance Imaging*, vol. 26, no. 5, pp. 1278-1285, 2007.

[146] C. J. Yeung, R. C. Susil, and E. Atalar, "RF heating due to conductive wires during MRI depends on the phase distribution of the transmit field," *Magnetic Resonance in Medicine*, vol. 48, no. 6, pp. 1096-1098, Dec 2002.

[147] R. Buchli, P. Boesiger, and D. Meier, "Heating effects of metallic implants by MRI examinations," *Magnetic Resonance in Medicine*, vol. 7, no. 3, pp. 255-261, 1988.

[148] C.-K. Chou, J. A. McDougall, and K. W. Chan, "RF heating of implanted spinal fusion stimulator during magnetic resonance imaging," *IEEE Transactions on Biomedical Engineering*, vol. 44, no. 5, pp. 367-373, 1997.

[149] L. Golestanirad *et al.*, "RF-induced heating in tissue near bilateral DBS implants during MRI at 1.5 T and 3T: The role of surgical lead management," *NeuroImage*, vol. 184, pp. 566-576, 2019.

[150] P. Wei, B. Yang, C. McElcheran, L. Golestanirad, and S. Graham, "Reducing Radiofrequency-induced Heating in Realistic Deep Brain Stimulation Lead Trajectories using Parallel Transmission," in *In Proceedings of the 26th Annual Meeting of ISMRM, Paris, France, Abstract 0638*, 2018.

[151] C. E. McElcheran, L. Golestanirad, and S. J. Graham, "Heating Reduction in Unilateral And Bilateral Implanted Leads At 3T Using Parallel Radiofrequency Transmission in a Heterogeneous Head Model," in *In Proceedings of the 24th Annual Meeting of ISMRM, Singapore, Abstract 3659*, 2016.

[152] C. E. McElcheran *et al.*, "Parallel Transmission for Heating Reduction in Realistic Deep Brain Stimulation Lead Trajectories," in *In Proceedings of the 25th Annual Meeting of ISMRM, Honolulu, USA, Abstract 2633*, 2017.

[153] L. Golestanirad *et al.*, "A Patient-adjustable MRI coil for implant-friendly imaging of deep brain stimulation: Design, construction, and patient-specific

numerical simulations," *In Proceedings of the 24th Annual Meeting of ISMRM, Singapore, Abstract 0354,* 2016.

[154] H. U. Kerl, L. Gerigk, I. Pechlivanis, M. Al-Zghloul, C. Groden, and I. Nölte, "The subthalamic nucleus at 3.0 Tesla: choice of optimal sequence and orientation for deep brain stimulation using a standard installation protocol," *Journal of Neurosurgery,* vol. 117, no. 6, pp. 1155-1165, 2012.

[155] C. E. McElcheran, L. Golestanirad, and S. J. Graham, "Reduced Heating of Implanted Electrical Conductors Using Parallel Radiofrequency Transmission," in *In Proceedings of the 22nd Annual Meeting of ISMRM-ESMRMB, Milan, Italy, Abstract 0174,* 2014.

[156] Y. Eryaman *et al.,* "A simple geometric analysis method for measuring and mitigating RF induced currents on Deep Brain Stimulation leads by multichannel transmission/reception," *NeuroImage,* vol. 184, pp. 658-668, 2019.

[157] W. Ondo, M. Almaguer, J. Jankovic, and R. K. Simpson, "Thalamic deep brain stimulation: comparison between unilateral and bilateral placement," *Archives of Neurology,* vol. 58, no. 2, pp. 218-222, 2001.

[158] H. A. Taba *et al.,* "A closer look at unilateral versus bilateral deep brain stimulation: results of the National Institutes of Health COMPARE cohort," *Journal of Neurosurgery,* vol. 113, no. 6, pp. 1224-1229, 2010.

[159] I. Hancu *et al.,* "On the (Non-)equivalency of monopolar and bipolar settings for deep brain stimulation fMRI studies of Parkinson's disease patients," *Journal of Magnetic Resonance Imaging,* pp. 1736-1749, 2019.

[160] E. Mattei *et al.,* "Complexity of MRI induced heating on metallic leads: experimental measurements of 374 configurations," *BioMedical Engineering OnLine,* vol. 7, no. 1, p. 11, 2008.

[161] P. Nordbeck *et al.,* "Measuring RF-induced currents inside implants: Impact of device configuration on MRI safety of cardiac pacemaker leads," *Magnetic Resonance in Medicine,* vol. 61, no. 3, pp. 570-578, 2009.

[162] K. B. Baker, J. Tkach, J. D. Hall, J. A. Nyenhuis, F. G. Shellock, and A. R. Rezai, "Reduction of magnetic resonance imaging-related heating in deep brain stimulation leads using a lead management device," *Neurosurgery,* vol. 57, no. 4, pp. 392-397, 2005.

[163] L. Golestanirad, L. M. Angelone, M. I. Iacono, H. Katnani, L. L. Wald, and G. Bonmassar, "Local SAR near deep brain stimulation (DBS) electrodes at 64 MHz and 127 MHz: A simulation study of the effect of extracranial loops " *Magnetic Resonance in Medicine* vol. 88, no. 4, pp. 1558-1565, 2016.

[164] L. Golestanirad *et al.*, "Changes in the specific absorption rate (SAR) of radiofrequency energy in patients with retained cardiac leads during MRI at 1.5 T and 3 T," *Magnetic Resonance in Medicine,* vol. 81, no. 1, pp. 653-669, 2019.

[165] *IEEE P1528.4™/D1.0,Recommended Practice for Determining the Peak Spatial Average Specific Absorption Rate (SAR) in the Human Body from Wireless Communications Devices, 30 MHz - 6 GHz: Requirements for Using the Finite-Element Method for SAR Calculations, specifically involving Vehicle Mounted Antennas and Personal Wireless Devices*, 2014.

[166] E. Mattei *et al.*, "Temperature and SAR measurement errors in the evaluation of metallic linear structures heating during MRI using fluoroptic® probes," *Physics in Medicine and Biology,* vol. 52, no. 6, p. 1633, 2007.

[167] Yeo DT, Wang Z, Loew W, Vogel MW, and H. I, "Local SAR in High Pass Birdcage and TEM Body Coils for Multiple Human Body Models in Clinical Landmark Positions at 3T," *Journal of Magnetic Resonance Imaging*, vol. 33(5), pp. 1209–1217, 2011.

[168] H. L. M. Cheng and D. B. Plewes, "Tissue thermal conductivity by magnetic resonance thermometry and focused ultrasound heating," *Journal of Magnetic Resonance Imaging*, vol. 16, no. 5, pp. 598-609, 2002.

[169] C. R. Butson and C. C. McIntyre, "Role of electrode design on the volume of tissue activated during deep brain stimulation," *Journal of Neural Engineering*, vol. 3, no. 1, pp. 1-8, 2006.

[170] A. Chaturvedi, C. R. Butson, S. F. Lempka, S. E. Cooper, and C. C. McIntyre, "Patient-specific models of deep brain stimulation: influence of field model complexity on neural activation predictions," *Brain Stimulation,* vol. 3, no. 2, pp. 65-77, 2010.

[171] W. Grill, "Extracellular excitation of central neurons: implications for the mechanisms of deep brain stimulation," *Thalamus & Related Systems,* vol. 1, no. 3, pp. 269-277, 2001.

[172] C. C. McIntyre, W. M. Grill, D. L. Sherman, and N. V. Thakor, "Cellular effects of deep brain stimulation: model-based analysis of activation and inhibition," *Journal of Neurophysiology,* vol. 91, no. 4, pp. 1457-69, 2004.

[173] C. C. McIntyre, S. Mori, D. L. Sherman, N. V. Thakor, and J. L. Vitek, "Electric field and stimulating influence generated by deep brain stimulation of the subthalamic nucleus," *Clinical Neurophysiology,* vol. 115, no. 3, pp. 589-95, 2004.

[174] S. Miocinovic *et al.*, "Computational analysis of subthalamic nucleus and lenticular fasciculus activation during therapeutic deep brain stimulation," *Journal of Neurophysiology,* vol. 96, no. 3, pp. 1569-80, 2006.

[175] L. Golestanirad, B. Elahi, A. Molina Arribere, J. R. Mosig, C. Pollo, and S. J. Graham, "Analysis of fractal electrodes for efficient neural stimulation," *Frontiers in neuroengineering,* vol. 6, p. 3, 2013.

[176] L. Golestanirad, A. P. Izquierdo, S. J. Graham, J. R. Mosig, and C. Pollo, "Effect of realistic modeling of deep brain stimulation on the prediction of volume of activated tissue," *Progress In Electromagnetics Research,* vol. 126, pp. 1-16, 2012.

[177] L. Golestanirad *et al.*, "Solenoidal micromagnetic stimulation enables activation of axons with specific orientation," *Frontiers in Physiology,* vol. 9, 2018.

[178] C. C. McIntyre and P. J. Hahn, "Network perspectives on the mechanisms of deep brain stimulation," *Neurobiology of Disease,* vol. 38, no. 3, pp. 329-337, 2010.

[179] J. Geday, K. Østergaard, E. Johnsen, and A. Gjedde, "STN-stimulation in Parkinson's disease restores striatal inhibition of thalamocortical projection," *Human Brain Mapping,* vol. 30, no. 1, pp. 112-121, 2009.

[180] R. Cilia *et al.*, "Clinical and cerebral activity changes induced by subthalamic nucleus stimulation in advanced Parkinson's disease: a prospective case-control study," *Clinical Neurology and Neurosurgery,* vol. 111, no. 2, pp. 140-146, 2009.

[181] D. Shrivastava *et al.*, "Effect of the extracranial deep brain stimulation lead on radiofrequency heating at 9.4 Tesla (400.2 MHz)," *Journal of Magnetic Resonance Imaging,* vol. 32, no. 3, pp. 600-607, 2010.

[182] L. Golestanirad *et al.*, "Reducing RF-Induced Heating Near Implanted Leads Through High-Dielectric Capacitive Bleeding of Current (CBLOC)," *IEEE Transactions on Microwave Theory and Techniques,* 2019.

[183] P. Serano, L. M. Angelone, H. Katnani, E. Eskandar, and G. Bonmassar, "A Novel Brain Stimulation Technology Provides Compatibility with MRI," *Scientific Reports,* vol. 5, 2015.

[184] D. Hingwala, S. Chatterjee, C. Kesavadas, B. Thomas, and T. R. Kapilamoorthy, "Applications of 3D CISS sequence for problem solving in neuroimaging," *Indian Journal of Radiology and Imaging,* vol. 21, no. 2, pp. 90-97, 2011.

[185] E. Kazemivalipour *et al.*, "RF heating of deep brain stimulation implants during MRI in 1.2 T vertical scanners versus 1.5 T horizontal systems: A simulation study with realistic lead configurations," *2020 42nd Annual International Conference of the IEEE Engineering in Medicine & Biology Society (EMBC), Montreal, QC, Canada,* pp. 6143-6146, 2020.

[186] L. Golestanirad *et al.*, "RF heating of deep brain stimulation implants in open-bore vertical MRI systems: A simulation study with realistic device configurations," *Magnetic Resonance in Medicine,* vol. 83, no. 6, pp. 2284-2292, Jun 2020.

[187] P. Limousin *et al.*, "Effect on Parkinsonian Signs and Symptoms of Bilateral Subthalamic Nucleus Stimulation," *Lancet*, vol. 345, no. 8942, pp. 91-95, Jan 14 1995.

[188] W. M. Grill, "Safety considerations for deep brain stimulation: review and analysis," *Expert Review of Medical Devices*, vol. 2, no. 4, pp. 409-420, Jul 2005.

[189] A. R. Rezai *et al.*, "Neurostimulation systems for deep brain stimulation: In vitro evaluation of magnetic resonance imaging-related heating at 1.5 tesla," *Journal of Magnetic Resonance Imaging*, vol. 15, no. 3, pp. 241-250, Mar 2002.

[190] J. M. Henderson, J. Tkach, M. Phillips, K. Baker, F. G. Shellock, and A. R. Rezai, "Permanent neurological deficit related to magnetic resonance imaging in a patient with implanted deep brain stimulation electrodes for Parkinson's disease: case report," *Neurosurgery*, vol. 57, no. 5, p. E1063; discussion E1063, Nov 2005.

[191] L. Golestanirad *et al.*, "RF-induced heating in tissue near bilateral DBS implants during MRI at 1.5T and 3T: The role of surgical lead management," *Neuroimage*, vol. 184, pp. 566-576, Jan 1 2019.

[192] L. Golestanirad *et al.*, "Variation of RF heating around deep brain stimulation leads during 3.0 T MRI in fourteen patient-derived realistic lead models: The role of extracranial lead management," *In Proceedings of the 25th Annual Meeting of ISMRM, Honolulu, USA, Abstract 0484*, 2017.

[193] H. Ochi, Y. Soutome, Y. Bito, S. Suzuki, T. Shmoda, and T. Taniguchi, "RF coil and magnetic resonance device employing it," (in Japanese), December 9, 2008 2008, Art. no. Pub. No.: WO/2008/108048.

[194] G. Calcagnini *et al.*, "In vitro investigation of pacemaker lead heating induced by magnetic resonance imaging: Role of implant geometry," *Journal of Magnetic Resonance Imaging*, vol. 28, no. 4, pp. 879-886, Oct 2008.

[195] E. Mattei *et al.*, "Complexity of MRI induced heating on metallic leads: Experimental measurements of 374 configurations," *Biomedical Engineering Online,* vol. 7, Mar 3 2008.

[196] P. Nordbeck *et al.*, "Spatial distribution of RF-induced E-fields and implant heating in MRI," *Magnetic Resonance in Medicine,* vol. 60, no. 2, pp. 312-319, Aug 2008.

[197] P. Nordbeck *et al.*, "Impact of Imaging Landmark on the Risk of MRI-Related Heating Near Implanted Medical Devices Like Cardiac Pacemaker Leads," *Magnetic Resonance in Medicine,* vol. 65, no. 1, pp. 44-50, Jan 2011.

[198] E. Lucano *et al.*, "A numerical investigation on the effect of RF coil feed variability on global and local electromagnetic field exposure in human body models at 64 MHz," *Magnetic Resonance in Medicine,* vol. 79, no. 2, pp. 1135-1144, Feb 2018.

[199] C. Thalhammer *et al.*, "Two-Dimensional Sixteen Channel Transmi eceive Coil Array for Cardiac MRI at 7.0 T: Design, Evaluation, d Application," *Journal of Magnetic Resonance Imaging,* vol. 36, no. 4, pp. 847-857, Oct 2012.

[200] S. McCabe and J. Scott, "A Novel Implant Electrode Design Safe in the RF Field of MRI Scanners," *IEEE Transactions on Microwave Theory and Techniques,* vol. 65, no. 9, pp. 3541-3547, Sep 2017.

[201] Y. Eryaman, E. A. Turk, C. Oto, O. Algin, and E. Atalar, "Reduction of the radiofrequency heating of metallic devices using a dual-drive birdcage coil," *Magnetic Resonance in Medicine,* vol. 69, no. 3, pp. 845-852, Mar 2013.